THERMO-POROELASTIC FRACTURE PROPAGATION MODELING WITH DISPLACEMENT DISCONTINUITY BOUNDARY ELEMENT METHOD

A Dissertation

by

KWANG HEE CHUN

Submitted to the Office of Graduate Studies of
Texas A&M University
in partial fulfillment of the requirements for the degree of

DOCTOR OF PHILOSOPHY

Chair of Committee,	Ahmad Ghassemi
Committee Members,	Jerome Schubert
	Eduardo Gildin
	Charles Aubeny
Head of Department,	A. Daniel Hill

August 2013

Major Subject: Petroleum Engineering

ABSTRACT

The effect of coupled thermo-poroelastic behavior on hydraulic fracture propagation is of much interest in geothermal- and petroleum-related geomechanics problems such as wellbore stability and hydraulic fracturing as pore pressure and temperature variations can significantly induce rock deformation, fracture initiation, and propagation. In this dissertation, a two-dimensional (2D) boundary element method (BEM) was developed to simulate the fully coupled thermo-poroelastic fracture propagation process. The influence of pore pressure and temperature changes on the fracture propagation length and path, as well as on stress and pore pressure distribution near wellbores and fractures, was considered in isotropic and homogeneous rock formations.

The BEM used in this work consists of the displacement discontinuity (DD) method and the fictitious stress (FS) method. Also, a combined FS-DD numerical model was implemented for the hydraulically or thermally-induced fractures in the vicinity of a wellbore.

The linear elastic fracture mechanics (LEFM) theory was adopted to numerically model within the framework of poroelasticity and thermo-poroelasticity theory. For high accuracy of crack tip modeling, a special displacement discontinuity tip element was developed and extended to capture the pore pressure and temperature influence at the tip.

For poroelastic fracture propagation, a steadily propagating crack driven by fluid pressure was modeled to find the effect of pore pressure on crack path under the two

limiting poroelastic conditions (undrained and drained). The results indicate that the pore pressure diffusion has no influence on the crack growth under the undrained condition because the crack propagation velocity is too fast for the diffusion effect to take place. On the other hand, its influence on the crack path under the drained condition with its low propagation velocity has significance because it induces a change in principal stress direction, resulting in an alteration of fracture orientation.

For the thermal fracturing, when the rock around a wellbore and a main fracture is cooled by injecting cold water in a hot reservoir, the rapid decrease in temperature gives rise to thermal stress, which causes a crack to initiate and propagate into the rock matrix. The single and multiple fracture propagation caused by transient cooling in both thermoelastic and poro-thermoelastic rock were numerically modeled. The results of this study indicate that the thermal stresses induced by cooling may exceed the in-situ stress in the reservoir, creating secondary fractures perpendicular to main fracture. Furthermore, the faster cooling rate produces longer crack extension of the secondary thermal fractures. This implies that the faster cooling induces a higher tensile stress zone around the fracture, which tends to produce larger driving forces to make the secondary fractures penetrate deeper into the geothermal reservoir.

DEDICATION

To my Family

ACKNOWLEDGEMENTS

I would like to sincerely express my appreciation to my committee chair, Dr. Ghassemi, for his guidance and support throughout the course of this research.

I express thanks to the committee members, Dr. Schubert, Dr. Gildin, and Dr. Aubeny, for their academic assistance and cooperation.

Thanks also go to my friends and colleagues and the Harold Vance department of Petroleum Engineering faculty and staff for making my time at Texas A&M University a great experience. I also want to extend my gratitude to the American Rock Mechanics Association, which provided me the opportunity to attend an annual conference.

Finally, thanks to my mother, father, and sister for their encouragement and to my future wife for her patience and love.

NOMENCLATURE

a	fracture half-length
a_0	major semi-axis of the elliptical cooled region
b_0	minor semi-axis of the elliptical cooled region
B	Skempton pore pressure coefficient
c_f	fluid diffusivity
c^T	thermal diffusivity
c_p	specific heat capacity
c_r	rock heat capacity
c_w	water heat capacity
d	average crack spacing
D	main fracture length
D_n	normal displacement discontinuity
D_s	shear displacement discontinuity
E	Young's modulus of the rock
f_{ij}	dimensionless function
G	shear modulus of the rock
h	time step index
h_s	initial length of secondary fracture

k	intrinsic permeability
K	bulk modulus of the rock
K_0	modified Bessel function of second kind of zero order
K_1	modified Bessel function of second kind of first order
K_f	fluid bulk modulus
K_{I}	mode I stress intensity factor
K_{Ic}	fracture toughness of the rock
K_{II}	mode II stress intensity factor
K_{III}	mode III stress intensity factor
K_s	solid bulk modulus
K_u	undrained bulk modulus
M	Biot modulus
p	pore pressure
P	applied stress
P_0	initial pore pressure
q	fluid flux
q^T	heat flux
r	radial distance from the crack tip
s	Laplace operator
t	time

T	temperature
T_0	initial reservoir temperature
T_w	injection water temperature
u	displacement
v	crack propagation velocity
α	Biot coefficient
β	angle with the direction of applied stress
β_f	volumetric thermal expansion coefficient of fluid
β_m	hydro-thermal expansion coefficient
β_s	volumetric thermal expansion coefficient of solid
δ_{ij}	Kronecker delta function
ΔT	temperature difference
ε_{ij}	total strain tensor
ε_{kk}	volumetric strain
ζ	variation of fluid content
η	poroelastic coefficient
θ	angle with respect to the plane of a crack
θ_c	crack growth angle
κ	permeability
κ^T	thermal conductivity

μ	dynamic fluid viscosity
ν	Poisson's ratio
ν_u	undrained Poisson's ratio
ρ_m	total mass density
ρ_r	rock density
ρ_w	water density
ϕ	porosity
σ_1	Maximum principal stress
σ_h	Minimum in-situ stress
σ_H	Maximum in-situ stress
σ_{ij}	total stress tensor
σ_{kk}	volumetric stress
σ_n	normal stress
σ_{rr}	radial stress in polar coordinate
$\sigma_{r\theta}$	shear stress in polar coordinate
σ_s	shear stress
σ_{th}	thermally induced stress
$\sigma_{\theta\theta}$	tangential stress in polar coordinate

TABLE OF CONTENTS

Page

Page

Page

Page

LIST OF FIGURES

Page

Page

Page

Page

Page

Page

LIST OF TABLES

Page

1. INTRODUCTION

The fracture propagation modeling in response to thermo-poroelastic stresses is of much interest in geothermal reservoir stimulation. Generally, this process involves coupled rock deformation, fluid diffusion, heat diffusion, and thermo-poroelastic effects in the fluid-saturated porous rock. As we know, the subsurface rocks are filled with cracks and pore spaces saturated with one or more fluids such as oil, water, and gas, which can influence the mechanical behavior of rock. For example, if a rock is under compression, it leads to an increase in pore fluid pressure, and this pore pressure also gives rise to the volumetric deformation of the rock. The mechanical deformation of a rock is therefore coupled to the pore pressure.

Nevertheless, most analyses of fracture propagation problems in the petroleum industry have ignored the fluid-solid coupling effect. Numerical models in hydraulic fracturing have been developed under the assumption that the rock mass is an elastic medium and the pore pressure effect is negligible. Although such assumption may be acceptable in certain circumstances, in general, the coupling between rock deformation and pore pressure must be accounted for (Boone and Ingraffea 1990; Boone et al. 1991; Detournay and Cheng 1988; Detournay et al. 1989), and this coupling effect cannot be ignored (Zimmerman 2000).

Rock deformation and pore pressure can be also influenced by thermal effects. In several aspects of petroleum-related rock mechanics, temperature effects play an

important role (Finnie et al. 1979; McTigue 1986; Perkins and Gonzalez 1985; Stephens and Voight 1982; Wang et al. 1996). For example, when the reservoir rock is under cooling, the temperature difference between injecting water and the reservoir leads to both the shrinkage of the rock and decrease in pore pressure. In conventional reservoir condition (i.e., the drilling mud is cooler than the formation temperature), this thermal effect would contribute not only to inducing additional tensile stresses but also to lowering formation pore pressure around the borehole and fracture.

Basically the thermoelasticity is mathematically analogous to the poroelasticity in that the temperature plays a role similar to that of the pore pressure (Norris 1992; Rice and Cleary 1976). One difference between the two theories is thermo-mechanical coupling is unidirectional, in the sense that the temperature field has an effect on the rock deformation, but the stresses and strains have little effect on the temperature (Jaeger et al. 2007). As a consequence, the temperature field is decoupled from pore pressure and the stress field; thus, the heat flux and temperature can be calculated independently. A schematic illustration of the relationship between thermoelasticity and poroelasticity is shown in Figure 1.1.

Thermal fracturing is normally observed during injection period when the temperature difference between the cold injecting water and the hot reservoir is large. As the rock is cooled by cold water injection in a hot reservoir, the rapid decrease in temperature induces thermal stress which causes cracks to initiate and propagate into the rock matrix. And these induced thermal stresses can exceed the in-situ stresses, resulting in the creation of secondary fractures perpendicular to the main fracture because the

orientation of the principal stresses is reversed. This process is generally referred to as thermal fracturing.

Finally, as combining the poroelastic and thermoelastic effect, the influence of pore pressure and temperature changes on the fracture propagation length and path, as well as on stress and pore pressure distribution near wellbores and fractures, is considered in isotropic and homogeneous rock formations within the framework of poroelasticity and thermo-poroelasticity theory.

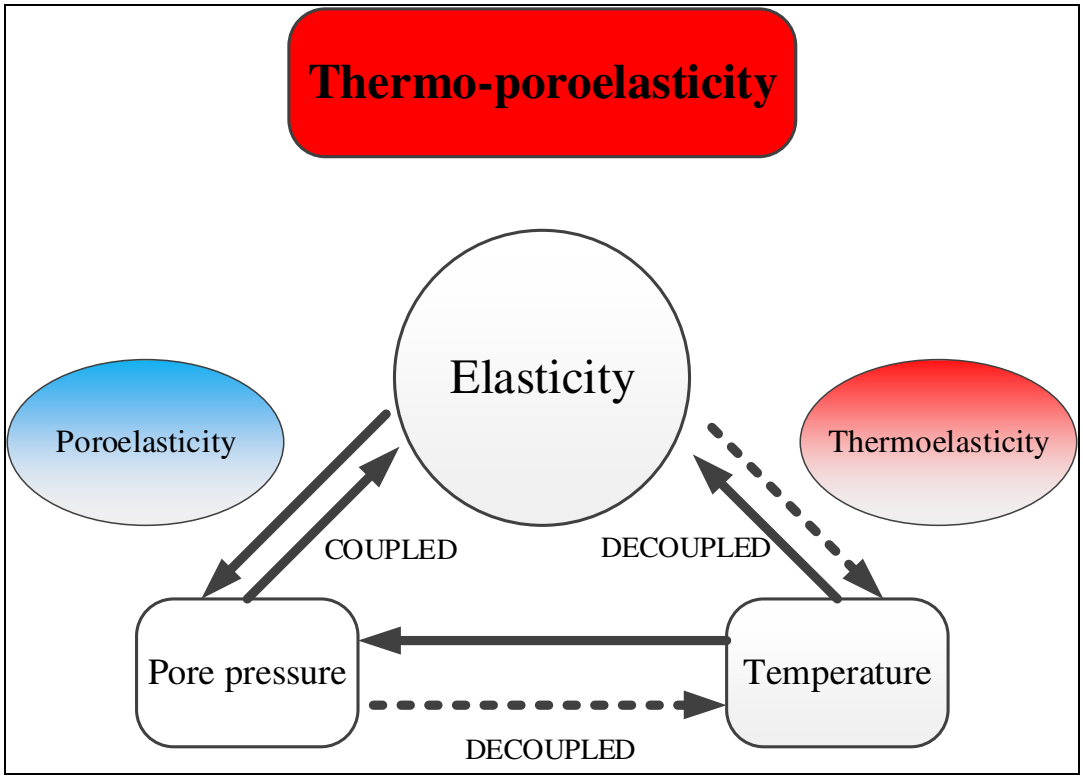

Figure 1.1 A schematic illustration of the relationship among elasticity, poroelasticity and thermoelasticity

1.1 Objectives

The objective in this work was to develop a two-dimensional (2D) boundary element method (BEM) to simulate fracture propagation stimulation under fully coupled thermo-poroelasticity theory. The displacement discontinuity method (DDM) and the fictitious stress method (FSM) were used to deal with fracture propagation modeling. The influence of pore pressure and temperature on the fracture propagation length and path as well as the stress and pore pressure distribution near hydraulically/thermally induced fractures in the vicinity of wellbore were considered in isotropic and homogeneous rock formations with a plane-strain assumption.

The specific objectives of the research were:

- To investigate a general poroelastic response of a crack in rock under Mode I (normal stress) and Mode II (pore pressure) loading
- To investigate a general thermo-poroelastic response of a crack in rock under Mode III (heat source) loading
- To observe transient poroelastic and thermo-poroelastic crack opening variations
- To observe transient poroelastic and thermo-poroelastic stress intensity factor (SIF) variations
- To investigate the fracture extension path under mixed-mode loading and analyze the influence of internal pressure and in-situ stress anisotropy in an elastic rock
- To simulate the coupled poroelastic fracture propagation model under two-limiting poroelastic behaviors (undrained and drained)
- To observe the thermal stress and temperature variation around a single fracture due

to transient cooling in hot reservoir

- To observe the orientation of the growing secondary fractures following cold water injection into a hot reservoir
- To observe the thermo-hydraulically induced fracture growth in the vicinity of a wellbore between the Westerly granite rock and the Haynesville shale formation

These goals have been achieved by working within the framework of the poroelasticity and thermo-poroelasticity theory.

1.2 Literature review

In recent years, the creation of hydraulically induced fractures in reservoir rock formation by injecting fluids has become a major procedure in the petroleum industry to boost the productivity of hydrocarbons from oil and gas wells that have low permeability. Generally, this hydraulic fracturing involves reversible coupled rock deformation and fluid diffusion effects in the fluid-saturated rock.

Poroelasticity theory accounts for deformation of a fluid-saturated porous rock. This theory, extended from the classical elasticity theory, takes into account the fluid phase, which indicates that two additional parameters are required to describe the isothermal state of the fluid (Guéguen and Boutéca 2004). They are pore pressure and fluid mass.

The coupled isothermal theory of poroelasticity was first presented by Biot (1941) and reformulated by several researchers (Geertsma 1966; Rice and Cleary 1976).

Limited work has investigated fractures in poroelastic material. Ruina (1978) has given an analytical solution for a semi-infinite crack propagating in poroelastic media, under various pore pressure boundary conditions on the crack faces, and his solution is practicable for a hydraulic fracture propagating at a constant rate with impermeable crack surfaces. Huang and Russell (1985) extended Ruina's results to steadily propagating cracks where the fracture walls are permeable.

According to Selvadurai and Mahyari (1998), in poroelastic material with the nature of dissipative phenomena, a steadily propagating crack can be modeled at limiting times when the fracture propagation has occurred over a long period of time. Also, to preserve the condition of a steadily propagating crack, the tractions along the boundary should be time invariant in a reference coordinate system moving with the crack tip in an infinite poroelastic medium. Atkinson and Craster (1991) examined pore pressure and stress distribution near the crack tip for a steadily propagating semi-infinite crack and investigated their relevance to the retardation of fracture.

Meanwhile, thermally induced stresses are developed when there are temperature differences between rock formation and injecting fluids. The constitutive equations for thermo-poroelasticity theory was first presented by Palciauskas and Domenico (1982). They extended the classic Biot (1941) theory by appropriately modifying for non-isothermal conditions with some representative parameters describing the thermal expansion of the fluid, solid, and pore volume. Carslaw and Jaeger (1959) showed an

analytical derivation of temperature and thermal stress field by heat conduction. McTigue (1986) showed several results of thermoelastic response of fluid-saturated porous rock. Perkins and Gonzalez (1985) showed that thermal stresses induced by cooling may exceed the in-situ stresses in the reservoir, resulting in the creation of secondary fractures perpendicular to main fracture. They showed that a thermally induced fracture can lead to an elliptical stress and temperature distribution around the cooled zone and proposed analytical expressions for the stress change in cooled regions as a function of dimension of the ellipticity.

The numerical approaches to the boundary element method in thermo-poroelastic geomechanical problems have been extended from the classical linear elastic theory. Numerical examples of pressurized cracks in elasticity have been applied successfully to many geological engineering problems with elastic DDM and FSM (Crouch and Starfield 1983). Direct and indirect boundary element methods, especially for poroelastic and thermo-poroelastic problems, have been discussed by many researchers (Ghassemi et al. 2001; Ghassemi et al. 2008; Ghassemi et al. 2007; Ghassemi and Zhang 2004, 2006; Ghassemi and Zhou 2011; Tao and Ghassemi 2007; Tao et al. 2011; Zhou and Ghassemi 2011). Boundary integral equations have also been considered. Especially for the fictitious stress and displacement discontinuity method, Carvalho (1990) developed poroelastic singular point source solutions in 2D and 3D problems. Zhang (2004) extended rock mechanics applications using a combined fictitious stress and displacement discontinuity method based on thermo-poroelasticity theory.

1.3 Summary of dissertation

This dissertation consists of eight sections. Section 1 describes the fracture propagation modeling in response to thermo-poroelastic effects. The pore pressure and temperature influence on the fracture propagation is reviewed with previous literature.

Section 2 explains the theory of poroelasticity and thermo-poroelasticity. Poroelastic and thermo-poroelastic constitutive equations are discussed, and related field equations are derived with the balance and transport laws.

Section 3 presents the general description of the boundary element method. The analytical and numerical methods based on the elastic DDM and FSM are described in detail, and they are extended to poroelastic and thermo-poroelastic problems. It also presents the numerical verifications and examples for the stationary crack to show the poroelastic and thermo-poroelastic response of the crack in rock.

Section 4 reviews essential key elements of the LEFM theory to model thermo-poroelastic fracture propagation. It introduces a stress intensity factor, fracture modes, and a crack-tip stress field in elastic rock. A numerical stress intensity factor is computed and verified with analytical solutions. In addition, numerical examples of fracture propagation in elastic rock are presented to illustrate the effect of the internal fluid pressure and in-situ stress anisotropy.

Section 5 illustrates fracture propagation in poroelastic rock and reviews Ruina's analytical approach. Fracture tip stress analysis is performed to investigate the stress and the pore pressure field near the crack tip between the undrained and drained conditions.

It also presents the numerical examples of fracture propagation under the two limiting regimes to show the influence of pore pressure on fracture extension path.

Section 6 demonstrates the impact of cooling on the fracture propagation and shows analytical solutions to the thermal stress and temperature variations due to cooling. The numerical examples of uniformly cooled cracks are simulated to capture the thermally induced stresses and temperature variations near the cooled crack. In addition, this section describes the secondary thermal fracture growth caused by temperature differences near the cooled crack.

Section 7 demonstrates the rock mechanics applications. The real-scale field examples are shown. The shale fracturing in the Haynesville formation is simulated and compared with the example in Westerly granite rock to observe the distinct aspect of the shale fracturing under thermo-poroelastic effects. The case of the secondary thermal fracture growth is also simulated and compared with the case in granite rock.

Last, Section 8 presents conclusions of this dissertation and recommendations for the future work.

2. THE LINEAR COUPLED DEFORMATION AND DIFFUSION PHENOMENA BASED ON THE THEORY OF THERMO-POROELASTICITY

2.1 Introduction

Most underground rocks in geological formations, by their nature, are filled with pore spaces where one or more fluids are saturated. The presence of this pore fluid in a porous rock can modify the rock's mechanical response. For example, an increase of pore pressure induces a volumetric deformation of a rock, or, conversely compression of a rock causes an increase of pore pressure. The mechanical deformation of a rock therefore is interrelated with the pore fluid, and this hydrological and mechanical behavior of porous rocks is fully coupled.

Meanwhile, the external loading applied on the rock can allow the induced pore pressure to diffuse through the pore network, so subsequent rock deformation progressively evolves. We can call it a coupled diffusion-deformation mechanism with time-dependent characteristics. When the loading is applied for very short time, the pore pressure in the rock's pore spaces increases because the pore fluid carries some part of the applied stress, and the rock behavior is stiffer under undrained conditions. However, when the loading is applied for a long period of time, increased pore pressure corresponding to compression of pore spaces has time to dissipate. Consequently, the rock behavior is the same as the elastic one.

The fundamental linear theory of poroelasticity was first suggested by Biot (1941). After that, this theory was reformulated by Biot himself (Biot 1955, 1956a,

1956b) and other researchers (Geertsma 1966; Rice and Cleary 1976). Rice and Cleary (1976) extended Biot's theory through different formulations of the coupled deformation-diffusion field equations. They also emphasized the two limiting behaviors, which are drained (no flow) and undrained (constant pore pressure) poroelastic behavior.

Meanwhile, a consideration of the heat transfer is also very important in many geomechanics fields, such as geothermal systems and unconventional resources, because it not only changes the total stress but also alters the pore fluid pressure, causing additional variations in the total and effective stress states. The constitutive equations for thermo-poroelasticity theory were first presented by Palciauskas and Domenico (1982). They extended the classic Biot's theory by appropriately modifying for non-isothermal conditions with some represented parameters describing the thermal expansion of the fluid, solid, and pore volume. McTigue (1986) considered particular solutions for coupled heat transfer, fluid pressure changes, and rock deformation in porothermoelastic media.

In this section, we briefly review the theory of poroelasticity and thermo-poroelasticity with the coupled diffusion-deformation phenomena.

2.2 Linear theory of poroelasticity

2.2.1 Poroelastic constitutive equations

The basic concept of Biot's poroelastic theory for a fluid-filled porous material is that the applied stress (σ_{ij}) and strain (ε_{ij}) field has linear constitutive relationships (Detournay and Cheng 1993; Wang 2000). This relation can be obtained by extending the generalized Hooke's law in elasticity theory.

The general form for poroelastic response in an isotropic material can be described as:

$$\varepsilon_{ij} = \frac{1}{2G}\left(\sigma_{ij} - \frac{\nu}{1+\nu}\sigma_{kk}\delta_{ij}\right) + \frac{\alpha}{3K}\delta_{ij}p \quad \text{..... (2.1)}$$

where ε_{ij} is solid strain tensor, σ_{ij} is total stress tensor, σ_{kk} is volumetric stress, and p is pore pressure. The constants G and K are shear and bulk modulus of elasticity, respectively, and the coefficient α is called the Biot coefficient.

The variation of fluid content (ζ) can be described as:

$$\zeta = \frac{\alpha}{K}\frac{\sigma_{kk}}{3} + \frac{\alpha}{BK}p \quad \text{..... (2.2)}$$

where B is the Skempton pore pressure coefficient, which is defined as the ratio of the induced pore pressure to the change of applied stress for the undrained condition; that is, no fluid is allowed to be transported in or out of the control volume:

$$B \equiv -\left.\frac{\delta p}{\delta \sigma}\right|_{\zeta=0} \quad \text{..... (2.3)}$$

Rearranging Eq. 2.1 in terms of σ_{ij} and Eq. 2.2 in terms of p ,

$$\sigma_{ij} = 2G(\varepsilon_{ij} + \frac{\nu}{1-2\nu}\varepsilon_{kk}\delta_{ij}) - \alpha\delta_{ij}p \quad \text{..... (2.4)}$$

$$p = M(\zeta - \alpha\varepsilon_{kk}) \quad \text{..... (2.5)}$$

where ε_{kk} is volumetric strain, δ_{ij} is the Kronecker delta function, and M is the Biot modulus defined by:

$$M = \frac{2G(\nu_u - \nu)}{\alpha^2(1-2\nu)(1-2\nu_u)} = \frac{BK_u}{\alpha} \quad \text{..... (2.6)}$$

where ν_u is the undrained Poisson's ratio and K_u is the undrained bulk modulus.

2.2.2 Field equations

The field equations consist of the balance laws for solids and fluids, and the transport laws for fluid. With these basic laws, we can also derive the Navier equation for the displacement u_i and diffusion equations for p and ζ.

The balance law for solid (force equilibrium equation) is:

$$\begin{aligned}
&\frac{\partial\sigma_{xx}}{\partial x} + \frac{\partial\sigma_{xy}}{\partial y} + \frac{\partial\sigma_{xz}}{\partial z} = 0 \\
&\frac{\partial\sigma_{yx}}{\partial x} + \frac{\partial\sigma_{yy}}{\partial y} + \frac{\partial\sigma_{yz}}{\partial z} = 0 \\
&\frac{\partial\sigma_{zx}}{\partial x} + \frac{\partial\sigma_{zy}}{\partial y} + \frac{\partial\sigma_{zz}}{\partial z} = 0
\end{aligned} \quad \text{..... (2.7)}$$

The balance law for fluid (continuity equation) is:

$$\frac{\partial\zeta}{\partial t} + \nabla\cdot q = 0 \quad \text{..... (2.8)}$$

The transport law for fluid (Darcy's law) is:

$$q_i = -\frac{k}{\mu} p_{,i} \quad \text{..... (2.9)}$$

where k is intrinsic permeability and μ is fluid viscosity.

The Navier equation for the displacement u_i:

$$G\nabla^2 u_i + \frac{G}{1-2\nu}\frac{\partial^2 u_k}{\partial x_i \partial x_k} = \alpha \frac{\partial p}{\partial x_i} \quad \text{.....(2.10)}$$

The diffusion equation for the pore pressure p is:

$$\frac{\partial p}{\partial t} - \frac{k}{\mu} M \nabla^2 p = -\alpha M \frac{\partial \varepsilon_{kk}}{\partial t} \quad \text{.....(2.11)}$$

The diffusion equation for the variation of fluid content ζ is:

$$\frac{\partial \zeta}{\partial t} - c_f \nabla^2 \zeta = 0 \quad \text{.....(2.12)}$$

where c_f is hydraulic diffusivity coefficient defined by:

$$c_f = \frac{2kG(1-\nu)(\nu_u - \nu)}{\alpha^2 \mu (1-2\nu)^2 (1-\nu_u)} \quad \text{.....(2.13)}$$

2.3 Linear theory of thermo-poroelasticity

2.3.1 Thermo-poroelastic constitutive equations

The constitutive equations for thermo-poroelasticity represent the effect of temperature change, which should be included in the constitutive equations for poroelasticity.

The general form for thermo-poroelastic response in isotropic material can be described as:

$$\sigma_{ij} = 2G(\varepsilon_{ij} + \frac{\nu}{1-2\nu}\varepsilon_{kk}\delta_{ij}) - \alpha\delta_{ij}p + K\beta_s\Delta T\delta_{ij} \quad \text{.....(2.14)}$$

$$\zeta = \frac{\alpha}{K}\frac{\sigma_{kk}}{3} + \frac{\alpha}{BK}p - \phi(\beta_f - \beta_s)\Delta T \quad \text{.....(2.15)}$$

where ϕ is porosity, β_f and β_s are the volumetric thermal expansion coefficients of fluid and solid respectively, and ΔT is temperature difference.

Eq. 2.15 can be rearranged in terms of pore pressure p :

$$p = M(\zeta - \alpha\varepsilon_{kk} + \beta_m\Delta T) \quad \text{.....(2.16)}$$

where β_m is the hydro-thermal expansion coefficient defined by:

$$\beta_m = \alpha\beta_s + \phi(\beta_f - \beta_s) \quad \text{.....(2.17)}$$

2.3.2 Field equations

The transport law for heat (Fourier's law) is:

$$q_i^T = -\kappa^T T_{,i} \quad \text{.....(2.18)}$$

where κ^T is thermal conductivity

The Navier equation for the displacement u_i is:

$$G\nabla^2 u_i + \frac{G+3K}{3}\frac{\partial \varepsilon}{\partial x_i} = \alpha \frac{\partial p}{\partial x_i} + K\beta_s \frac{\partial T}{\partial x_i} \quad \text{.....(2.19)}$$

The diffusion equation for the pore pressure p is:

$$\frac{\partial p}{\partial t} - \frac{k}{\mu} M \nabla^2 p = -\alpha M \frac{\partial \varepsilon_{kk}}{\partial t} + \beta_m M \frac{\partial T}{\partial t} \quad \text{.....(2.20)}$$

The diffusion equation for the temperature T is:

$$c^T \nabla^2 T = \frac{\partial T}{\partial t} \quad \text{.....(2.21)}$$

where c^T is the thermal diffusivity coefficient defined by:

$$c^T = \frac{\kappa^T}{\rho_m c_p} \quad \text{.....(2.22)}$$

where ρ_m is total mass density and c_p is specific heat capacity.

3. BOUNDARY ELEMENT METHOD

3.1 Introduction

The boundary element method (BEM) has become one of the useful numerical techniques to solve many types of differential equations and has been regarded as a strong alternative to finite element methods, particularly in cases where a high accuracy is required such as fracture mechanics problems in infinite extent (Brebbia and Dominquez 1992).

For example, in rock mechanics, a rock mass may be so large that we assume it is of infinite extent. In this case, the finite element method (FEM) is not a good way to solve the problem because a huge number of elements would have to be used to cover the response of the domain. However, the boundary elements only require the discretized surface of an excavation, which greatly reduces the amount of input data required to define the problem. The boundary element method also has been extensively used for coupled fluid-solid problems based on the poroelasticity and thermo-poroelasticity theory (Ghassemi et al. 2007; Ghassemi and Zhang 2004; Tao et al. 2011; Zhou and Ghassemi 2011). For this method to work, a fundamental solution (one that satisfies the differential equation in the problem) is required. Basically, this fundamental solution is a unit singular point solution of the differential equation distributed at specific density over the boundary of interest (Banerjee and Butterfield 1981). This point source would represent the point force, fluid source, heat source, or displacement discontinuity source in poro-thermo-mechanical problems. These solutions are usually called *singular*

solutions because they are well behaved everywhere in the region except at the point of source, where they exhibit a mathematical singularity (Crouch and Starfield 1983).

Figure 3.1 shows a number of discretized boundary elements on boundary Γ in the region Ω. Finite element analysis requires that the whole region Ω be divided into a network of elements; boundary element analysis requires only that the boundary Γ is divided into a finite number of elements. Once this boundary approximation is made, then the appropriate types of singular sources are distributed on these boundary elements along the boundary Γ, depending on the type of problems we are interested in. After that, the particular solution can be obtained by superposition of the all influences of the singular sources from each element in such a way that the prescribed boundary conditions are fully satisfied.

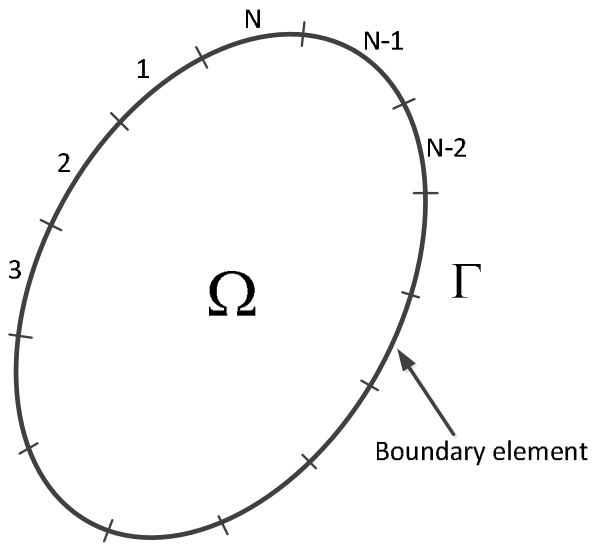

Figure 3.1 Boundary element idealization (Crouch and Starfield 1983)

Meanwhile, boundary elements can be divided naturally into two different but closely related categories (Banerjee and Butterfield 1981). These are the direct and indirect formulation of BEM. In the direct method, the unknown functions in the integral equations from Green's theorem are the actual physical variables, which can be derived from the boundary values by numerical integration.

In the indirect method, the integral equations are expressed entirely in terms of a unit singular solution of the original differential equations distributed at a specific density over the boundaries of interest. The density functions could be point force, fluid source, heat source, or displacement discontinuity source, and even though they have no physical importance, once they are obtained from the numerical solution, the value of the solution parameters (such as stress, displacements, pore pressure, temperature) anywhere within the body can be calculated from them by simple algebraic equations.

As a matter of fact, the indirect method has two sub-categories, namely the displacement discontinuity method (DDM) and the fictitious stress method (FSM). Each model is suited to solve different types of problems. For instance, the displacement discontinuity method is good for open-boundary problems such as fracture and joints, whereas the fictitious stress method performs well in closed-boundary value problems such as boreholes (Carvalho 1990).

In this section, we first present the basic description of the elastic DDM and FSM in detail. Then we extend this into the fully coupled poroelastic or thermo-poroelastic applications related to the problems in rock mechanics and geological engineering.

Finally, we demonstrate numerical examples to show how those applications are implemented and verified with analytical solutions.

3.2 Displacement discontinuity method

The displacement discontinuity method (DDM) is one of the indirect boundary element methods to solve solid mechanics problems containing discontinuities such as cracks and joints. Crouch and Starfield (1983) first introduced the DDM in elastic media to cope with rock mechanics and geological problems.

Basically, the DDM is based on an analytical solution of the problem of a constant discontinuity in displacement over a finite line segment in the x, y plane of an infinite elastic solid depicted as in Figure 3.2. The line segment is chosen to occupy a certain portion $|x| \le a$, $y = 0$. Consider this segment to be a line crack with two surfaces, which can be distinguished like this: one surface is on the positive side of y ($y = 0^+$), and the other is on the negative side of y ($y = 0^-$). In crossing from one side to the other, the displacement keeps constant, specified changes. We can define the displacement discontinuity D_i as the difference in displacement between the two sides of the segment as follows (Crouch and Starfield 1983):

$$\begin{aligned} D_s &= D_x = u_x(x,0^-) - u_x(x,0^+) \\ D_n &= D_y = u_y(x,0^-) - u_y(x,0^+) \end{aligned} \quad \text{..... (3.1)}$$

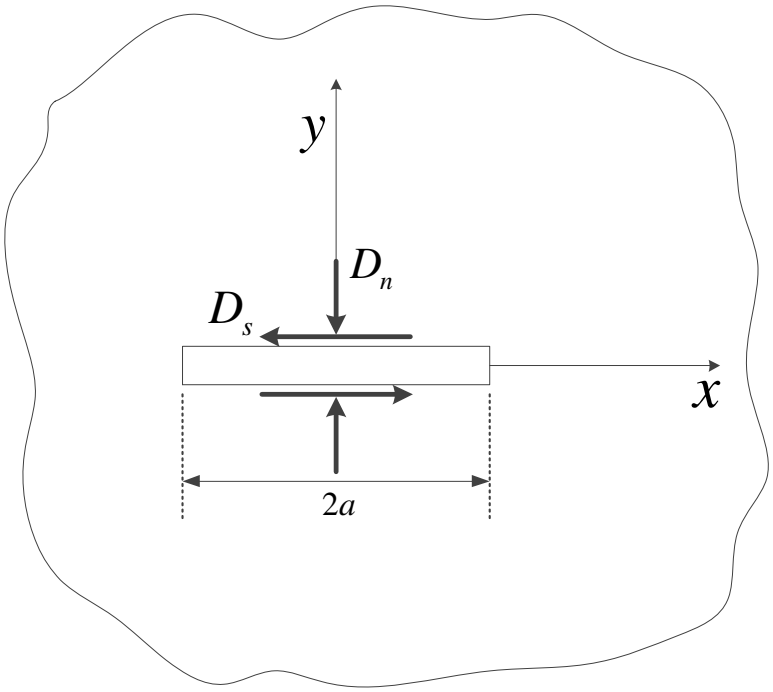

Figure 3.2 A thin line fracture in an infinite two-dimensional elastic medium with constant displacement discontinuity components D_n and D_s (Crouch and Starfield 1983)

Crouch (1976) also developed the fundamental stress solution at any arbitrary point (x, y) in an infinite elastic medium containing a thin-line fracture with constant discontinuity values.

The stresses can be written as

$$\sigma_{xx} = 2GD_s\left[2\frac{\partial^2 f}{\partial x\partial y} + y\frac{\partial^3 f}{\partial x\partial y^2}\right] + 2GD_n\left[\frac{\partial^2 f}{\partial y^2} + y\frac{\partial^3 f}{\partial y^3}\right]$$

$$\sigma_{yy} = 2GD_s\left[-y\frac{\partial^3 f}{\partial x\partial y^2}\right] + 2GD_n\left[\frac{\partial^2 f}{\partial y^2} - y\frac{\partial^3 f}{\partial y^3}\right] \quad \text{..... (3.2)}$$

$$\sigma_{xy} = 2GD_s\left[\frac{\partial^2 f}{\partial y^2} + y\frac{\partial^3 f}{\partial y^3}\right] + 2GD_n\left[-y\frac{\partial^3 f}{\partial x\partial y^2}\right]$$

where D_n is normal displacement discontinuity, D_s is shear displacement discontinuity, G is shear modulus and function $f(x, y)$ is defined as

$$f(x,y)=\frac{-1}{4\pi(1-\nu)}\left[\begin{array}{l} y\left(\arctan\frac{y}{x-a}-\arctan\frac{y}{x+a}\right)- \\ (x-a)\ln\sqrt{(x-a)^2+y^2}+(x+a)\ln\sqrt{(x+a)^2+y^2} \end{array}\right] \quad \text{..... (3.3)}$$

For the general numerical procedure for solving any crack problems, first we discretize the crack into N number of discrete displacement discontinuity elements under the assumption that the total number of elements should sufficiently represent numerical approximations to the real geometry of the crack.

Second, boundary influence coefficients at each discrete element are computed using Eq. 3.4. We will explain this in detail.

Figure 3.3 shows a discrete approximation of a curved crack with N segments arbitrarily inclined in the global (x, y) coordinate system. (Only 5 elements are shown for explanation). Each segment has normal and shear displacement discontinuity sources that can influence or can be influenced by each other in the local $(\bar{x}, \bar{y})$ coordinate system. For example, we have the influence of the normal ($\overset{j}{D}_n$) and shear ($\overset{j}{D}_s$) displacement discontinuity at the j th element that influences the normal and shear stresses at the i th influenced element. This influence can be determined with the appropriate coordinate transformation in terms of the normal and shear displacement discontinuities at the j th element shown in Eq. 3.4.

In here, the coefficient $\overset{ij}{A}$, for example, is the influence coefficient for normal stress due to constant normal displacement discontinuity over the j th element.

$$\left.\begin{aligned}\overset{i}{\sigma}_n &= \sum_{j=1}^{N} \overset{ij}{A}\,\overset{j}{D}_n + \sum_{j=1}^{N} \overset{ij}{B}\,\overset{j}{D}_s \\ \overset{i}{\sigma}_s &= \sum_{j=1}^{N} \overset{ij}{E}\,\overset{j}{D}_n + \sum_{j=1}^{N} \overset{ij}{F}\,\overset{j}{D}_s\end{aligned}\right\} i, j = 1,2,3...N \quad \text{..... (3.4)}$$

where $\overset{i}{\sigma}_n$, $\overset{i}{\sigma}_s$ are the normal and shear stresses at i th element due to influences from the j th element.

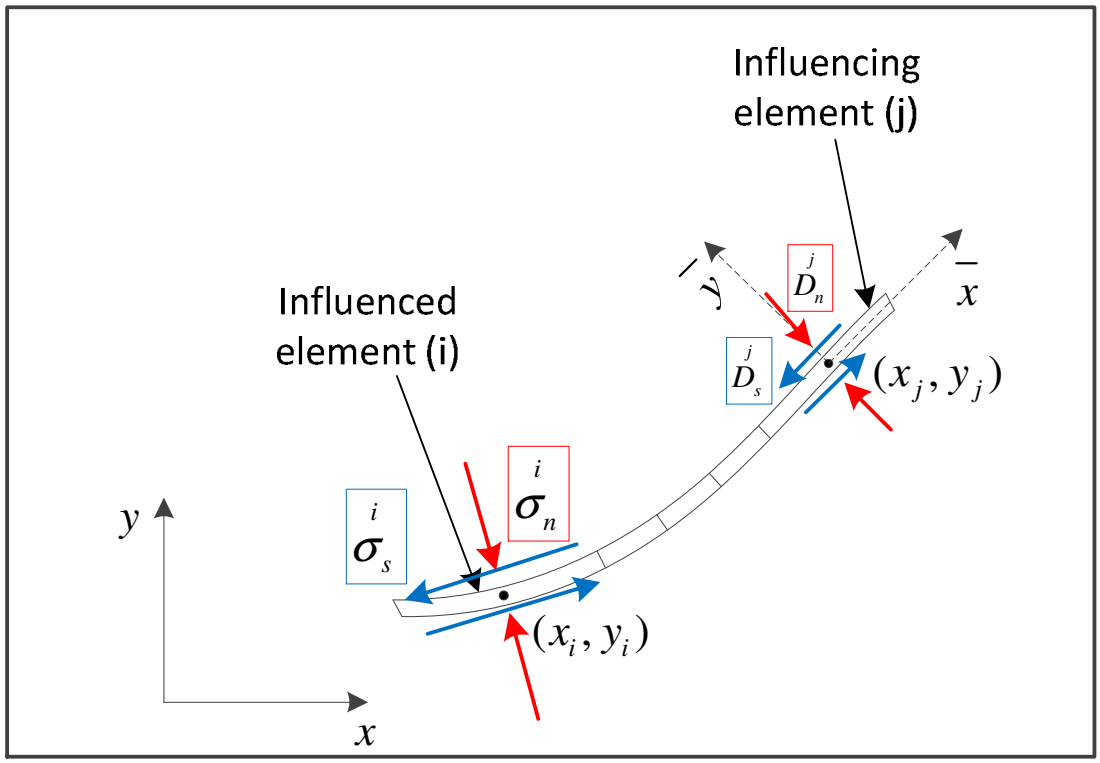

Figure 3.3 Influenced and influencing elements for the computation of influence coefficients

Third, when we specify boundary tractions such as $\overset{i}{\sigma}_n$ and $\overset{i}{\sigma}_s$ for each element of the crack, Eq. 3.4 is a system of $2N$ linear equations containing $2N$ unknowns. The matrix format for this case (with only 5 elements are shown for explanation) is shown in Eq. 3.5.

Finally, by solving these linear equations for $\overset{j}{D}_n$ and $\overset{j}{D}_s$, we can calculate stresses at random points in the body by using the principle of superposition.

$$\begin{pmatrix}
\overset{11}{A} & \overset{11}{B} & \overset{12}{A} & \overset{12}{B} & \overset{13}{A} & \overset{13}{B} & \overset{14}{A} & \overset{14}{B} & \overset{15}{A} & \overset{15}{B} \\
\overset{11}{E} & \overset{11}{F} & \overset{12}{E} & \overset{12}{F} & \overset{13}{E} & \overset{13}{F} & \overset{14}{E} & \overset{14}{F} & \overset{15}{E} & \overset{15}{F} \\
\overset{21}{A} & \overset{21}{B} & \overset{22}{A} & \overset{22}{B} & \overset{23}{A} & \overset{23}{B} & \overset{24}{A} & \overset{24}{B} & \overset{25}{A} & \overset{25}{B} \\
\overset{21}{E} & \overset{21}{F} & \overset{22}{E} & \overset{22}{F} & \overset{23}{E} & \overset{23}{F} & \overset{24}{E} & \overset{24}{F} & \overset{25}{E} & \overset{25}{F} \\
\overset{31}{A} & \overset{31}{B} & \overset{32}{A} & \overset{32}{B} & \overset{33}{A} & \overset{33}{B} & \overset{34}{A} & \overset{34}{B} & \overset{35}{A} & \overset{35}{B} \\
\overset{31}{E} & \overset{31}{F} & \overset{32}{E} & \overset{32}{F} & \overset{33}{E} & \overset{33}{F} & \overset{34}{E} & \overset{34}{F} & \overset{35}{E} & \overset{35}{F} \\
\overset{41}{A} & \overset{41}{B} & \overset{42}{A} & \overset{42}{B} & \overset{43}{A} & \overset{43}{B} & \overset{44}{A} & \overset{44}{B} & \overset{45}{A} & \overset{45}{B} \\
\overset{41}{E} & \overset{41}{F} & \overset{42}{E} & \overset{42}{F} & \overset{43}{E} & \overset{43}{F} & \overset{44}{E} & \overset{44}{F} & \overset{45}{E} & \overset{45}{F} \\
\overset{51}{A} & \overset{51}{B} & \overset{52}{A} & \overset{52}{B} & \overset{53}{A} & \overset{53}{B} & \overset{54}{A} & \overset{54}{B} & \overset{55}{A} & \overset{55}{B} \\
\overset{51}{E} & \overset{51}{F} & \overset{52}{E} & \overset{52}{F} & \overset{53}{E} & \overset{53}{F} & \overset{54}{E} & \overset{54}{F} & \overset{55}{E} & \overset{55}{F}
\end{pmatrix}
\begin{pmatrix}
\overset{1}{D}_n \\ \overset{1}{D}_s \\ \overset{2}{D}_n \\ \overset{2}{D}_s \\ \overset{3}{D}_n \\ \overset{3}{D}_s \\ \overset{4}{D}_n \\ \overset{4}{D}_s \\ \overset{5}{D}_n \\ \overset{5}{D}_s
\end{pmatrix} =
\begin{pmatrix}
\overset{1}{\sigma}_n \\ \overset{1}{\sigma}_s \\ \overset{2}{\sigma}_n \\ \overset{2}{\sigma}_s \\ \overset{3}{\sigma}_n \\ \overset{3}{\sigma}_s \\ \overset{4}{\sigma}_n \\ \overset{4}{\sigma}_s \\ \overset{5}{\sigma}_n \\ \overset{5}{\sigma}_s
\end{pmatrix} \quad \text{..... (3.5)}$$

The fundamental solutions of the fully coupled poroelastic displacement discontinuity method (DDM) for fluid-saturated porous media account for rock deformation, stresses, and pore pressure changes by constant fluid and displacement discontinuity source intensities on fracture segments. Carvalho (1990) provided the

fundamental solutions for the induced stress and pore pressure changes at any arbitrary point (x, y) in an infinite poroelastic medium containing a thin line fracture with constant fluid flux and displacement discontinuities on the fracture segments.

The induced pore pressure can be written as

$$p(x,y,t) = p^{dn}(x,y,t)D_n + p^{ds}(x,y,t)D_s + p^{q}(x,y,t)q_f \quad \text{..... (3.6)}$$

where D_n is normal displacement discontinuity, D_s is shear displacement discontinuity, and q_f is fluid flux. The coefficients p^{dn} and p^{ds} are the pore pressures of the influenced elements induced by the normal and shear displacement discontinuities of the influencing elements, respectively. The coefficient p^{q} is the pore pressure of the influenced elements induced by the fluid flux of the influencing elements.

The induced stress components can be written as

$$\begin{aligned}
\sigma_{xx}(x,y,t) &= \sigma_{xx}^{dn}(x,y,t)D_n + \sigma_{xx}^{ds}(x,y,t)D_s + \sigma_{xx}^{q}(x,y,t)q_f \\
\sigma_{yy}(x,y,t) &= \sigma_{yy}^{dn}(x,y,t)D_n + \sigma_{yy}^{ds}(x,y,t)D_s + \sigma_{yy}^{q}(x,y,t)q_f \quad \text{..... (3.7)} \\
\sigma_{xy}(x,y,t) &= \sigma_{xy}^{dn}(x,y,t)D_n + \sigma_{xy}^{ds}(x,y,t)D_s + \sigma_{xy}^{q}(x,y,t)q_f
\end{aligned}$$

where the coefficients σ_{xx}^{dn}, σ_{xx}^{ds} are the stress components of the influenced elements along the x direction induced by the normal and shear displacement discontinuities of the influencing elements, respectively. The coefficient σ_{xx}^{q} is the stress component of the

influenced elements along the x direction induced by the fluid flux of the influencing elements. Other stress components can be also defined with same terminologies as these. The boundary integral equations to calculate these poroelastic influence coefficients are explicitly presented by Tao (2010).

Let us assume a normal ($\overset{j}{D}_n$), shear ($\overset{j}{D}_s$) displacement discontinuity with a fluid flux ($\overset{j}{q}_f$) at the j th element that influences the normal, shear stresses, and the pore pressure at the i th influenced element. Similar to the approach in the elastic DDM, these influences in the poroelastic DDM can be determined with appropriate coordinate transformation in terms of the fluid flux and the constant normal and shear displacement discontinuities at the j th element shown in Eq. 3.8.

$$\left.\begin{aligned}
\overset{i}{\sigma}_n &= \sum_{j=1}^{N} \overset{ij}{A}\,\overset{j}{D}_n + \sum_{j=1}^{N} \overset{ij}{B}\,\overset{j}{D}_s + \sum_{j=1}^{N} \overset{ij}{C}\,\overset{j}{q}_f \\
\overset{i}{\sigma}_s &= \sum_{j=1}^{N} \overset{ij}{E}\,\overset{j}{D}_n + \sum_{j=1}^{N} \overset{ij}{F}\,\overset{j}{D}_s + \sum_{j=1}^{N} \overset{ij}{G}\,\overset{j}{q}_f \\
\overset{i}{p} &= \sum_{j=1}^{N} \overset{ij}{K}\,\overset{j}{D}_n + \sum_{j=1}^{N} \overset{ij}{L}\,\overset{j}{D}_s + \sum_{j=1}^{N} \overset{ij}{M}\,\overset{j}{q}_f
\end{aligned}\right\} i, j = 1, 2, 3 \ldots N \quad \text{..... (3.8)}$$

where $\overset{i}{\sigma}_n$, $\overset{i}{\sigma}_s$, $\overset{i}{p}$ are the normal and shear stresses and pore pressure, respectively at the i th element due to influences from the j th element.

3.3 Fictitious stress method

As noted, the fictitious stress method (FSM) has the same formulation and approach as the displacement discontinuity method except for the singular source type. Therefore, we describe it briefly in this section.

The elastic fictitious stress method is based on the analytical solution regarding the problem of a point force at a point in an infinite elastic solid, denoted as Kelvin's problem (Crouch and Starfield 1983). Kelvin's problem for plane strain conditions is illustrated in Figure 3.4.

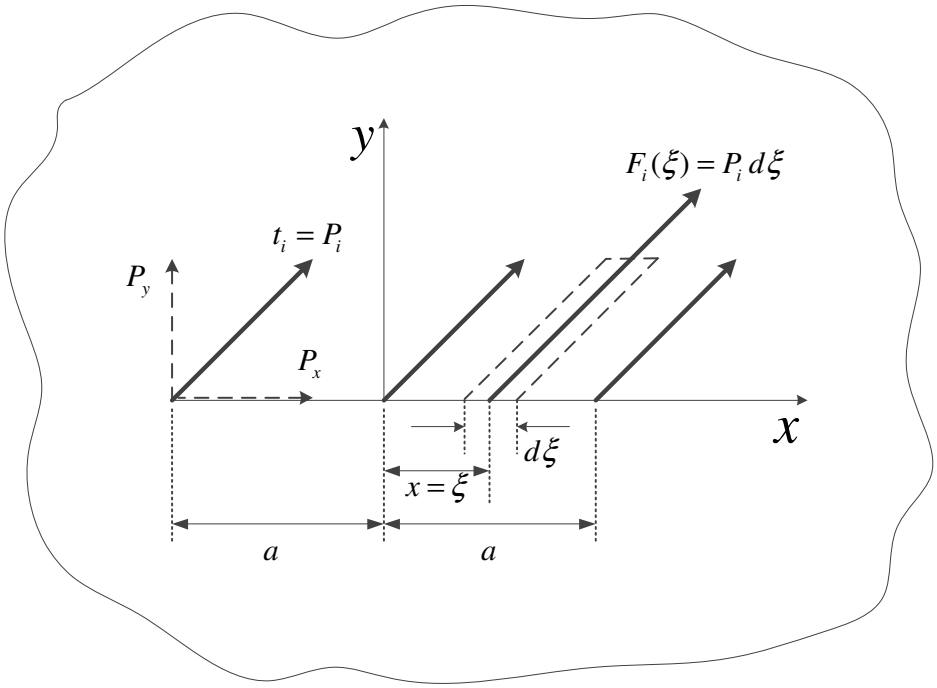

Figure 3.4 Point force distribution on the line segment in Kelvin's problem (Crouch and Starfield 1983)

Let's assume constant tractions $P_i = (P_x, P_y)$ are acting on the line segment, $|x| \le a$, $y = 0$. The solution for this problem can be obtained by integrating the Kelvin's point force solution with respect to ξ between the limits $-a$ and $+a$. The results can be expressed in terms of a function $f(x, y)$, which is defined as

$$f(x,y) = \int_{-a}^{a} g(x-\xi, y)\, d\xi \quad \text{..... (3.9)}$$

where $g(x, y)$ is defined by:

$$g(x,y) = -\frac{1}{4\pi(1-\nu)} \ln(x^2 + y^2)^{0.5} \quad \text{.....(3.10)}$$

Crouch (1976) developed the fundamental stress solution at any arbitrary point (x, y) in an infinite elastic medium with this line segment.

The stresses can be written as

$$\begin{aligned}
\sigma_{xx} &= P_x\left[(3-2\nu)\frac{\partial f}{\partial x} + y\frac{\partial^2 f}{\partial x \partial y}\right] + P_y\left[2\nu\frac{\partial f}{\partial y} + y\frac{\partial^2 f}{\partial y^2}\right] \\
\sigma_{yy} &= P_x\left[-(1-2\nu)\frac{\partial f}{\partial x} - y\frac{\partial^2 f}{\partial x \partial y}\right] + P_y\left[2(1-\nu)\frac{\partial f}{\partial y} - y\frac{\partial^2 f}{\partial y^2}\right] \quad \text{.....(3.11)} \\
\sigma_{xy} &= P_x\left[2(1-\nu)\frac{\partial f}{\partial y} + y\frac{\partial^2 f}{\partial y^2}\right] + P_y\left[(1-2\nu)\frac{\partial f}{\partial x} - y\frac{\partial^2 f}{\partial x \partial y}\right]
\end{aligned}$$

where $f(x, y)$ is defined as

$$f(x,y) = \frac{-1}{4\pi(1-\nu)}\left[\begin{array}{l} y\left(\arctan\dfrac{y}{x-a} - \arctan\dfrac{y}{x+a}\right) - \\ (x-a)\ln\sqrt{(x-a)^2+y^2} + (x+a)\ln\sqrt{(x+a)^2+y^2} \end{array}\right] \quad \text{.....(3.12)}$$

3.4 Discretization in time

Many important engineering problems do involve transient phenomena, which are governed by the linear diffusion equation (Banerjee and Butterfield 1981). Because the hydraulic and heat diffusion phenomena in thermo-poroelasticity induce the stress, pore pressure, and temperature changes as a function of time, it is necessary to keep track of the variation of those poroelastic or thermo-poroelastic variables in time. For the extensive numerical temporal solution, a "time-marching" process has been commonly used in numerical analysis with boundary elements because it can preserve the influence of all previous incremental singular sources (Banerjee and Butterfield 1981).

In a time-marching process, the solution is evaluated at successive time intervals following initially specified conditions. The basis of such processes is to march from $t = 0$, step by step using fixed time increments $\Delta\tau$ to any specified time $\tau_\xi = \xi\Delta\tau$ in ξ time steps. A basic illustration of incremental applications of the time sequence of displacement discontinuity is shown in Figure 3.5.

The basic procedure for the time discretization is explained in great detail. First, we choose the magnitude of fixed time increments $\Delta\tau$ from the point of view of our problem type and computational efficiency. Second, the singular sources are distributed at each element in space and time such that the sum of their influences satisfies the prescribed boundary conditions. In this work, we assumed that the discretized boundary elements were straight line segments with collocation points located at the center of each element. Also the distributed singular sources were located at collocation points and the intensity of those variables was constant over each element.

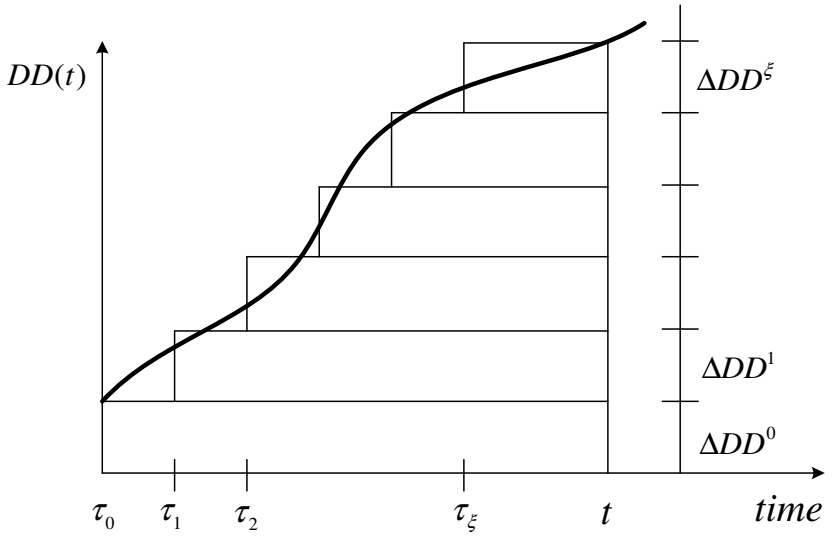

Figure 3.5 Time marching scheme for a continuous displacement discontinuity source increment applications

Finally, a time shift method can be applied to the fundamental solutions and the influence coefficients to compute the incremental normal ($\Delta \overset{\xi}{D}_n$) and shear ($\Delta \overset{\xi}{D}_s$) displacement discontinuities, fluid flux ($\Delta \overset{\xi}{q}_f$) or heat flux ($\Delta \overset{\xi}{h}_f$) over each element at time τ_ξ if the singular sources do not take place from $t = 0$ sec. For example, the stress tensor (σ_{ij}) at arbitrary points x at time t because the displacement discontinuity source took place at point X from time τ_ξ is equivalent to the stress at point x at time $t - \tau_\xi$ because the displacement discontinuity source exists at point X from time $t = 0$. This explanation can be expressed in terms of mathematical operators as follows.

$$\sigma_{ij}(x,t;\mathrm{X},\tau_\xi) = \sigma_{ij}(x,t-\tau_\xi;\mathrm{X},\tau_0) \quad \text{.....(3.13)}$$

Using this time shift method under the time-marching process, we can calculate transient solution parameters (such as stress, displacements, pore pressure, temperature) anywhere within the body without modifying the fundamental solutions.

We will describe the time-marching scheme used for thermo-poroelastic problems for the stationary crack in detail in section 3.4.1. For the non-stationary crack (i.e., fracture propagation), a detailed description of the time-marching scheme is shown in Appendix C.

3.4.1 Time marching scheme used for thermo-poroelastic fundamental solution for stationary crack (no propagation)

Suppose constant displacement discontinuities and fluid and heat sources exist on the N number of elements used to discretize our interest boundary. Given that i is the influenced element and j is influencing element, the total stress, pore pressure, and temperature induced on the i element at time t by a constant displacement discontinuity, fluid, and heat source that existed on the j element at time τ_ξ is given by:

$$
\begin{aligned}
\overset{i}{\sigma}_n &= \sum_{j=1}^{N} \overset{ij}{A}(t-\tau_\xi)\Delta \overset{j\xi}{D}_n + \sum_{j=1}^{N} \overset{ij}{B}(t-\tau_\xi)\Delta \overset{j\xi}{D}_s + \sum_{j=1}^{N} \overset{ij}{C}(t-\tau_\xi)\Delta \overset{j\xi}{q}_f + \sum_{j=1}^{N} \overset{ij}{T}(t-\tau_\xi)\Delta \overset{j\xi}{h}_f \\
\overset{i}{\sigma}_s &= \sum_{j=1}^{N} \overset{ij}{E}(t-\tau_\xi)\Delta \overset{j\xi}{D}_n + \sum_{j=1}^{N} \overset{ij}{F}(t-\tau_\xi)\Delta \overset{j\xi}{D}_s + \sum_{j=1}^{N} \overset{ij}{G}(t-\tau_\xi)\Delta \overset{j\xi}{q}_f + \sum_{j=1}^{N} \overset{ij}{T}(t-\tau_\xi)\Delta \overset{j\xi}{h}_f \\
\overset{i}{p} &= \sum_{j=1}^{N} \overset{ij}{K}(t-\tau_\xi)\Delta \overset{j\xi}{D}_n + \sum_{j=1}^{N} \overset{ij}{L}(t-\tau_\xi)\Delta \overset{j\xi}{D}_s + \sum_{j=1}^{N} \overset{ij}{M}(t-\tau_\xi)\Delta \overset{j\xi}{q}_f + \sum_{j=1}^{N} \overset{ij}{T}(t-\tau_\xi)\Delta \overset{j\xi}{h}_f \\
\overset{i}{T} &= \sum_{j=1}^{N} \overset{ij}{T}(t-\tau_\xi)\Delta \overset{j\xi}{h}_f
\end{aligned}
\qquad \text{.....(3.14)}
$$

where $\Delta \overset{j\xi}{D}_n$, $\Delta \overset{j\xi}{D}_s$, $\Delta \overset{j\xi}{q}_f$, and $\Delta \overset{j\xi}{h}_f$ denote the increment of normal displacement discontinuity, shear displacement discontinuity, fluid flux, and heat flux of the j th fracture segment at time τ_ξ . $\overset{ij}{A}(t-\tau_\xi)$, $\overset{ij}{B}(t-\tau_\xi)$, $\overset{ij}{C}(t-\tau_\xi)$, $\overset{ij}{E}(t-\tau_\xi)$, $\overset{ij}{F}(t-\tau_\xi)$, $\overset{ij}{G}(t-\tau_\xi)$, $\overset{ij}{K}(t-\tau_\xi)$, $\overset{ij}{L}(t-\tau_\xi)$, $\overset{ij}{M}(t-\tau_\xi)$ and $\overset{ij}{T}(t-\tau_\xi)$ are the influence coefficients of j th fracture segment on the i th fracture element at time step ξ.

Then the total induced stress, pore pressure, and temperature on the i th fracture segment at time t can be obtained by summing the influences from all the previous time steps.

$$
\begin{aligned}
\overset{i}{\sigma}_n(t) &= \sum_{h=0}^{\xi}\sum_{j=1}^{N} \overset{ij}{A}(t-\tau_h)\Delta \overset{jh}{D}_n + \sum_{h=0}^{\xi}\sum_{j=1}^{N} \overset{ij}{B}(t-\tau_h)\Delta \overset{jh}{D}_s + \sum_{h=0}^{\xi}\sum_{j=1}^{N} \overset{ij}{C}(t-\tau_h)\Delta \overset{jh}{q}_f + \sum_{h=0}^{\xi}\sum_{j=1}^{N} \overset{ij}{T}(t-\tau_h)\Delta \overset{jh}{h}_f \\
\overset{i}{\sigma}_s(t) &= \sum_{h=0}^{\xi}\sum_{j=1}^{N} \overset{ij}{E}(t-\tau_h)\Delta \overset{jh}{D}_n + \sum_{h=0}^{\xi}\sum_{j=1}^{N} \overset{ij}{F}(t-\tau_h)\Delta \overset{jh}{D}_s + \sum_{h=0}^{\xi}\sum_{j=1}^{N} \overset{ij}{G}(t-\tau_h)\Delta \overset{jh}{q}_f + \sum_{h=0}^{\xi}\sum_{j=1}^{N} \overset{ij}{T}(t-\tau_h)\Delta \overset{jh}{h}_f \\
\overset{i}{p}(t) &= \sum_{h=0}^{\xi}\sum_{j=1}^{N} \overset{ij}{K}(t-\tau_h)\Delta \overset{jh}{D}_n + \sum_{h=0}^{\xi}\sum_{j=1}^{N} \overset{ij}{L}(t-\tau_h)\Delta \overset{jh}{D}_s + \sum_{h=0}^{\xi}\sum_{j=1}^{N} \overset{ij}{M}(t-\tau_h)\Delta \overset{jh}{q}_f + \sum_{h=0}^{\xi}\sum_{j=1}^{N} \overset{ij}{T}(t-\tau_h)\Delta \overset{jh}{h}_f \\
\overset{i}{T}(t) &= \sum_{h=0}^{\xi}\sum_{j=1}^{N} \overset{ij}{T}(t-\tau_h)\Delta \overset{jh}{h}_f
\end{aligned}
\qquad \text{.....(3.15)}
$$

where h is the time step index (shown in Figure 3.5).

For the next time step, we have to subtract all previous influences from known boundary conditions at current time step. For example, for the normal stress,

$$\sum_{j=1}^{N} \overset{ij}{A}(t-\tau_\xi)\Delta \overset{j\xi}{D}_n + \sum_{j=1}^{N} \overset{ij}{B}(t-\tau_\xi)\Delta \overset{j\xi}{D}_s + \sum_{j=1}^{N} \overset{ij}{C}(t-\tau_\xi)\Delta \overset{j\xi}{q}_f + \sum_{j=1}^{N} \overset{ij}{T}(t-\tau_\xi)\Delta \overset{j\xi}{h}_f =$$

$$\overset{i}{\sigma}_n(\xi) - \sum_{h=0}^{\xi-1}\sum_{j=1}^{N} \overset{ij}{A}(t-\tau_h)\Delta \overset{jh}{D}_n - \sum_{h=0}^{\xi-1}\sum_{j=1}^{N} \overset{ij}{B}(t-\tau_h)\Delta \overset{jh}{D}_s - \sum_{h=0}^{\xi-1}\sum_{j=1}^{N} \overset{ij}{C}(t-\tau_h)\Delta \overset{jh}{q}_f \quad \text{.....(3.16)}$$

$$-\sum_{h=0}^{\xi-1}\sum_{j=1}^{N} \overset{ij}{T}(t-\tau_h)\Delta \overset{jh}{h}_f$$

For the shear stress,

$$\sum_{j=1}^{N} \overset{ij}{E}(t-\tau_\xi)\Delta \overset{j\xi}{D}_n + \sum_{j=1}^{N} \overset{ij}{F}(t-\tau_\xi)\Delta \overset{j\xi}{D}_s + \sum_{j=1}^{N} \overset{ij}{G}(t-\tau_\xi)\Delta \overset{j\xi}{q}_f + \sum_{j=1}^{N} \overset{ij}{T}(t-\tau_\xi)\Delta \overset{j\xi}{h}_f =$$

$$\overset{i}{\sigma}_s(\xi) - \sum_{h=0}^{\xi-1}\sum_{j=1}^{N} \overset{ij}{E}(t-\tau_h)\Delta \overset{jh}{D}_n - \sum_{h=0}^{\xi-1}\sum_{j=1}^{N} \overset{ij}{F}(t-\tau_h)\Delta \overset{jh}{D}_s - \sum_{h=0}^{\xi-1}\sum_{j=1}^{N} \overset{ij}{G}(t-\tau_h)\Delta \overset{jh}{q}_f \quad \text{.....(3.17)}$$

$$-\sum_{h=0}^{\xi-1}\sum_{j=1}^{N} \overset{ij}{T}(t-\tau_h)\Delta \overset{jh}{h}_f$$

For the pore pressure,

$$\sum_{j=1}^{N} \overset{ij}{K}(t-\tau_\xi)\Delta \overset{j\xi}{D}_n + \sum_{j=1}^{N} \overset{ij}{L}(t-\tau_\xi)\Delta \overset{j\xi}{D}_s + \sum_{j=1}^{N} \overset{ij}{M}(t-\tau_\xi)\Delta \overset{j\xi}{q}_f + \sum_{j=1}^{N} \overset{ij}{T}(t-\tau_\xi)\Delta \overset{j\xi}{h}_f =$$

$$\overset{i}{p}(\xi) - \sum_{h=0}^{\xi-1}\sum_{j=1}^{N} \overset{ij}{K}(t-\tau_h)\Delta \overset{jh}{D}_n - \sum_{h=0}^{\xi-1}\sum_{j=1}^{N} \overset{ij}{L}(t-\tau_h)\Delta \overset{jh}{D}_s - \sum_{h=0}^{\xi-1}\sum_{j=1}^{N} \overset{ij}{M}(t-\tau_h)\Delta \overset{jh}{q}_f \quad \text{.....(3.18)}$$

$$-\sum_{h=0}^{\xi-1}\sum_{j=1}^{N} \overset{ij}{T}(t-\tau_h)\Delta \overset{jh}{h}_f$$

As shown above, three types of equations in terms of normal stress, shear stress, and pore pressure can be established.

The temperature can be solved independently as shown in Eq. 3.19.

$$\sum_{j=1}^{N} \overset{ij}{T}(t-\tau_\xi)\Delta \overset{j\xi}{h}_f = \overset{i}{T}(\xi) - \sum_{h=0}^{\xi-1}\sum_{j=1}^{N} \overset{ij}{T}(t-\tau_h)\Delta \overset{jh}{h}_f \quad \text{.....(3.19)}$$

Then the increment of normal displacement discontinuity ($\Delta \overset{j\xi}{D}_n$), shear displacement discontinuity ($\Delta \overset{j\xi}{D}_s$), fluid flux ($\Delta \overset{j\xi}{q}_f$), and heat flux ($\Delta \overset{j\xi}{h}_f$) at time t can be determined from the previous sets of the algebraic equations shown in Eq. 3.16 to 3.19.

Finally the total normal displacement discontinuity ($\overset{j}{D}_n$), shear displacement discontinuity ($\overset{j}{D}_s$), fluid flux ($\overset{j}{q}_f$), and heat flux ($\overset{j}{h}_f$) on every fracture segment at time t can be obtained by summing all of the time step increments.

$$\overset{j}{D}_n = \sum_{h=0}^{\xi} \Delta \overset{jh}{D}_n \; ; \; \overset{j}{D}_s = \sum_{h=0}^{\xi} \Delta \overset{jh}{D}_s \; ; \; \overset{j}{q}_f = \sum_{h=0}^{\xi} \Delta \overset{jh}{q}_f \; ; \; \overset{j}{h}_f = \sum_{h=0}^{\xi} \Delta \overset{jh}{h}_f \quad \text{.....(3.20)}$$

3.5 Numerical verification of the displacement discontinuity method

3.5.1 The poroelastic response of a crack in rock (Mode I, II)

Consider a single horizontal, pressurized, stationary crack in an infinite poroelastic rock (Figure 3.6). The fracture half-length (a) is 1m. The crack surfaces are subjected to a suddenly applied constant and continuous fluid pressure p =1MPa at t =0. Assume that the infinite domain is initially at zero stress and pore pressure everywhere. Fifty equal-length constant poroelastic displacement discontinuity (DD) elements are used to discretize the crack boundary. According to Detournay and Cheng (1991), this problem can be decomposed into two sub-problems corresponding to two types of the loadings: Mode 1 (normal stress loading) and Mode 2 (pore pressure loading).

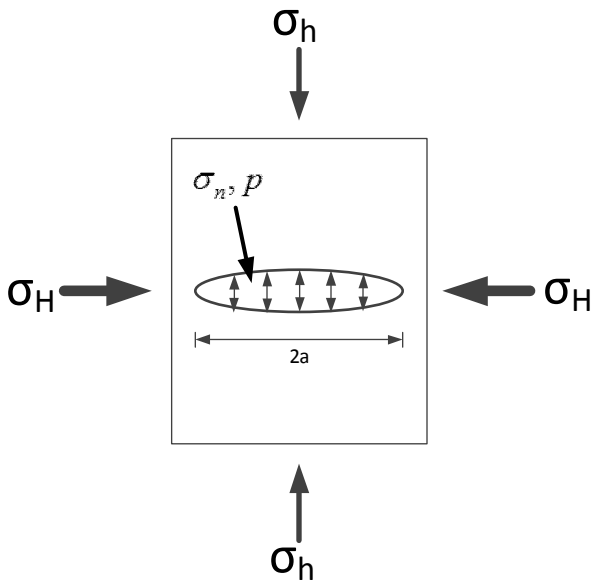

Figure 3.6 Horizontal pressurized crack in an infinite poroelastic rock

$$\text{Mode I: } \sigma_n(x,t) = pH(t), \quad p(x,t) = 0 \qquad \text{.....(3.21)}$$

$$\text{Mode II: } \sigma_n(x,t) = 0, \quad p(x,t) = pH(t) \qquad \text{.....(3.22)}$$

where $H(t)$ is the Heaviside step function. In this simulation, the rock is assumed to be Westerly Granite and all material parameters of this rock are used from the dataset listed in Rice and Cleary (1976) and shown in Table 3.1.

Table 3.1 Poroelastic properties of Westerly granite

Young's Modulus, E (GPa)	37.5
Poisson's ratio, ν	0.25
Undrained Poisson's ratio, ν_u	0.33
Solid bulk Modulus, K_s (GPa)	45
Fluid bulk Modulus, K_f (GPa)	2.5
Skempton's coefficient, B	0.815
Fluid diffusivity, c_f (m^2/s)	6.16×10^{-5}
Fluid viscosity, μ_f (Pa·s)	3.547×10^{-4}
Rock permeability, κ (m^2)	4.0×10^{-19}
Water density, ρ_w (kg/m^3)	1000
Biot's coefficient, α	0.444
Porosity, ϕ	0.01

Mode I loading is a total stress loading and causes the crack to open. The crack opening will cause a compression in the rock around the crack. At very early time ($t = 0^+$), the pore fluid cannot move out, and the rock response shows undrained behavior; as a result, the pore pressure around the crack instantly increases. And then the induced pore pressure starts to dissipate, decreasing with time until it reaches a drained stage with no pore pressure gradient. Figure 3.7 and 3.8 represent stresses and induced pore pressure contours around the crack under Mode I loading at very short time. The maximum tensile stresses are shown in the vicinity of the crack tip region, while the crack opening leads to compressive stresses on the top and bottom regions of the fracture. The induced pore pressure fell by 1MPa at the tip region while Skempton's effect increased it in the region of compression.

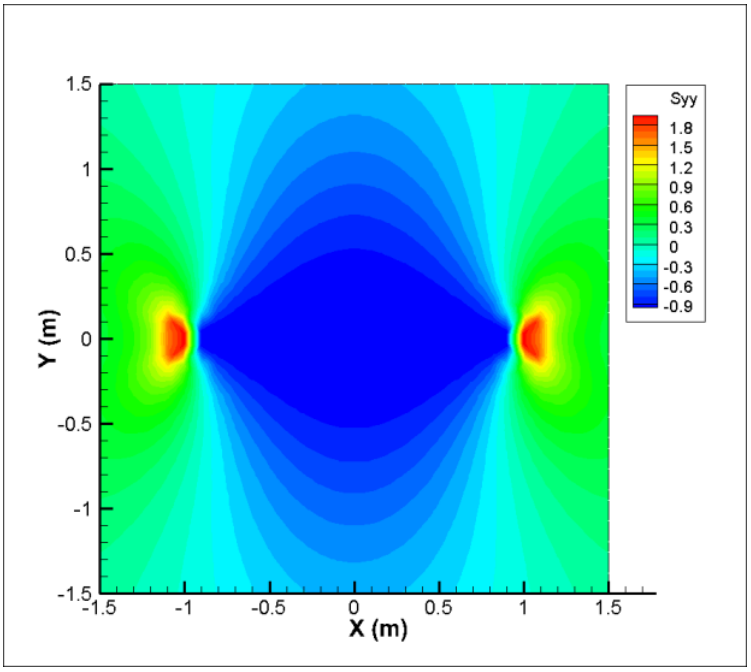

(a) σ_{yy}

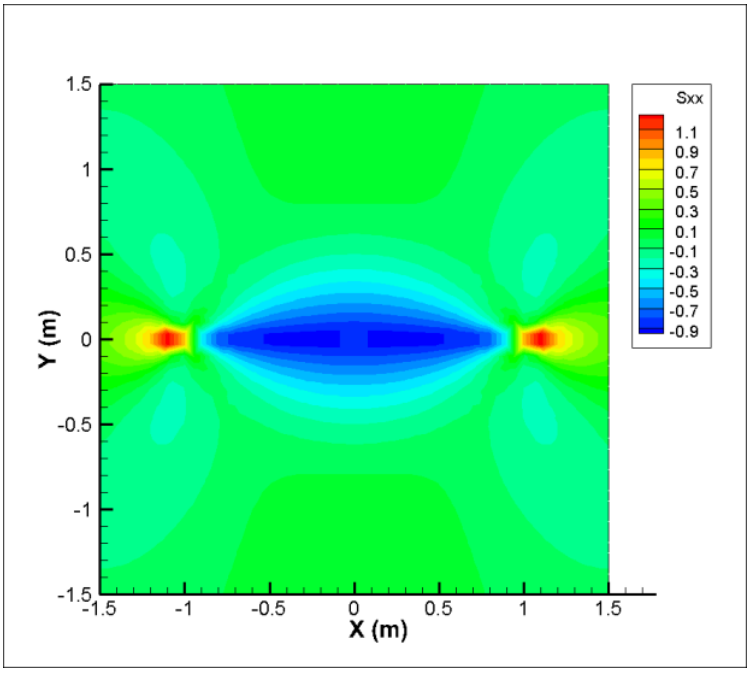

(b) σ_{xx}

Figure 3.7 Stress contours (MPa) under Mode I loading (applied σ_n on the crack surface) near single crack (a) σ_{yy} and (b) σ_{xx} at very short time ($t = 0^+$)

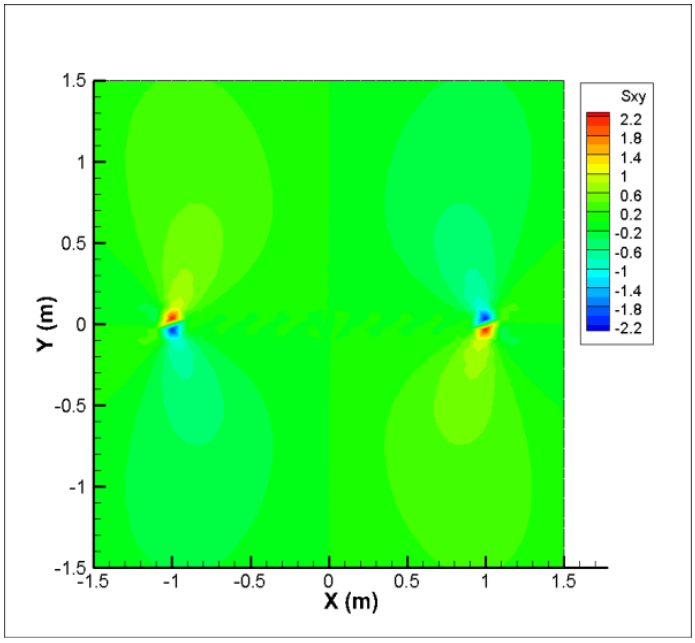

(a) σ_{xy}

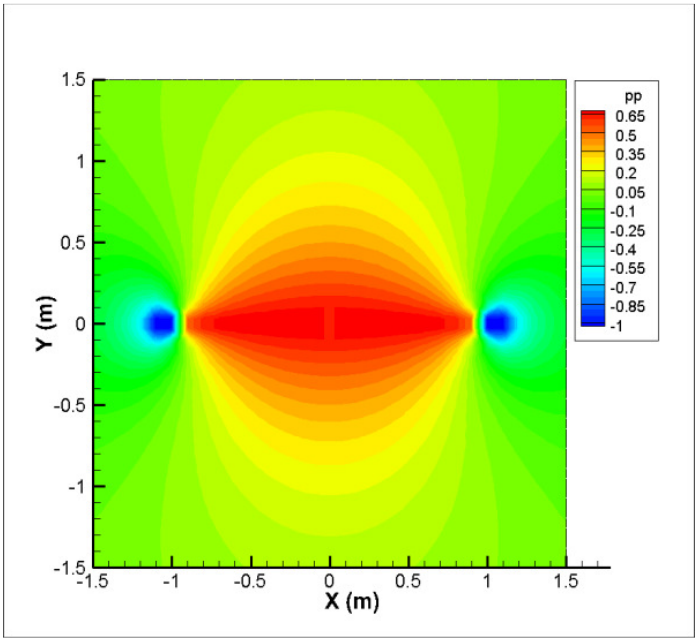

(b) induced pore pressure

Figure 3.8 Stress and pore pressure contours (MPa) under Mode I loading (applied σ_n on the crack surface) near single crack (a) σ_{xy} and (b) induced pore pressure at very short time ($t = 0^+$)

On the other hand, Figure 3.9 and 3.10 illustrate stresses and induced pore pressure contours around cracks under Mode I loading at very long time. As we can see, not all stress components change with time; they remain the same as under undrained conditions. However, the pore pressure has already dissipated into the rock formation, indicating the drainage stage.

The time-independent total stress distribution can be explained from Sneddon's analytical solution of a Griffith crack model (Sneddon 1946).

Eq.3.23 is the analytical distribution of total stress components in the vicinity of the crack tip in an elastic body for the constant pressurized crack problem.

$$\sigma_{xx} = p\sqrt{\frac{a}{2r}}\left[\frac{3}{4}\cos\frac{\theta}{2}+\frac{1}{4}\cos\frac{5\theta}{2}\right]$$
$$\sigma_{yy} = p\sqrt{\frac{a}{2r}}\left[\frac{5}{4}\cos\frac{\theta}{2}-\frac{1}{4}\cos\frac{5\theta}{2}\right] \quad \text{.....(3.23)}$$
$$\tau_{xy} = p\sqrt{\frac{a}{2r}}\left[\frac{1}{2}\sin\theta\cos\frac{3\theta}{2}\right]$$

where p is the internal pressure on the crack surface, a is the fracture half-length, r is distance from the crack tip and θ is the angle with respect to the plane of a crack.

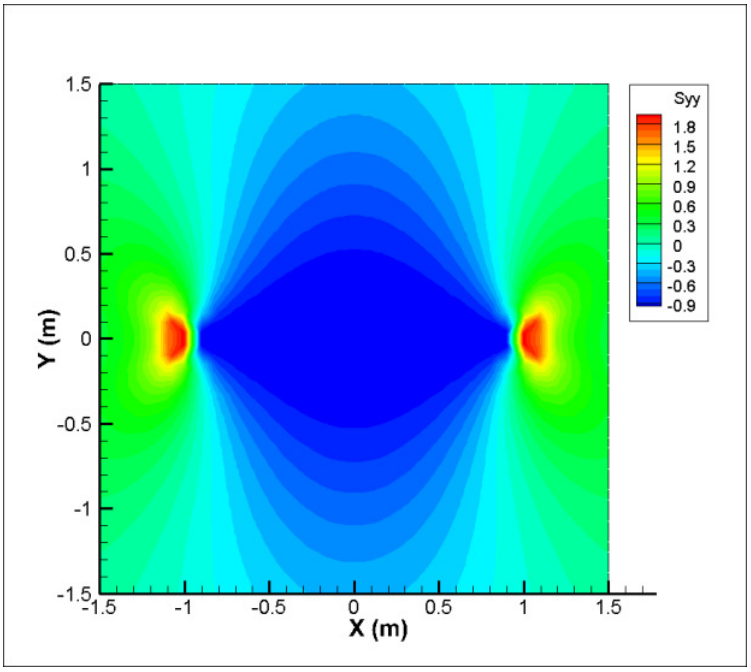

(a) σ_{yy}

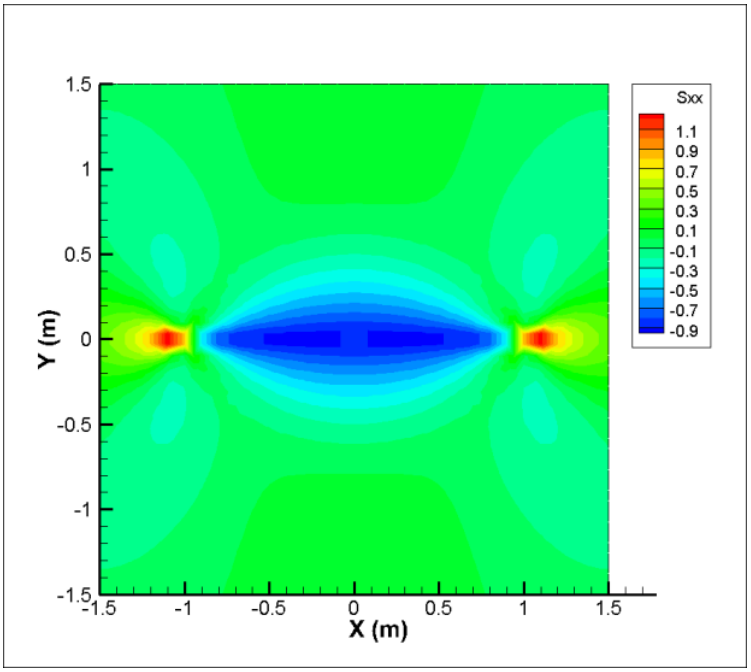

(b) σ_{xx}

Figure 3.9 Stress contours (MPa) under Mode I loading (applied σ_n on the crack surface) near single crack (a) σ_{yy} and (b) σ_{xx} at very long time

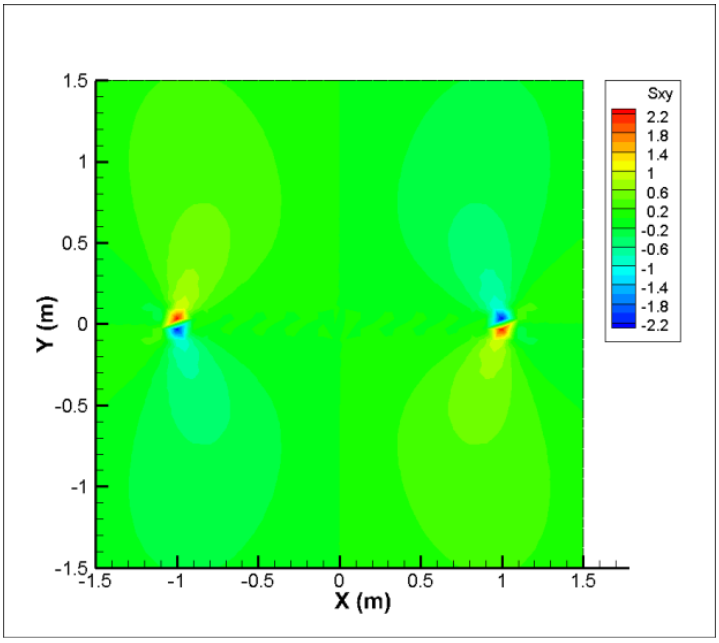

(a) σ_{xy}

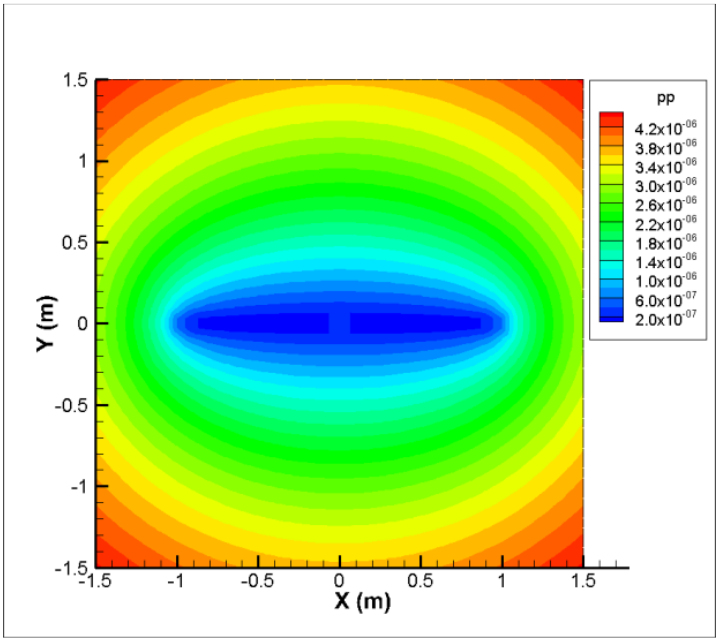

(b) induced pore pressure

Figure 3.10 Stress and pore pressure contours (MPa) under Mode I loading (applied σ_n on the crack surface) near single crack (a) σ_{xy} and (b) induced pore pressure at very long time

The total stress components are only proportional to the applied pressure p and fracture half-length a but they have nothing to do with the initial or induced pore pressure that has time-dependent characteristics. Therefore, the total stresses around the pressurized crack do not change with time, but the effective stresses can definitely change in compliance with variation in the induced pore pressure.

Mode II loading is likely to reduce the fracture opening as the fluid flows into the porous material around the crack, which means that the crack closes with time. It increases the pore pressure, which tends to cause an expansion of the porous material around the crack.

Figures 3.11 and 3.12 represent the stresses and induced pore pressure contours around cracks under Mode II loading at very long time. As can be seen, the pore pressure on the fracture surface is 1MPa as applied from the initial condition. From the stress contours, as the fluid is moving into the rock formation, the solid rock is subjected to compression, causing the fracture to close (Mode II effect).

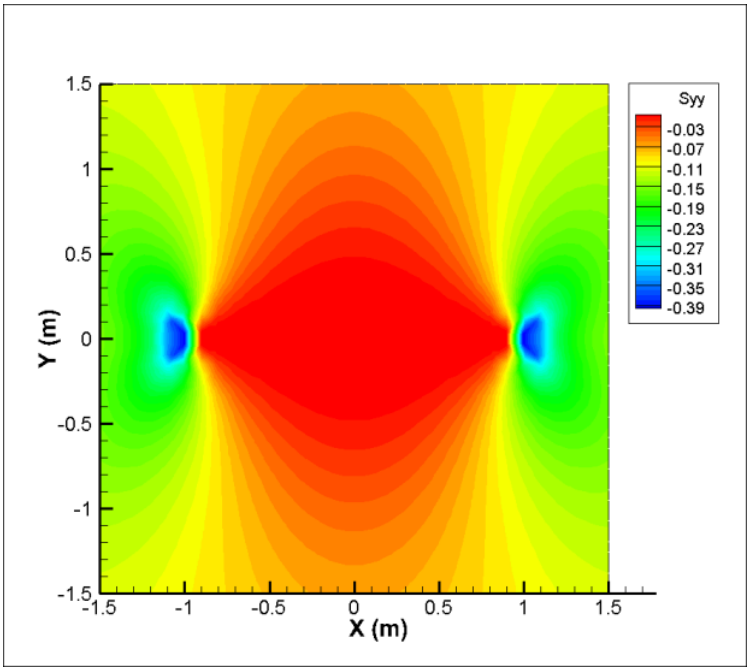

(a) σ_{yy}

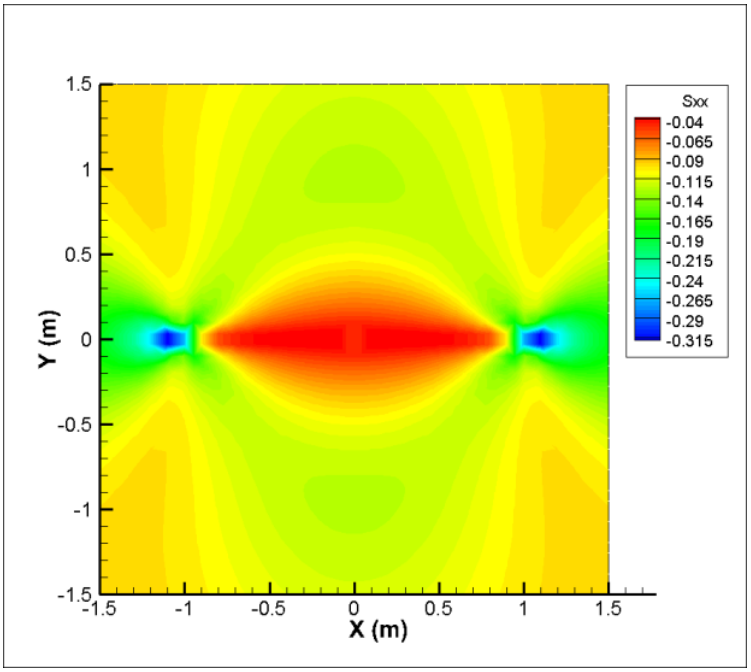

(b) σ_{xx}

Figure 3.11 Stress contours (MPa) under Mode II loading (applied p on the crack surface) near single crack (a) σ_{yy} and (b) σ_{xx} at very long time

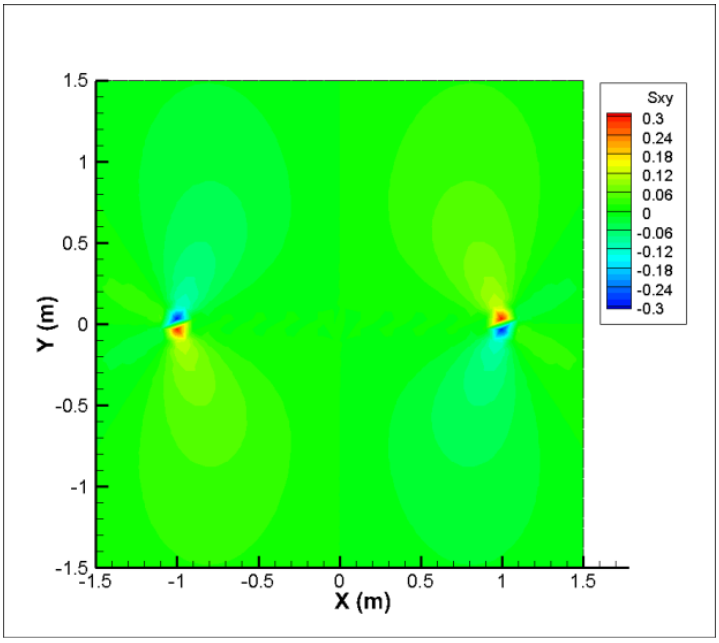

(a) σ_{xy}

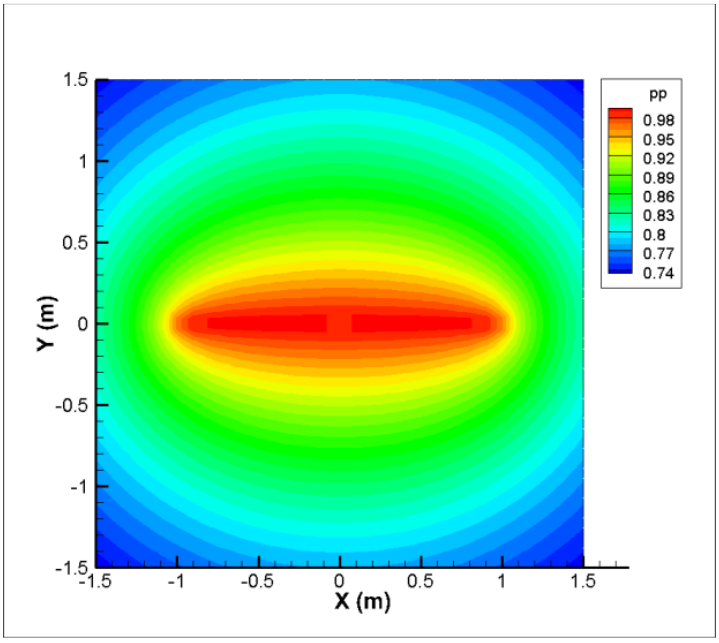

(b) induced pore pressure

Figure 3.12 Stress and pore pressure contours (MPa) under Mode II loading (applied p on the crack surface) near single crack (a) σ_{xy} and (b) induced pore pressure at very long time

Mode I loading represents a time-dependent opening of the crack. This transient crack opening can be calculated numerically by the 2D displacement discontinuity method and verified with the analytical solution of Sneddon (1946) and Detournay and Cheng (1991) with undrained (ν_u) and drained (ν) Poisson ratio.

In particular, the initial fracture opening is given by

$$w(x) = \frac{2pa(1-\nu_u)}{G}\sqrt{1-\frac{x^2}{a^2}} \quad \text{.....(3.24)}$$

The final fracture opening is given by

$$w(x) = \frac{2pa(1-\nu)}{G}\sqrt{1-\frac{x^2}{a^2}} \quad \text{.....(3.25)}$$

where p is pressure, a is half crack length and G is shear Modulus.

Figure 3.13 is the time-dependent fracture opening profile under Mode I loading. Initially the crack opening increases with time and then finally reaches steady-state at very long time. Figure 3.14 shows a negative fracture opening (crack closure) at very long time under Mode II loading. This crack closure reaches its maximum values in the middle of the crack at very long time when the pore pressure around the crack approaches the injected fluid pressure inside the crack.

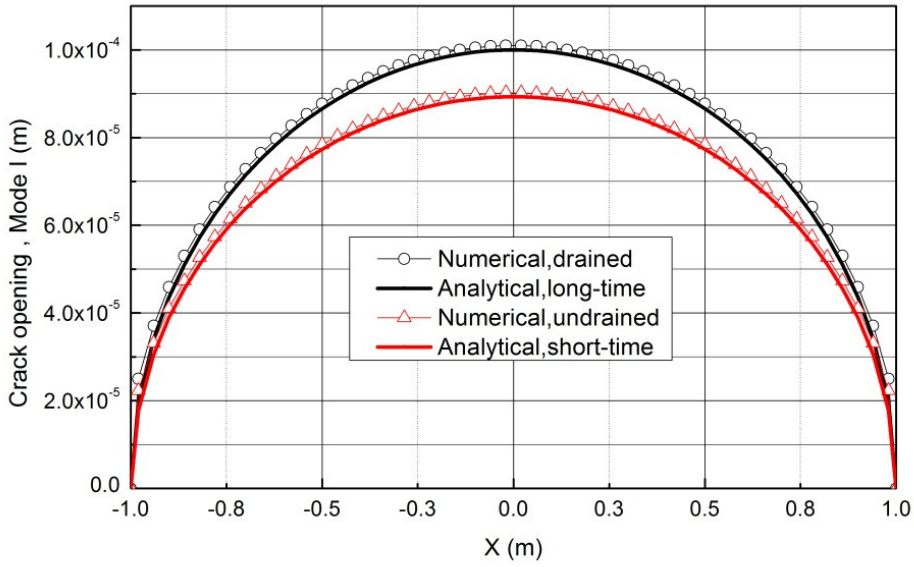

Figure 3.13 Comparison of the pressurized crack openings at short time (0.01sec) and long time (10^8sec) with analytical solution under Mode I loading

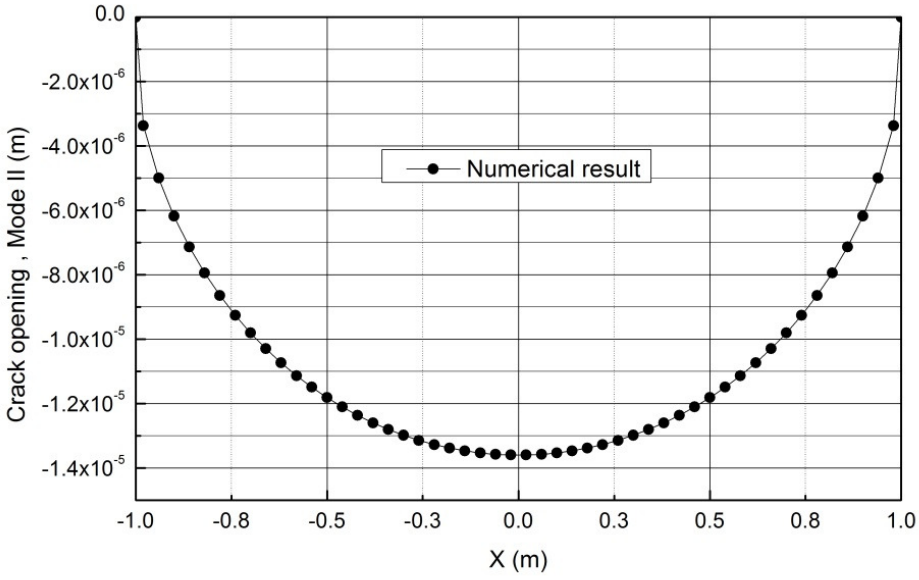

Figure 3.14 The crack closure at long time (10^8sec) under Mode II loading

3.5.2 The thermo-poroelastic response of a crack in rock (Mode III)

Now let us consider induced stresses and pore pressure distribution near a fracture in response to thermal loading. To investigate the effect of temperature on stresses and pore pressure, we assume that initial in-situ stress and pore pressure are zero everywhere. Figure 3.15 shows the single crack under thermal loading. The fracture half-length (a) is 1m. The reservoir temperature is 200^0C and the crack surfaces are suddenly cooled by injecting water and maintained at 0^0C. The crack response can be explained by the contraction of the rock formation as it cools, pulling the crack surfaces in opposite directions and gradually opening it.

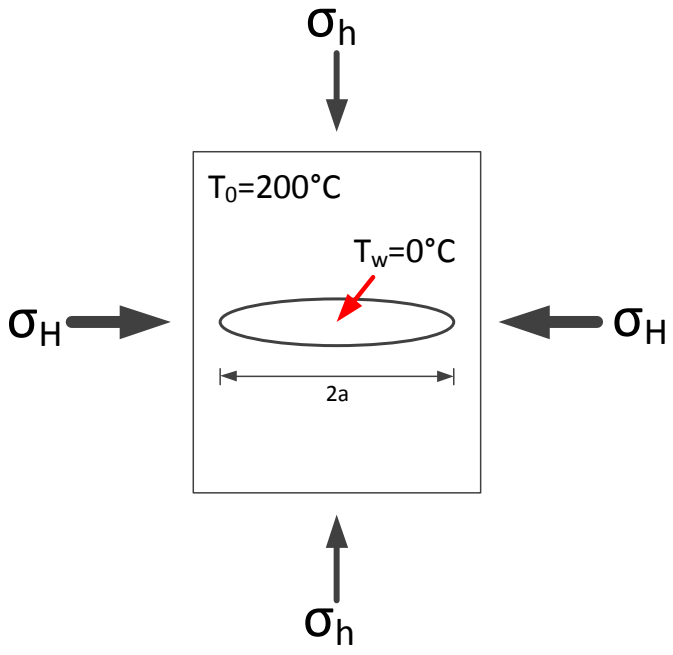

Figure 3.15 Horizontal crack under thermal loading in an infinite thermo-poroelastic rock

The thermoelastic properties for Westerly granite in this case are used from the dataset listed in the McTigue (1986) and shown in Table 3.2. The poroelastic ones are the same as the previous examples (see Table 3.1).

Table 3.2 Thermoelastic properties of Westerly granite

Rock thermal expansion coefficient, β_s [m/(m·°C)]	24×10^{-6}
Fluid thermal expansion coefficient, β_f [m/(m·°C)]	3.0×10^{-4}
Rock thermal diffusivity, c^T (m^2/s)	5.1×10^{-6}
Rock density, ρ_r (kg/m^3)	2650
Water density, ρ_w (kg/m^3)	1000
Rock heat capacity, c_r (J/kg·K)	790
Water heat capacity, c_w (J/kg·K)	4200

Figure 3.16 shows the induced stresses contours under Mode III loading at 10^5 sec. For the overall stress contour, tensile stress highly induced by cooling is acting around the fracture, which is much higher than the stresses under Mode I or II loading. This phenomenon tells us that the effect of cooling around the fracture on the induced stresses over a relatively long time is much more significant than the injection of fluid pressure along the fracture (Mode I+II). Also it indicates that high tensile stress would initiate and propagate thermal cracking under thermal loading if it exceeds the tensile strength of the rock.

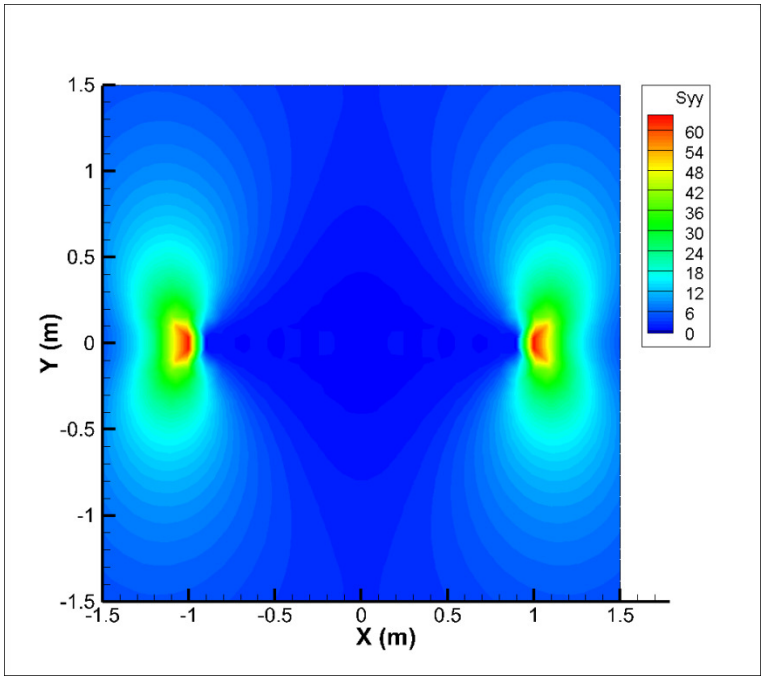

(a) σ_{yy}

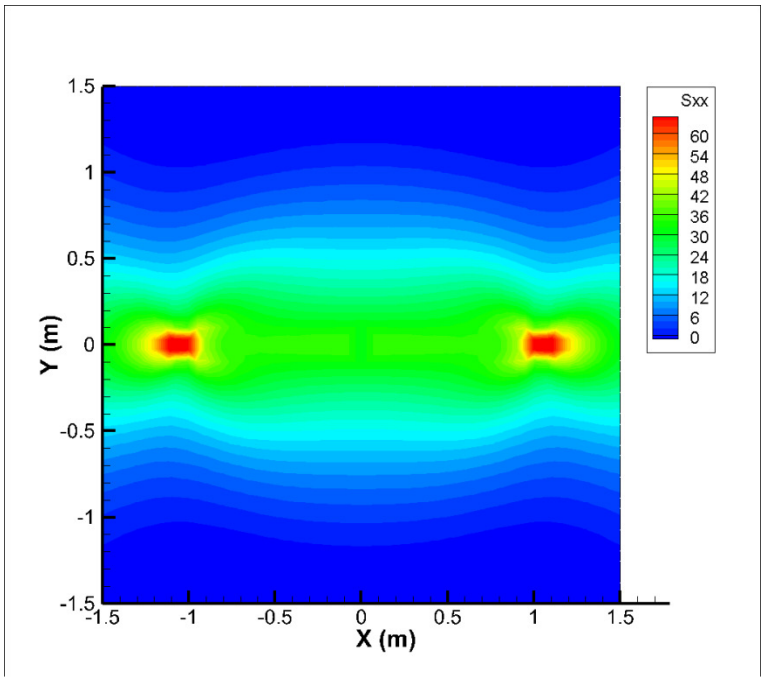

(b) σ_{xx}

Figure 3.16 Stress contours (MPa) under Mode III loading near single crack (a) σ_{yy} and (b) σ_{xx} at 10^5 sec

The analytical solution for stress components of thermal loading at very long time ($t \to \infty$) is given by Zhang (2004):

$$\sigma_{xx} = \sigma_{yy} = -\frac{E\beta_s}{6(1-\nu)}\Delta T \quad \text{.....(3.26)}$$

Eq. 3.26 indicates that the stress components by temperature change are equivalent over long periods of time, showing good agreement with numerical results shown in Figure 3.16.

Meanwhile, this thermal effect also induces pore pressure changes around the fracture. Figure 3.17 shows transient pore pressure distribution around a crack, indicating that the cooling induces significant decreases in pore pressure near crack region after 2 hours, but it also restores the pore pressure after the cooling front has passed from the near fracture. The pore pressure finally stabilizes after 10^8 sec.

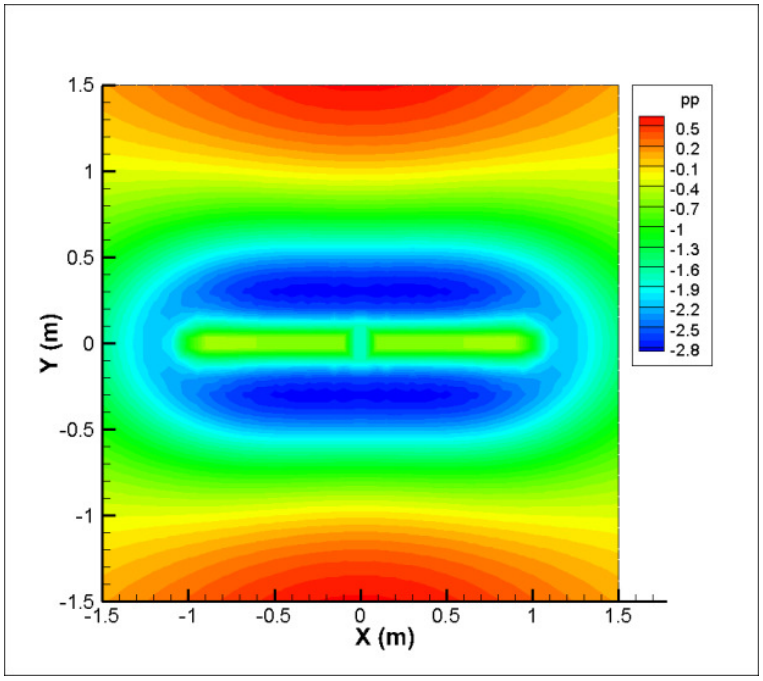

(a) t=7200sec

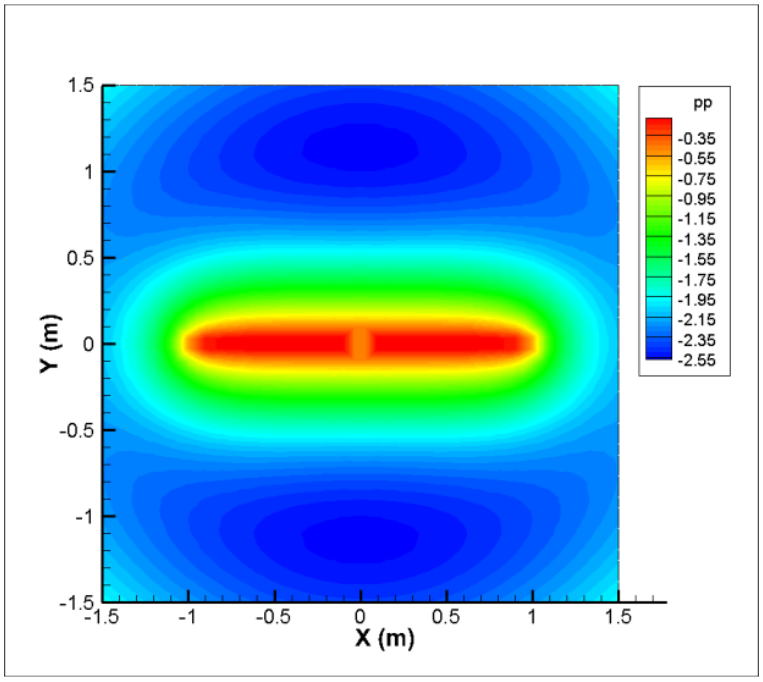

(b) t=10^5sec

Figure 3.17 Pore pressure contours (MPa) under Mode III loading (a) t=7200sec (b) t=10^5sec and (c) t=10^8sec

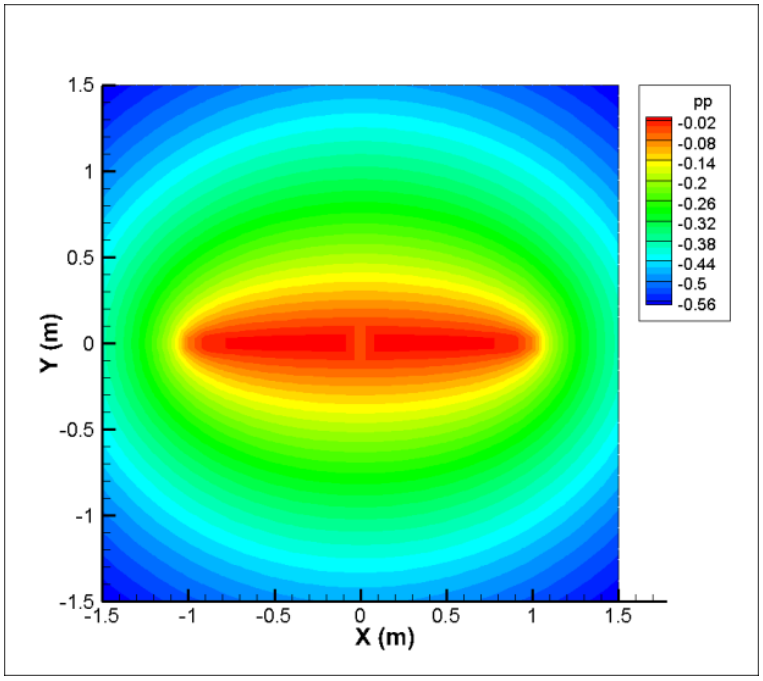

(c) t=10^8sec

Figure 3.17 Continued

3.5.3 The transient maximum crack aperture

The transient maximum crack aperture for poroelastic or thermo-poroelastic responses can be captured at the center of crack as a function of time. In this case, we assumed that initial pore pressure (P_0) was 5 MPa and fluid pressure (p) applied on the fracture surface was 10 MPa. Figure 3.18 shows the fracture opening at its center (maximum) in response to Mode I loading. Initially, the fracture opens with time and reaches a stabilized, positive value after a long time.

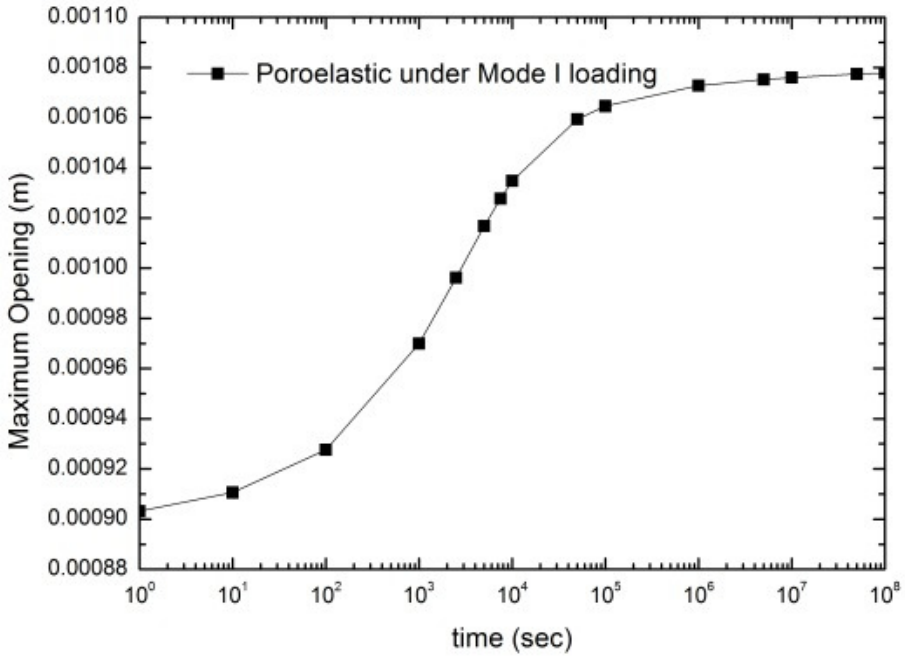

Figure 3.18 The crack opening at its center as a function of time under Mode I loading

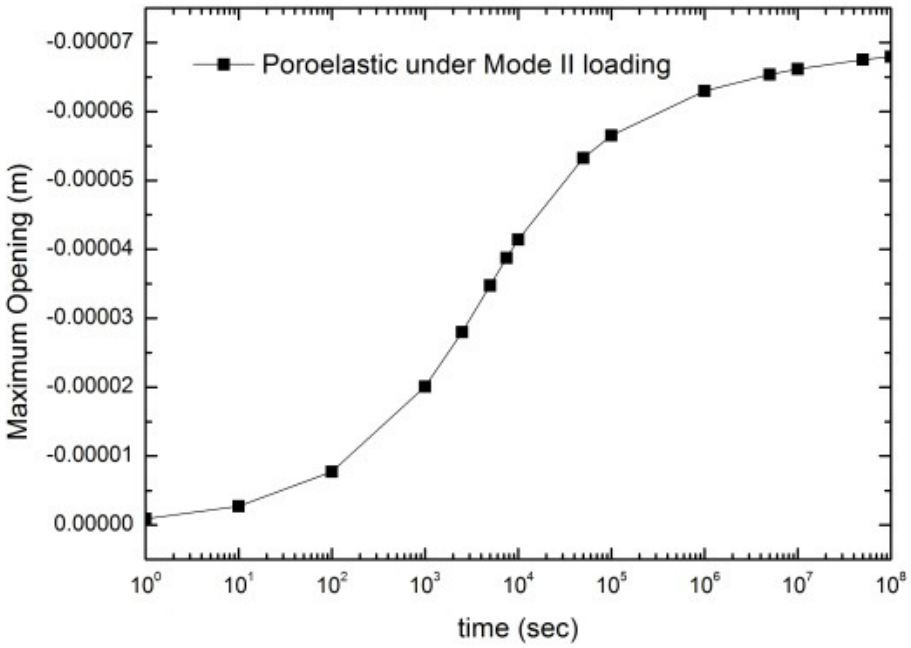

Figure 3.19 The crack closure at its center as a function of time under Mode II loading

Figure 3.19 shows the maximum fracture closure at the center of the crack in response to Mode II loading. The fracture progressively closes, starting from zero and approaching a constant negative value after a long time. Also the fracture closure in response to Mode II loading is smaller than the opening induced by Mode I loading. These two are caused by that the pore pressure diffusion as rock moves from the undrained to drained state.

Figure 3.20 shows the fracture opening at its center (maximum) in response to Mode I+II loading. The poroelastic nature of maximum crack opening in the combined

loading has a trend similar to Mode I loading with slightly less fracture aperture due to the closure of crack induced by Mode II loading.

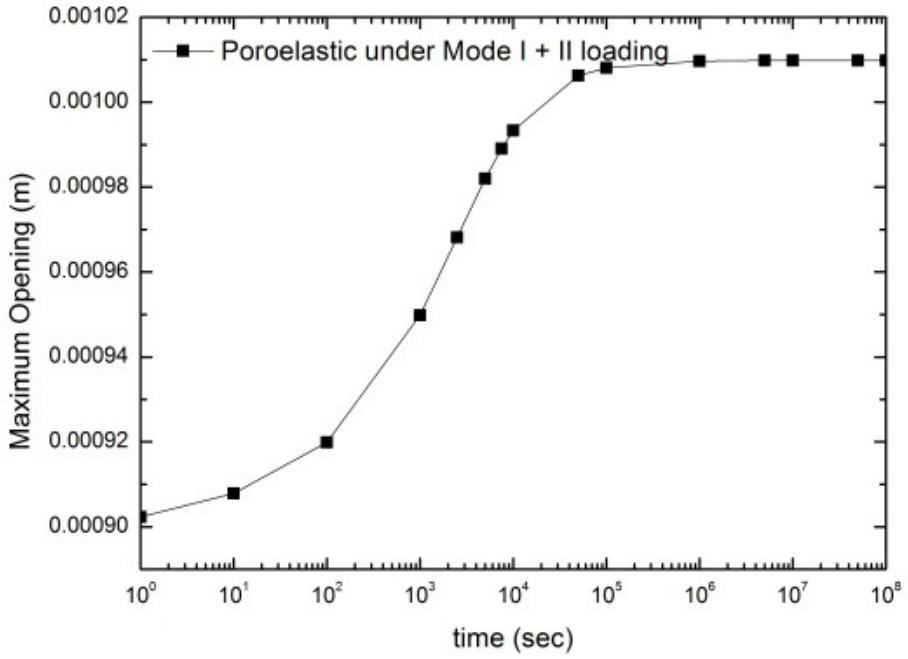

Figure 3.20 The crack opening at its center as a function of time under Mode I+II loading

Figure 3.21 shows the fracture opening at its center (maximum) in response to Mode III loading (ΔT=-200°C), illustrating how cooling on the crack surfaces and the surrounding rock results in opening of the fracture. This is an opposite effect of Mode II loading that allows the crack to be closed. Also, cooling in the fracture dramatically increases the fracture aperture, depending on the temperature change and the rock thermal expansion coefficient.

The asymptotic value at very long time is given by Detournay and Cheng (1991):

$$w_{\max} = -\frac{2\beta_s a(1+\nu)}{3}\Delta T \quad \text{.....(3.27)}$$

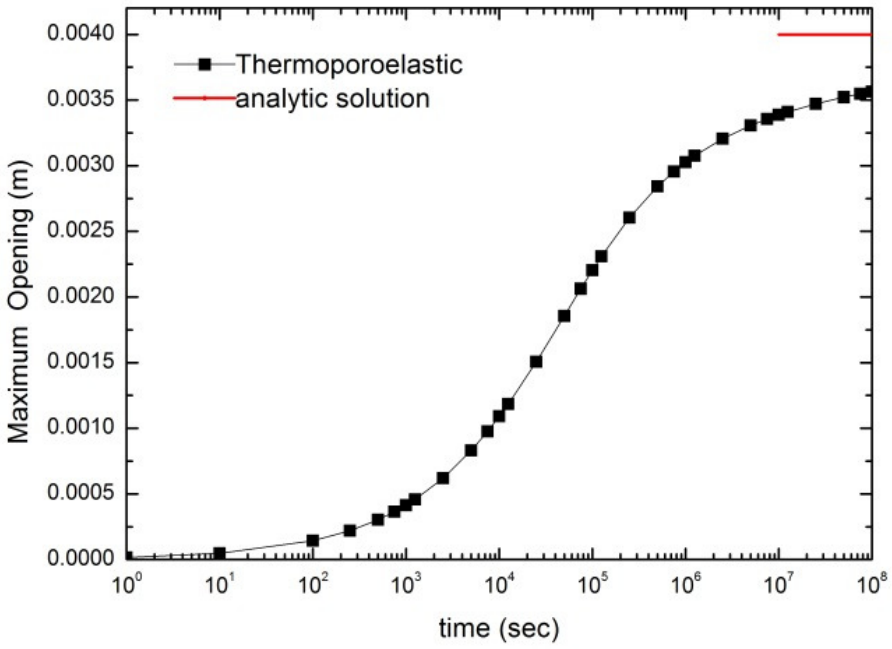

Figure 3.21 The crack opening at its center as a function of time under Mode III loading

3.5.4 The poroelastic and thermo-poroelastic stress intensity factor

Stress intensity factor (K) is used in linear elastic fracture mechanics to predict the stress state (intensity) near the crack tip caused by external loadings (Anderson 2005). It is usually applied to a homogeneous, isotropic, linear elastic material but also is effective in poroelastic or thermo-poroelastic problems.

Atkinson and Craster (1991) showed that an asymptotic elastic stress intensity factor accurately predicts transient behavior of itself in poroelastic media. Sih (1962) showed that the order of singularity predicted by thermoelastic stress is the same as that by mechanical stresses. And John et al. (1992) demonstrated by their experiment that the thermoelastic stress intensity factor has same effect as the mechanical stress intensity factor with respect to the crack. Hence, it is natural that we can apply the elastic stress intensity factor to poroelastic or thermo-poroelastic problem.

Figure 3.22 shows the stress intensity factor computed at the center of the crack tip under Mode I loading. As time goes to infinity, the excess pore pressure around the crack is totally drained; consequently, the response of the stress intensity factor approaches that of an elastic material and behaves in a softer manner.

However, at very small time, the pore fluid toward the crack tip lowers the stress intensity factor, effectively reducing the energy available to initiate a fracture in the vicinity of the crack tip.

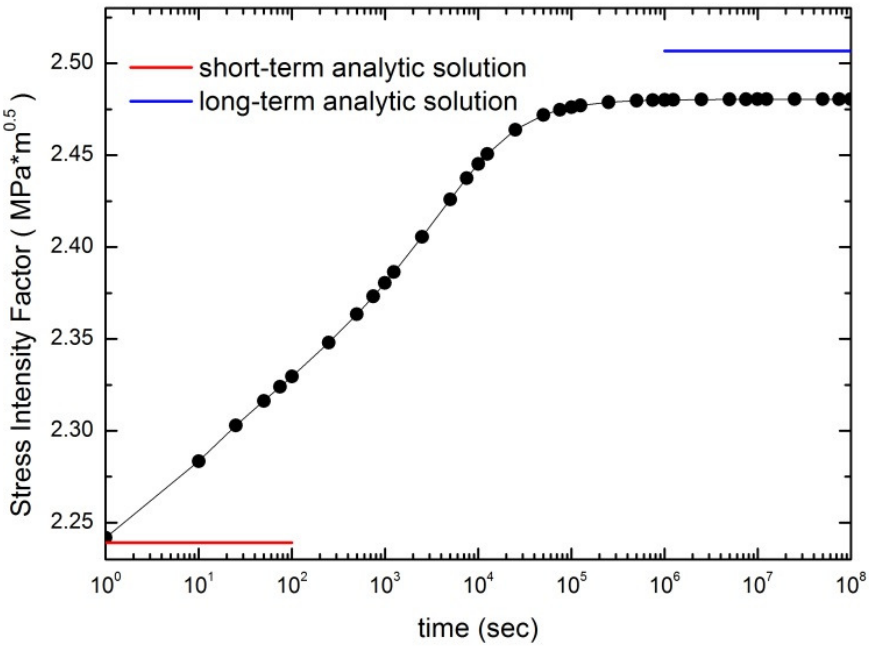

Figure 3.22 Stress intensity factor as a function of time under Mode I loading

The initial (short-term) value of stress intensity factor is given by Detournay and Cheng (1991):

$$K_{\mathrm{I}}(0^{+}) = \frac{(1-\nu_u)}{1-\nu}\sqrt{\pi a} \quad \text{.....(3.28)}$$

The final (long-term) value of stress intensity factor is also given by Detournay and Cheng (1991):

$$K_{\mathrm{I}}(\infty) = K_{\mathrm{I}}(\text{elastic}) = \sqrt{\pi a} \quad \text{.....(3.29)}$$

The stress intensity factor under Mode III loading (Figure 3.23) illustrates that the cooling in the crack surface and surrounding rock gives rise to significant increase in the stress intensity factor near the crack tip for a much longer time than under Mode I loading. This implies us that the cooling can cause creation of high, thermally induced stresses around the crack, causing the thermal fracturing process.

The stress intensity factor approaching asymptotic values in the steady-state is given by Zhang (2004):

$$K_I(\infty) = -\frac{E\beta_s}{6(1-\nu)}\Delta T\sqrt{\pi a} \quad \text{.....(3.30)}$$

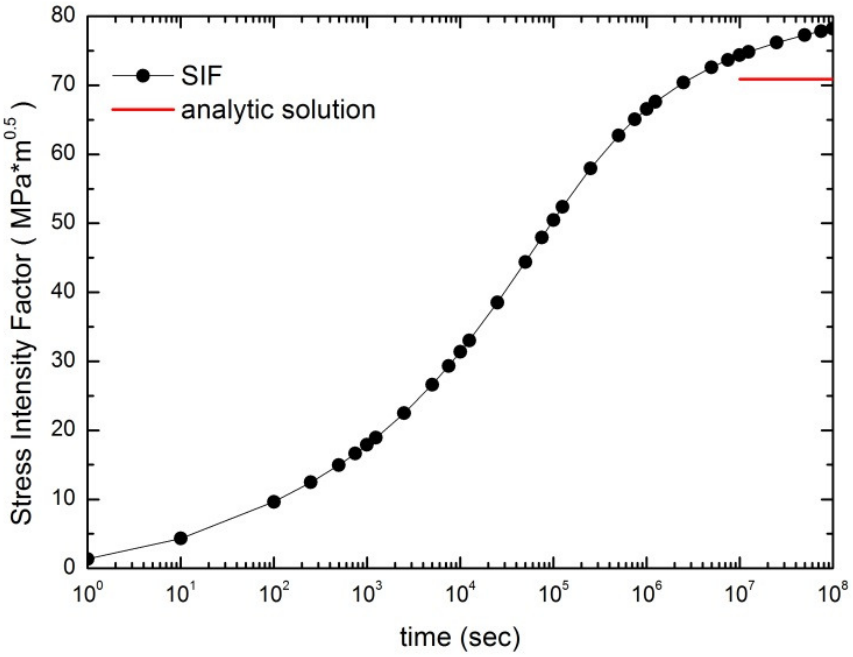

Figure 3.23 Stress intensity factor as a function of time under Mode III loading

4. FRACTURE PROPAGATION IN ELASTIC ROCK

4.1 Introduction

Hydraulic fracturing has been widely used for about 60 years in the petroleum industry to enhance oil and gas recovery from unconventional reservoirs. The hydraulic fracturing usually takes place when the fluid pressure inside the fracture or borehole exceeds the minor principal stress plus the tensile strengh of the rock. Artificial or man-made hydraulic fractures in unconventional resources are normally initiated by increasing the fluid pressure around the borehole to the point where the minor principal stress becomes tensile. Continued fluid pumping at an elevated pressure enables the formation to split, and the hydraulic fracture can propagate in the direction normal to the minimum principal stress in the rock formation.

Meanwhile, advances in the field of linear elastic fracture mechanics (LEFM) have helped geophysicists and geomechacnis engineers to understand rock fractures in the earth's crust (Atkinson 1987). In essence, LEFM concerns the study of stress concentrations caused by sharp cracks and the conditions for the propagation of these flaws. A criterion based on strong physical backgrounds or experimental evidence is used to predict whether a crack or discontinuity will propagate or not in rock.

In this section, we focus on the fracture propagation of elastic rocks. First, for that we will provide a review of fracture mechanics based on the LEFM theory. Second, the stress intensity factor is introduced to get the crack extension criterion and is evaluated to increase numerical accuracy. Third, we discuss the description of crack

propagation criterion to determine under which condition the crack will propagate as well as the direction of propagation. Finally, we show several elastic fracture propagation examples to predict how they will behave under certain boundary conditions.

4.2 Linear elastic fracture mechanics

This section defines basic concepts and terminologies within the linear elastic fracture mechanics (LEFM) theory as the fundamental step to incorporate fracture propagation modeling procedures. Thus the review discusses basic terms and methodologies to describe the behavior of cracks briefly.

4.2.1 Stress analysis of cracks

Figure 4.1 illustrates the stress components in the vicinity of the crack tip in two-dimensional problems for a homogeneous, linear elastic medium.

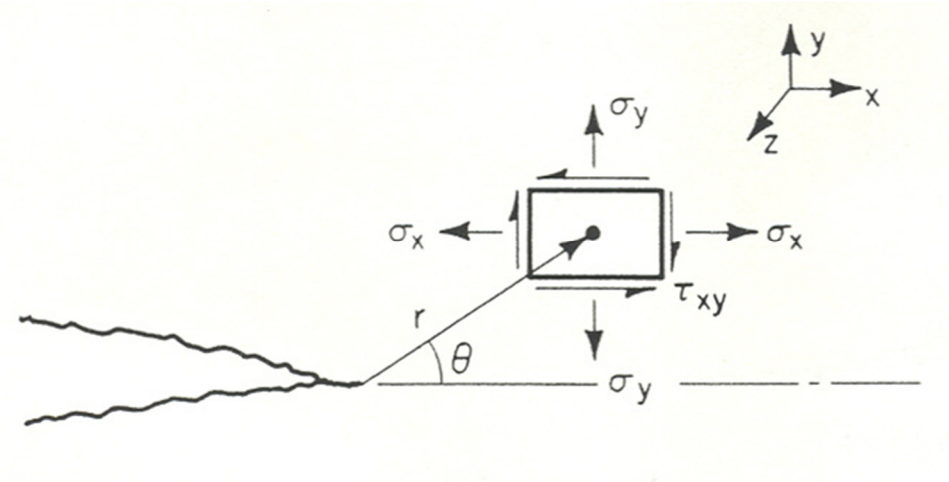

Figure 4.1 Coordinate axis ahead of a crack tip for linear elastic crack tip stress field (Anderson 2005)

According to the linear elastic fracture mechanics (LEFM), the stress field at the crack tip in elastic body is given for plane strain condition by (Irwin 1957)

$$\sigma_{ij} = \frac{K}{\sqrt{2\pi r}} f_{ij}(\theta) + \text{other terms} \quad \text{..... (4.1)}$$

where f_{ij} is a dimensionless function, r is distance from the crack tip, and θ is the angle with respect to the plane of a crack. As the coordinate r approaches zero, the leading term in Eq. 4.1 dominates, but the other terms tend to zero. The parameter K is the stress intensity factor. It therefore follows that the stress field near the crack tip can be characterized by the stress intensity factor.

4.2.2 Fracture modes

According to LEFM, we can distinguish several ways that external forces may be applied to the rock, enabling the crack to propagate. Irwin (1957) proposed classification corresponding to the three different types of loadings represented in Figure 4.2. Accordingly, we can consider three distinct modes: Mode I, Mode II, and Mode III.

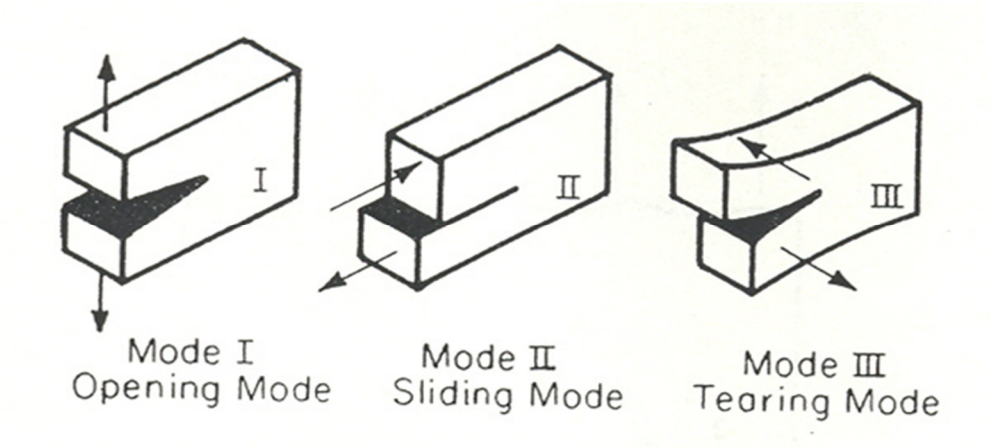

Figure 4.2 Three types of fracture modes (Anderson 2005)

In Mode I (opening mode), the cracked body is loaded normal to the crack plane by tensile forces, such that the crack surfaces are pulled apart normal to the loading direction which enables the crack open.

In Mode II (sliding mode), the cracked body is loaded by shear forces parallel to the crack surfaces, which slide over each other in the direction of loading.

In Mode III (tearing mode), the cracked body is loaded by shear forces parallel to the crack front and the crack surfaces slide over each other out of the plane direction.

Detailed mathematical expressions for the singular stress fields for Modes I, II, and III in two-dimensional problems for the plane strain assumption follow.

For Mode I (Opening)

$$\sigma_{xx} = \frac{K_{\mathrm{I}}}{\sqrt{2\pi r}}\cos\left(\frac{\theta}{2}\right)\left[1-\sin\frac{\theta}{2}\sin\frac{3\theta}{2}\right]$$
$$\sigma_{yy} = \frac{K_{\mathrm{I}}}{\sqrt{2\pi r}}\cos\left(\frac{\theta}{2}\right)\left[1+\sin\frac{\theta}{2}\sin\frac{3\theta}{2}\right] \quad \text{..... (4.2)}$$
$$\tau_{xy} = \frac{K_{\mathrm{I}}}{\sqrt{2\pi r}}\cos\left(\frac{\theta}{2}\right)\sin\left(\frac{\theta}{2}\right)\cos\left(\frac{3\theta}{2}\right)$$

For Mode II (In-plane shear)

$$\sigma_{xx} = -\frac{K_{\mathrm{II}}}{\sqrt{2\pi r}}\sin\left(\frac{\theta}{2}\right)\left[2+\cos\frac{\theta}{2}\cos\frac{3\theta}{2}\right]$$
$$\sigma_{yy} = \frac{K_{\mathrm{II}}}{\sqrt{2\pi r}}\sin\left(\frac{\theta}{2}\right)\cos\left(\frac{\theta}{2}\right)\cos\left(\frac{3\theta}{2}\right) \quad \text{..... (4.3)}$$
$$\tau_{xy} = \frac{K_{\mathrm{II}}}{\sqrt{2\pi r}}\cos\left(\frac{\theta}{2}\right)\left[1-\sin\frac{\theta}{2}\sin\frac{3\theta}{2}\right]$$

For Mode III (Out of plane shear)

$$\tau_{xz} = -\frac{K_{\mathrm{III}}}{\sqrt{2\pi r}}\sin\left(\frac{\theta}{2}\right)$$
$$\tau_{yz} = \frac{K_{\mathrm{III}}}{\sqrt{2\pi r}}\cos\left(\frac{\theta}{2}\right) \quad \text{..... (4.4)}$$

where $K_{\mathrm{I}}, K_{\mathrm{II}}, K_{\mathrm{III}}$ is stress intensity factor under Mode I, II , and III, respectively.

In mixed mode problems (that is, when more than one type of loading is applied), the individual contributions to a given stress component should be taken into account based on the principle of linear stress superposition. For example, if σ_{ij}^{I}, $\sigma_{ij}^{\mathrm{II}}$, $\sigma_{ij}^{\mathrm{III}}$ are respectively the stress components associated to modes I, II, and III, then the total stress component $\sigma_{ij}^{\mathrm{total}}$ is given by

$$\sigma_{ij}^{\mathrm{total}} = \sigma_{ij}^{\mathrm{I}} + \sigma_{ij}^{\mathrm{II}} + \sigma_{ij}^{\mathrm{III}} \quad \text{..... (4.5)}$$

4.3 Stress intensity factor

4.3.1 Numerical approach

Stress intensity factor (*K*) is the main characterization parameter in fracture mechanics to predict the stress state (intensity) near the crack tip caused by various types of external loading. It is usually applied to a homogeneous, isotropic, linear elastic material, but it is also useful for providing a crack propagation criterion for brittle materials (Atkinson 1987).

The magnitude of stress intensity factor depends on material geometry, flaw size and location of the crack, and the magnitude of loadings on the material (Anderson 2005), and it can be determined by both analytical and numerical methods. Numerical methods such as boundary element methods have been adopted to compute stress intensity factor for a wide range of engineering problems (Aliabadi and Rooke 1991).

In particular, in the discontinuity displacement method, the stress intensity factor is computed using a one-point formulation by using displacements obtained at the nodes inside the elements. The formulations are given by Shou and Crouch (1995):

$$K_{\mathrm{I}} = \frac{G}{4(1-\nu)}\sqrt{\frac{2\pi}{r}}D_n(r) \quad \text{..... (4.6)}$$

$$K_{\mathrm{II}} = \frac{G}{4(1-\nu)}\sqrt{\frac{2\pi}{r}}D_s(r) \quad \text{..... (4.7)}$$

where D_n and D_s are the normal and shear components of displacement discontinuity, and r is the distance from the point where D_n and D_s are calculated to the crack tip.

4.3.2 Numerical verification

In this section, we present sensitivity analysis to demonstrate the effect of crack tip length on the accuracy of computed numerical stress intensity factor by comparing analytic solutions.

Consider the analysis of a slanted straight crack in an elastic medium, shown in Figure 4.3. The crack has a length 2a and makes an angle β with the direction of applied uniaxial stress at infinity. In this case, the analytical stress intensity factors K_{I} and K_{II} are given by (Dong and de Pater 2001)

$$K_{\mathrm{I}} = \sigma\sqrt{\pi a}\sin^2\beta \quad \text{..... (4.8)}$$

$$K_{\mathrm{II}} = \sigma\sqrt{\pi a}\sin\beta\cos\beta \quad \text{..... (4.9)}$$

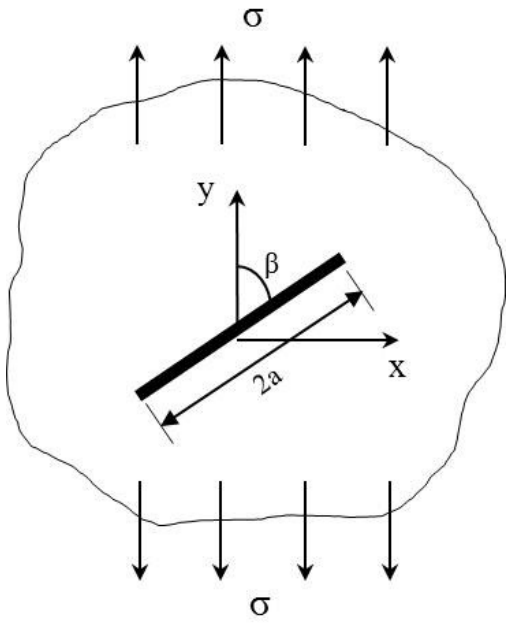

Figure 4.3 Slanted straight crack under uniform tension at infinity

In this analysis, 8, 10, and 20 constant displacement discontinuity (DD) elements (including 1 elastic tip element) with equal length were used for the discretization of the crack surfaces. Input parameters are shown in Table 4.1 and comparisons between analytical and numerical results are tabulated from Table 4.2 through 4.4. As shown in these tables, the numerical errors of K_{I} and K_{II} slightly increase with the larger number of elements but show relatively high accuracy. Also they demonstrate the same values of numerical error regardless of slanted angle, which indicates reasonable consistency in the numerical computation. With these results, we can determine and use optimized crack tip element length through sensitivity analysis, which allows us to perform more accurate numerical modeling of fracture problems in the rock mechanics field.

Table 4.1 Input parameters

Young's Modulus, E (kPa)	10
Poisson's ratio, ν	0.1
half crack length, a (m)	1.0
uniaxial stress, σ (Pa)	1.0

Table 4.2 Numerical and analytical stress intensity factor with 8 DD elements

Total 8 elements (7 constant + 1 tip element)								
	Analytical	Analytical	Analytical	Numerical	Numerical	Numerical	Error (%)	Error (%)
Slanted Angle(°)	KI	KII	KII/KI	KI	KII	KII/KI	KI	KII
30	0.4431	0.7675	1.7321	0.4726	0.8186	1.7320	6.66%	6.66%
45	0.8862	0.8862	1.0000	0.9453	0.9453	1.0000	6.66%	6.66%
60	1.3293	0.7675	0.5774	1.4179	0.8186	0.5774	6.66%	6.66%
90	1.7725	0.0000	0.0000	1.8905	0.0000	0.0000	6.66%	0.00%

Table 4.3 Numerical and analytical stress intensity factor with 10 DD elements

Total 10 elements (9 constant + 1 tip element)								
	Analytical	Analytical	Analytical	Numerical	Numerical	Numerical	Error (%)	Error (%)
Slanted Angle(°)	KI	KII	KII/KI	KI	KII	KII/KI	KI	KII
30	0.4431	0.7675	1.7321	0.4739	0.8207	1.7320	6.94%	6.94%
45	0.8862	0.8862	1.0000	0.9477	0.9477	1.0000	6.94%	6.94%
60	1.3293	0.7675	0.5774	1.4215	0.8207	0.5774	6.94%	6.94%
90	1.7725	0.0000	0.0000	1.8954	0.0000	0.0000	6.94%	0.00%

Table 4.4 Numerical and analytical stress intensity factor with 20 DD elements

Total 20 elements (19 constant + 1 tip element)								
	Analytical	Analytical	Analytical	Numerical	Numerical	Numerical	Error (%)	Error (%)
Slanted Angle(°)	KI	KII	KII/KI	KI	KII	KII/KI	KI	KII
30	0.4431	0.7675	1.7321	0.4763	0.8250	1.7320	7.49%	7.49%
45	0.8862	0.8862	1.0000	0.9526	0.9526	1.0000	7.49%	7.49%
60	1.3293	0.7675	0.5774	1.4288	0.8250	0.5774	7.49%	7.49%
90	1.7725	0.0000	0.0000	1.9051	0.0000	0.0000	7.49%	0.00%

4.4 The elastic crack tip displacement discontinuity element

In this section, the general description of the elastic crack tip displacement discontinuity element for accurate crack tip modeling in fracture mechanics is briefly discussed. Since a $\sqrt{r}$ displacement variation and a $1/\sqrt{r}$ singularity in the stress field exist near the crack tip based on the LEFM theory, it is impossible to represent these crack tip behaviors with the constant displacement discontinuity element. Therefore, the special crack tip element is adopted, for which the shape functions are modified to model the correct behavior of the displacements and stresses near the crack tip.

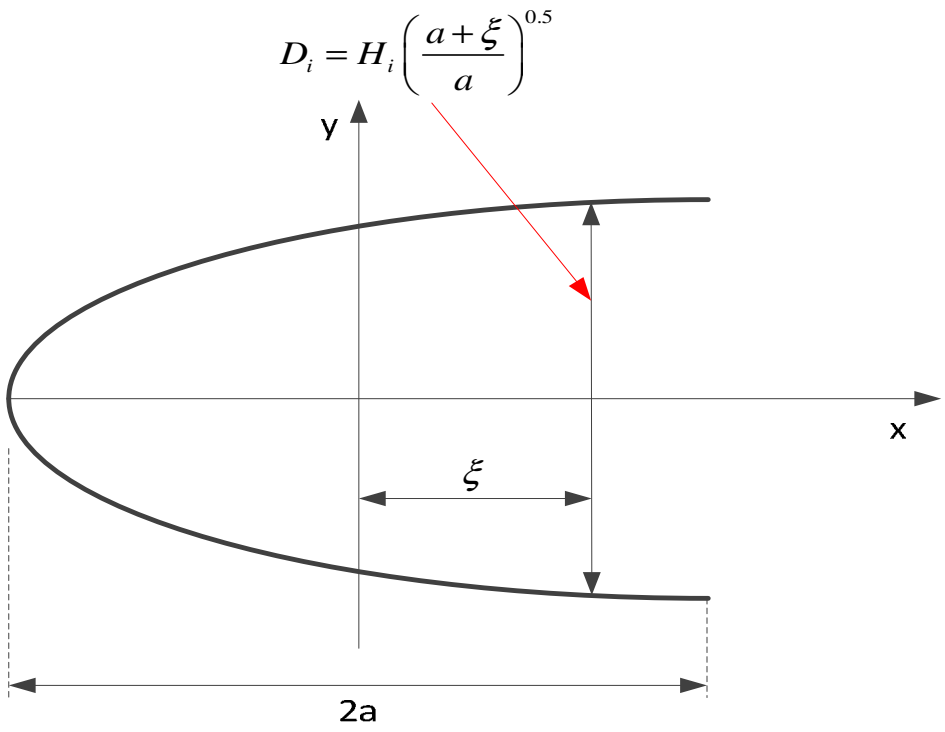

Figure 4.4 The special elastic DD element shape at the left crack tip (Yan 2004)

The schematic of the special crack tip displacement discontinuity element at the left tip of the crack is depicted in Figure 4.4.

The displacement discontinuity functions at the left tip are expressed in terms of constant displacement discontinuity (H_i) (Yan 2004):

$$D_x = H_s \left(\frac{a+\xi}{a} \right)^{0.5}$$
$$D_y = H_n \left(\frac{a+\xi}{a} \right)^{0.5} \quad \text{.....(4.10)}$$

where H_s and H_n are the tangential and normal displacement discontinuities at the center of the special crack tip element, respectively. The special crack tip element formulation and procedures for numerical integration are discussed in Appendix A in detail.

4.5 Crack extension criterion for numerical modeling

According to the linear elastic fracture mechanics (LEFM) approach, the cracked body can continuously propagate under loadings in rock if the following condition is satisfied. (We assume mode I only for discussion.)

$$K_{\mathrm{I}} \geq K_{\mathrm{Ic}} \quad \text{.....(4.11)}$$

where K_{I} is stress intensity factor, and K_{Ic} is fracture toughness of rock, an inherent material property that can be obtained by experimental work.

In reality, however, most of the geological rocks are subjected to some combination of mode I (tensile) and mode II (shear) loadings (a "mixed-mode" condition). Predicting the fracture trajectory under this circumstance is not simple; therefore, a number of crack extension criteria have been proposed by previous researchers (Erdogan and Sih 1963; Nuismer 1975; Stone and Babuska 1998).

With the assumption of quasi-static crack growth and neglecting dynamic effects (wave propagation), these criteria are:

1. Normal to the maximum principal (hoop) stress (Erdogan and Sih 1963)
2. Along the direction to the maximum energy release rate (Nuismer 1975)
3. Along the direction for which K_{II} vanishes on the crack extension (Stone and Babuska 1998)

In this section, we decided to use the maximum principal stress criterion because of its simplicity and accuracy in terms of numerical implementation (Stone and Babuska 1998). The maximum principal stress criterion explains that the crack will propagate

from the crack tip in the perpendicular direction where the hoop stress $\sigma_{\theta\theta}$ is at its maximum (Figure 4.5).

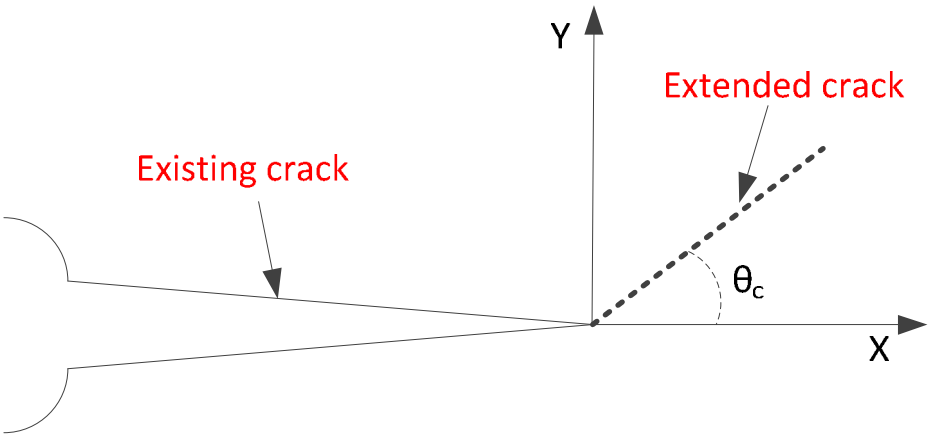

Figure 4.5 A discrete illustration of crack segment extension

Given the crack under mixed mode conditions, the asymptotic hoop and shear stresses near the tip in polar coordinates can be derived from Eqs. 4.2 and 4.3 by taking coordinate transformation. The following forms are given by

$$\begin{Bmatrix}\sigma_{\theta\theta}\\ \sigma_{r\theta}\end{Bmatrix}=\begin{Bmatrix}\frac{1}{\sqrt{2\pi r}}\cos\left(\frac{\theta}{2}\right)\left[K_{\mathrm{I}}\cos^2\left(\frac{\theta}{2}\right)-1.5K_{\mathrm{II}}\sin\theta\right]\\ \frac{1}{2\sqrt{2\pi r}}\cos\left(\frac{\theta}{2}\right)\left[K_{\mathrm{I}}\sin\theta+K_{\mathrm{II}}(3\cos\theta-1)\right]\end{Bmatrix} \quad \text{.....(4.12)}$$

At this point, the hoop stress in the direction of crack propagation is a principal stress. Therefore, the crack growth angle θ_c indicating the radial direction of

propagation can be determined by setting the shear stress $\sigma_{r\theta}$ to zero. Once the condition $\sigma_{r\theta} = 0$ is applied, the following equation is obtained:

$$\frac{1}{2\sqrt{2\pi r}}\cos\left(\frac{\theta}{2}\right)\left[K_{\mathrm{I}}\sin\theta + K_{\mathrm{II}}\left(3\cos\theta - 1\right)\right] = 0 \quad \text{.....(4.13)}$$

This leads to the equation determining the angle of crack extension θ_c in the local coordinate system.

$$K_{\mathrm{I}}\sin\theta_c + K_{\mathrm{II}}\left(3\cos\theta_c - 1\right) = 0 \quad \text{.....(4.14)}$$

Finally, solving this equation gives rise to

$$\theta_c = 2\arctan\frac{1}{4}\left(\frac{K_{\mathrm{I}}}{K_{\mathrm{II}}} - \mathrm{sgn}(K_{\mathrm{II}})\sqrt{\left(\frac{K_{\mathrm{I}}}{K_{\mathrm{II}}}\right)^2 + 8}\right) \quad \text{.....(4.15)}$$

Once the crack extention angle is determined, the maximum principal stress σ_1 is determined by

$$\sigma_1 = \frac{1}{\sqrt{2\pi r}}\cos^2\left(\frac{\theta_c}{2}\right)\left[K_{\mathrm{I}}\cos^2\left(\frac{\theta_c}{2}\right) - 1.5K_{\mathrm{II}}\sin\theta_c\right] \quad \text{.....(4.16)}$$

4.6 Numerical examples of fracture propagation in elastic rock

4.6.1 An inclined straight crack under uniaxial stress

Let us consider the inclined crack propagation problem shown in Figure 4.6. The initial length of the crack is 2 m, and it makes an angle β with the direction of applied uniaxial stress at infinity. For the numerical analysis, we took σ_y=1 Pa, E=10 kPa, ν =0.1, and 18 constant elastic displacement discontinuity (DD) and 2 elastic tip elements with equal size.

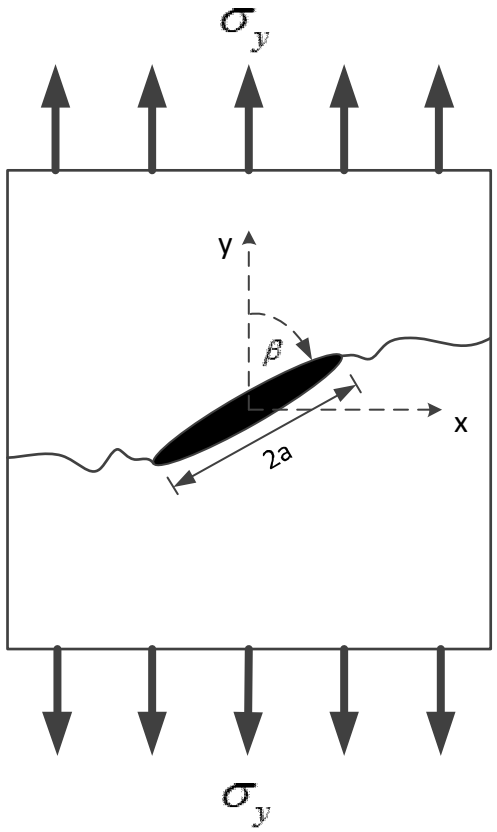

Figure 4.6 Typical fracture propagation from pre-existing crack under uniaxial stress

Figure 4.6 depicts a typical propagation path for an inclined crack that is not perpendicular to the applied normal stress. The initial angled crack is under a combination of mode I and II loadings (a mixed-mode condition). However, when the propagation occurs, this crack tends to propagate orthogonal to the applied stress (σ_y) as the mode II loading effect decays. This indicates that the mixed-modes crack becomes a pure Mode I crack propagation as it grows.

Figure 4.7 illustrates several propagation paths in terms of inclined angle (β). As mentioned above, the inclined crack turns and keep propagating perpendicular to the uniaxial loading, which is consistent with our prediction.

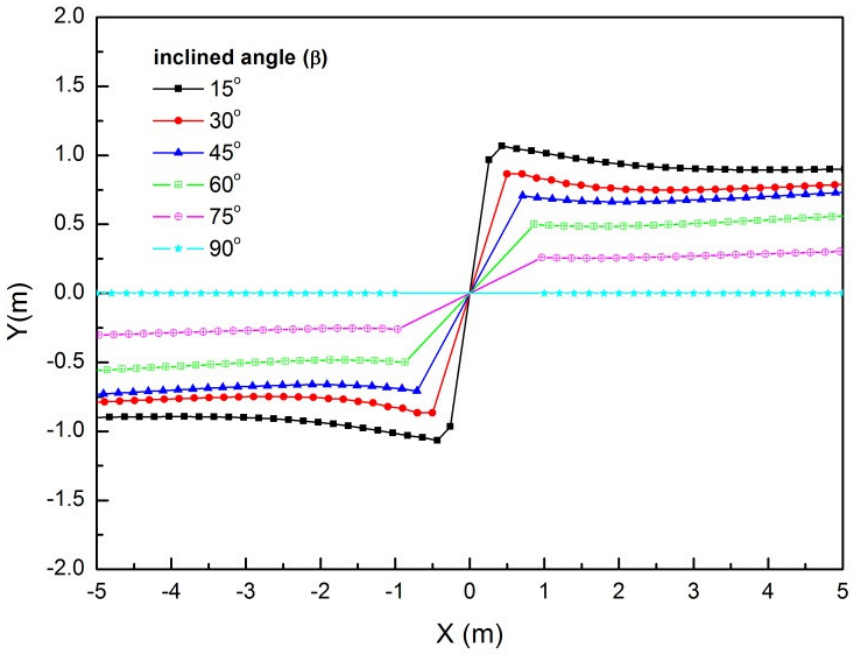

Figure 4.7 Fracture propagation trajectories of inclined crack under uniaxial tension

4.6.2 Vertical pressurized crack under biaxial compressive stresses

In this case, the initial crack with a length of 0.04 m is subjected to two principal confining stresses shown in Figure 4.8 based on the example in Dong's paper (Dong and de Pater 2001). The fluid is pumped into the crack and it assumes that there is no fluid loss throughout the crack propagation process. For the numerical analysis, we used E =20 GPa, ν =0.2, K_{Ic} =0.6 MPa√m, 9 constant elastic DD elements, and 1 elastic tip element with equal length for discretization. σ_H =19.4 MPa in the plane perpendicular to the initial crack and σ_h =9.7 MPa in the vertical direction.

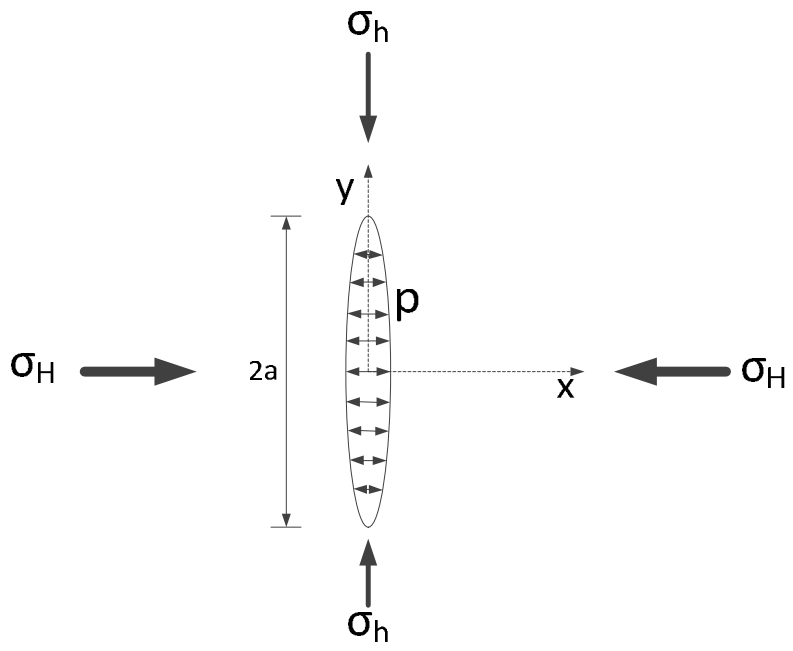

Figure 4.8 Pressurized crack under biaxial compressive stresses

Figure 4.9 illustrates the crack propagation paths for three different pressures (24.3, 29.1, and 38.8 MPa) inside the crack. A higher fluid pressure makes the crack path deviate gradually. Figure 4.10 shows the crack reorientation under three different maximum horizontal stresses (9.7, 19.4, and 22.6 MPa). In this case, the minimum vertical stress (σ_h) is 9.7 MPa and the pressure magnitude inside the crack is 29.1 MPa, and the crack reorients more rapidly under larger maximum horizontal stress.

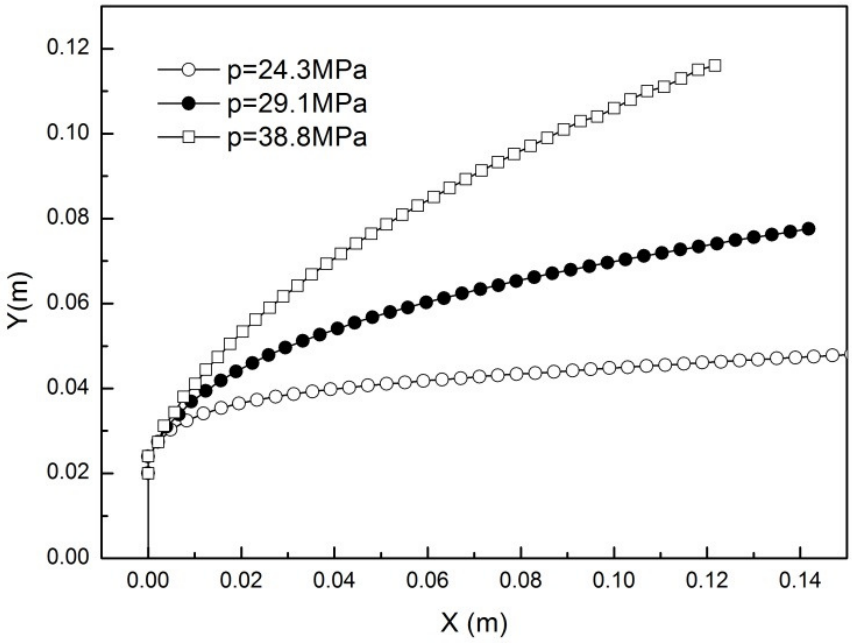

Figure 4.9 Crack reorienting paths for different internal pressures

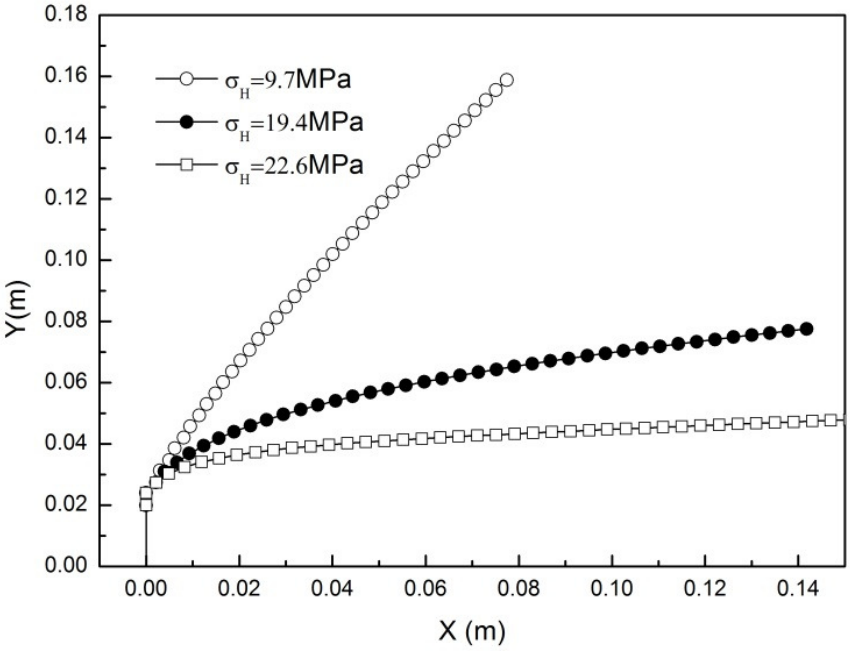

Figure 4.10 Crack reorienting paths for different maximum horizontal stresses

5. FRACTURE PROPAGATION IN POROELASTIC ROCK

5.1 Introduction

In recent years, hydraulic fracturing has become a major procedure in the petroleum industry for enhancing hydrocarbon production from low-permeability poroelastic rock formations (Huang and Russell 1985). Generally, the hydraulic fracturing process involves fully coupled deformation of the rock and fluid diffusion effects in the fluid-infiltrated porous rock.

However, most numerical methods for fracture propagation modeling in the petroleum industry have ignored the physical phenomena of fluid-solid coupling. Instead, these methods have assumed that the rock mass is an elastic medium and have neglected any influences related to the coupled effect such as changes in the rock deformation as the pore pressure diffuses or pressure changes induced by volumetric deformation of the rock. Even though their assumption can be effective in certain circumstances, in many situations, the coupled effect must be accounted for (Boone and Ingraffea 1990; Boone et al. 1991; Detournay and Cheng 1988; Detournay et al. 1989).

Meanwhile, as the application of this theory has become diverse, the study of the initiation and propagation of fractures in poroelastic media has been recognized as an area of both practical and fundamental interest (Selvadurai and Mahyari 1998).

The basic theory of poroelasticity was first developed by Biot (1941). Since then, Ruina (1978) has given analytical solutions for a semi-infinite crack propagating in poroelastic media, under various pore pressure boundary conditions on the crack faces,

and his solution is applicable to a hydraulic fracture propagating at a constant rate with impermeable crack surfaces. Huang and Russell (1985) extended Ruina's results to steadily propagating cracks where the fracture walls are permeable.

In poroelastic material with the nature of dissipative phenomena, a steadily propagating crack can be modeled at limiting times when the fracture propagation has occurred over a long period of time (Selvadurai and Mahyari 1998). Also to preserve the condition of steadily propagating crack, the tractions along the boundary should be time invariant in a reference to a coordinate system moving with the crack tip in an infinite poroelastic medium.

In this section, we present a numerical approach for implementing the steadily propagating crack in a poroelastic medium driven by tensile traction under two-dimensional plane strain conditions. First, we review Ruina's analytical approach to observe perception into the nature of the pore pressure field in the vicinity of hydraulic fractures. Second, we carried out fracture tip stress analysis to consider the stress and pore pressure distribution around the crack tip between drained and undrained conditions. In addition to this, we simulated two representative fracture propagation examples under poroelastic loading to investigate the influence of pore pressure on the crack extension path. Last, we developed a special poroelastic tip element and demonstrated the poroelastic tip effect on the near-tip stress and pore pressure field by comparing the case when the special elastic tip element is used at the crack tip.

5.2 Analytical approach for fractures propagating in poroelastic rock

As stated in Ruina's (1978) paper, two analytical solutions provide perception into the nature of the pore pressure fields in the vicinity of hydraulic fractures. One is the fully drained condition at low propagation velocities. The other is the undrained condition at high velocity limits. Figure 5.1 shows the geometry of the hydraulic fracture in Ruina's analytical model. The fracture is loaded by an applied stress P along the length a of the crack face, which is assumed to be impermeable.

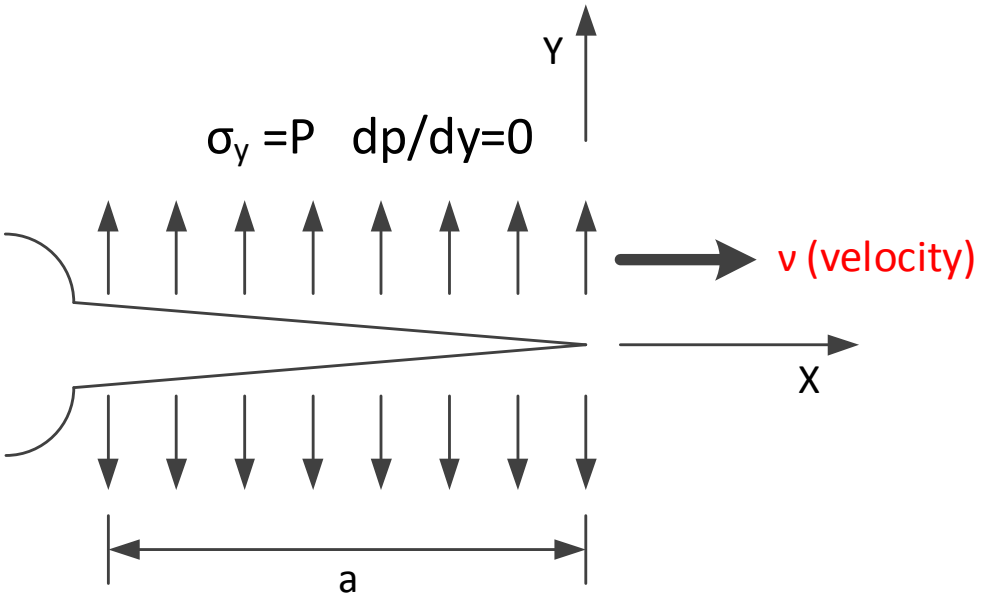

Figure 5.1 The dimensions and boundary conditions for Ruina's (Ruina 1978) model

In this case, the boundary conditions can be defined by the following assumptions and observations.

1) The impermeable assumption along the crack surface should be satisfied by the fact that there is no fluid flow across the crack faces.

$$\frac{\partial}{\partial y} p(x,0) = 0 \ (-\infty < x < \infty) \quad \text{..... (5.1)}$$

2) The symmetry of loading and consequent deformation with respect to the x-axis requires that no shear stress is applied along the entire x-axis.

$$\sigma_{xy}(x,0) = 0 \ (-\infty < x < \infty) \quad \text{..... (5.2)}$$

3) All field variables induced by the loading P should vanish at infinity from the crack tip.

$$p, \sigma_{xx}, \sigma_{yy}, \sigma_{xy} \to 0 \ \ as \ x^2 + y^2 \to \infty \quad \text{..... (5.3)}$$

4) Applied stress P is loaded along the length a of crack surface.

$$\sigma_{yy}(x,0) = -P(x) \ (-\infty < x < 0) \quad \text{..... (5.4)}$$

In addition, Ruina identified two different regimes of behavior for the fracture propagation in the poroelastic rock which are controlled by the characteristic length c_f / v, the ratio of the fluid diffusivity (c_f) to the crack propagation velocity (v).

In the fast regime ($c_f / v \cong 0$), the crack propagation speed is fast enough that there is no time for diffusion of pore fluid around the crack tip. This undrained field can cause pore pressure suction which is induced in the region of material breakdown near

the crack tip, thus resulting in reduced effective stress in that region. The solution for the full pore pressure field is given by

$$p(r,\theta) = -\frac{1}{\sqrt{2\pi r}} \frac{2B(1+\nu_u)}{3} \left(1 - e^{-\nu r(1+\cos\theta)/2c_f}\right) \cos\left(\frac{\theta}{2}\right) \quad \text{..... (5.5)}$$

where r is the radial distance from the crack tip , v is fluid velocity, θ is the angle measured at the crack tip from the x-axis c_f is fluid diffusivity, ν_u is undrained Poisson's ratio, and B is Skempton's pore pressure coefficient.

On the other hand, in the slow regime ($c_f / v \gg 0$), all excess pore pressure is totally drained in the general region of the crack face loading, the poroelastic response is exactly same as the elastic material, and the total induced pore pressure is zero everywhere. Also, the stress intensity factor is exactly the same as would be predicted for an elastic material. This can be explained because fracture propagation at very slow crack speed requires $K_{\mathrm{I}} = K_{\mathrm{Ic}}$ where K_{I} is defined as the stress intensity that the applied loads would cause on an elastic medium, and K_{Ic} is a fracture toughness of rock as inherent material properties. In conclusion, the characteristics of fracture propagation in a slow regime can be given by

$$\begin{aligned} &\sigma_{ij} = \sigma_{ij}^{\text{elastic}} \\ &K = K^{\text{elastic}} \\ &p = 0 \ (-\infty < x < \infty) \end{aligned} \quad \text{..... (5.6)}$$

5.3 Fracture tip stress analysis under undrained and drained loading

Poroelastic fracture propagation is of interest in many geomechanics problems where fracture initiation occurs over a period of time that is very short compared to the characteristic time of the rock. One approach to consider the poroelastic response is to consider a "short term analysis" (Bobet and Mutlu 2005). Such asymptotic analysis is useful, but a real transient analysis is required for a more comprehensive solution for various problems. Therefore, we improved the coupled poroelastic model with propagation to obtain the solution for very short times and compared it with the case under drained conditions.

In this section, we present stress analysis to consider the stress distribution around the crack tip and to show how the stresses change between drained and undrained conditions. Let us assume that a single inclined crack (45° with the horizontal) of length of 2 m lies in a poroelasic rock shown in Figure 5.2. The Young's modulus of the rock is E=5.96 GPa, and its Poisson's ratio is ν=0.15. Then we impose uniaxial compressive stress (1 MPa) along the vertical direction. The initial condition is of zero pore pressure everywhere and zero tractions along the crack boundary. For simplicity, we assumed that the crack was only propagating from one end. For the dicretization of the crack boundary, we imposed 20 constant displacement discontinuity (DD) elements with one special elastic tip element at the right side of the crack. All material parameters of this analysis are shown in Table 5.1.

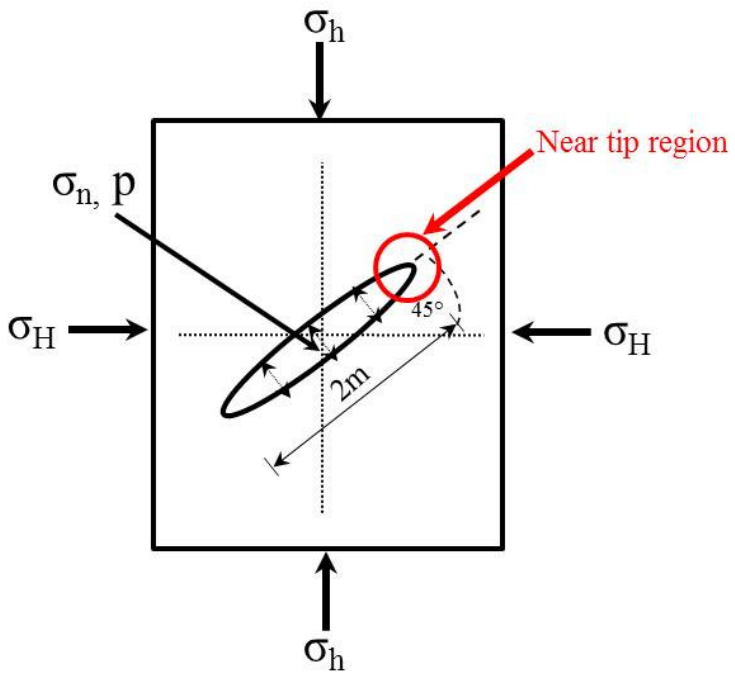

Figure 5.2 Schematic illustration of crack geometry in a poroelastic medium

Table 5.1 Material properties used in crack tip stress analysis

Young's Modulus, E (GPa)	5.96
Poisson's ratio, ν	0.15
Undrained Poisson's ratio, ν_u	0.33
Solid bulk Modulus, K_s (GPa)	45
Fluid bulk Modulus, K_f (GPa)	2.5
Skempton's coefficient, B	0.85
Fluid diffusivity, c_f (m^2/s)	6.16×10^{-5}
Fluid viscosity, μ_f (Pa·s)	3.547×10^{-4}
Rock permeability, κ (m^2)	4.0×10^{-19}
Water density, ρ_w (kg/m^3)	1000
Biot's coefficient, α	0.444
Porosity, ϕ	0.01

Figure 5.3 and Figure 5.4 show contours of radial and tangential stresses (tension positive sign convention) in an area close to the crack tip (0.7071, 0.7071), respectively. For convenience, the stresses are expressed in polar coordinates with origin at the tip of the crack to precisely analyze the numerical results. For the radial and tangential stresses in both cases, the maximum in compression and tension occur at exactly the same distance from the crack tip but in opposite directions. Also the radial stresses are of the same magnitude as the tangential stresses but opposite in sign in both cases. In addition, for the undrained condition, the magnitudes of tangential compression tend to decrease.

On the other hand, the tensile stress tends to increase, particularly ahead of the crack tip where the tensile stresses are the largest. This phenomenon indicates that loading in undrained compression is a much more effective process for the crack initiation (Bobet 2000, 2001).

Figure 5.5 illustrates the shear stress distribution in both cases; it is independent of the drained or undrained condition, which shows nearly zero. Figure 5.6 is a plot of total induced pore pressure in both cases. The pore pressure is nearly zero for the drained condition because enough time has elapsed to diffuse the pore pressure into the formation. In conclusion, these numerical results are consistent with the asymptotic model shown in Bobet and Mutlu's (Bobet and Mutlu 2005) work.

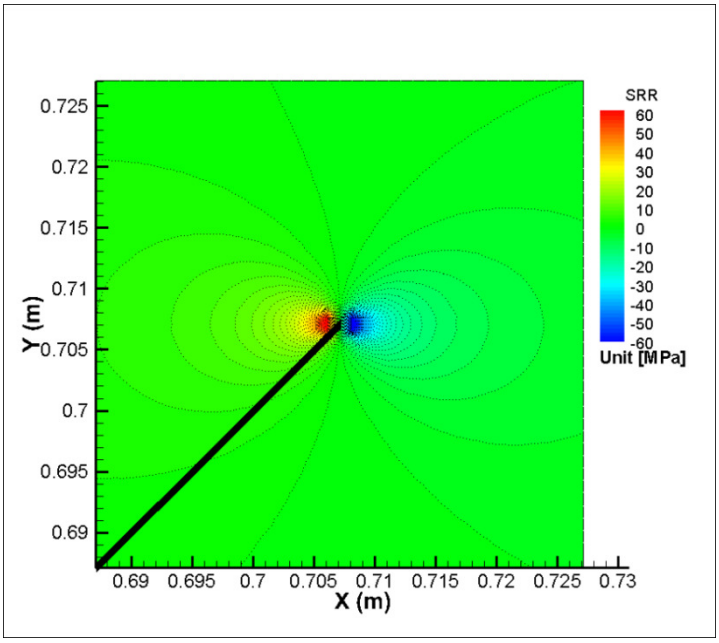

(a) Drained- σ_{rr}

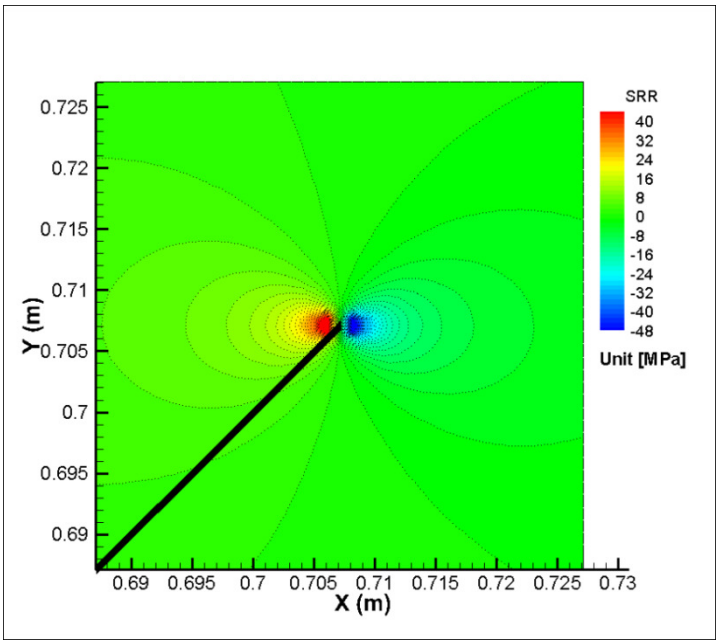

(b) Undrained- σ_{rr}

Figure 5.3 Radial stress (MPa) at the tip of the inclined crack in (a) drained and (b) undrained conditions

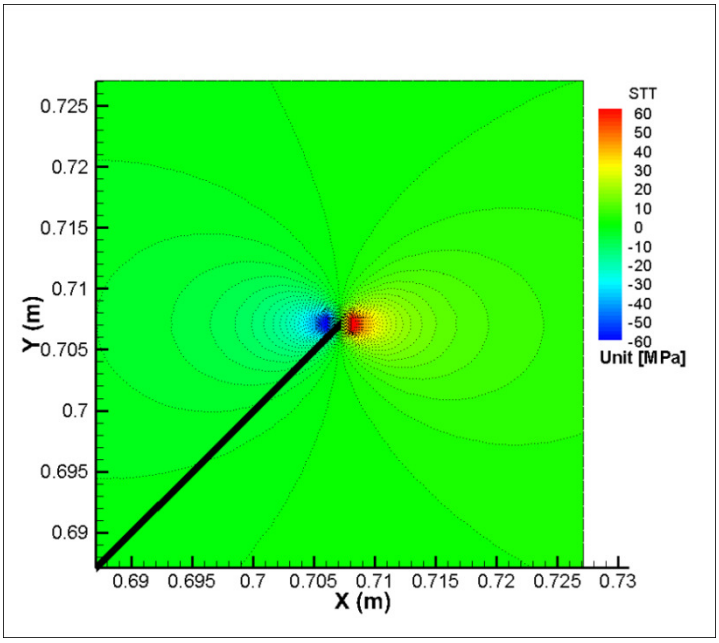

(a) Drained- $\sigma_{\theta\theta}$

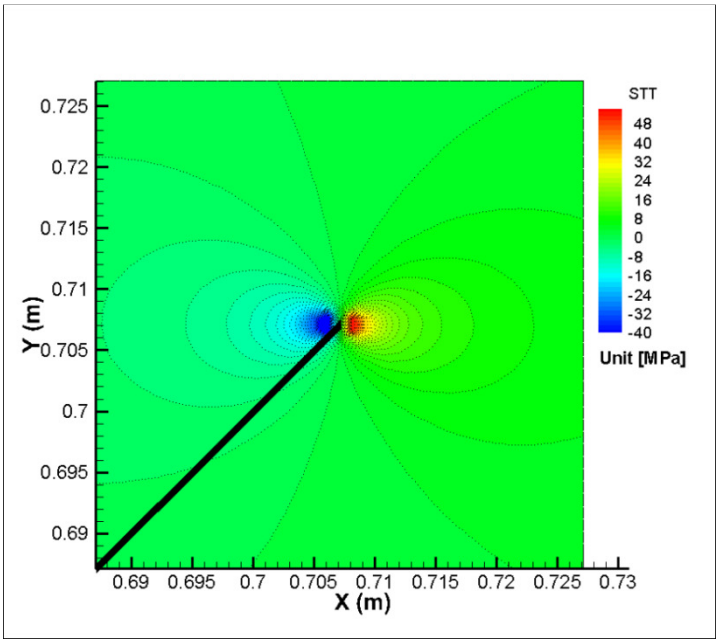

(b) Undrained- $\sigma_{\theta\theta}$

Figure 5.4 Tangential stress (MPa) at the tip of the inclined crack in (a) drained and (b) undrained conditions

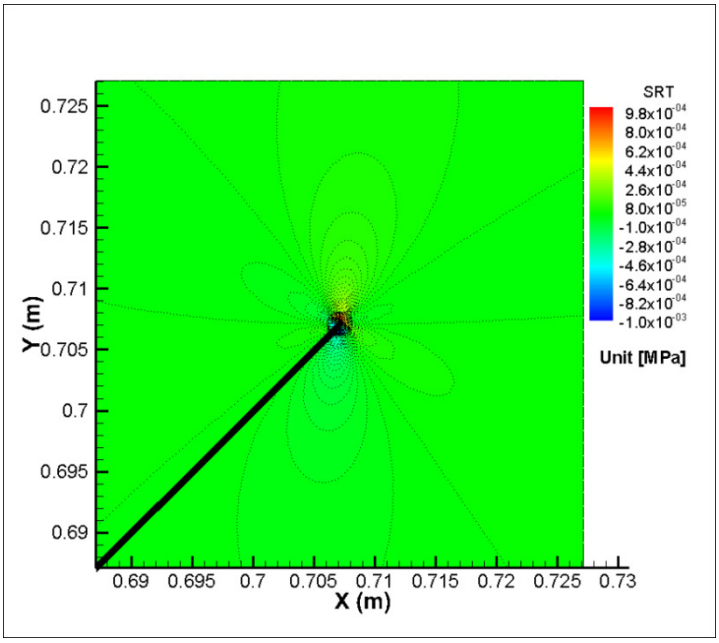

(a) Drained- $\sigma_{r\theta}$

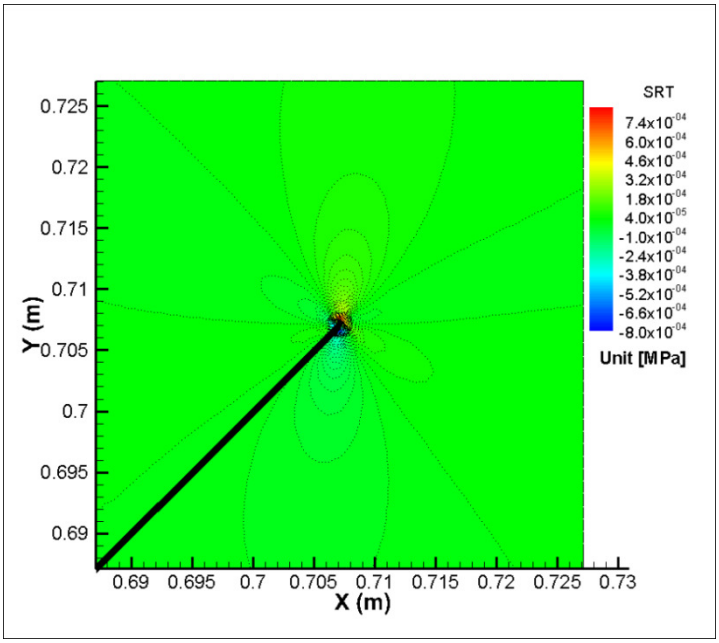

(b) Undrained- $\sigma_{r\theta}$

Figure 5.5 Shear stress (MPa) at the tip of the inclined crack in (a) drained and (b) undrained conditions

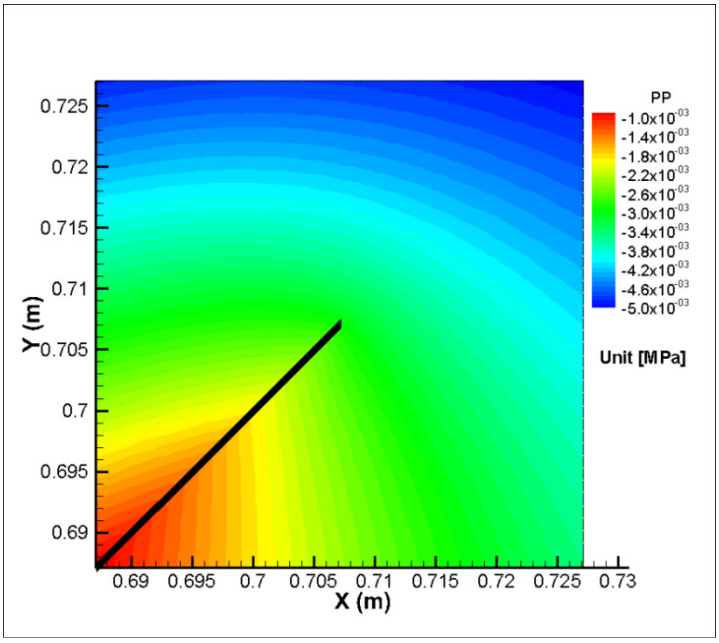

(a) Drained- pressure

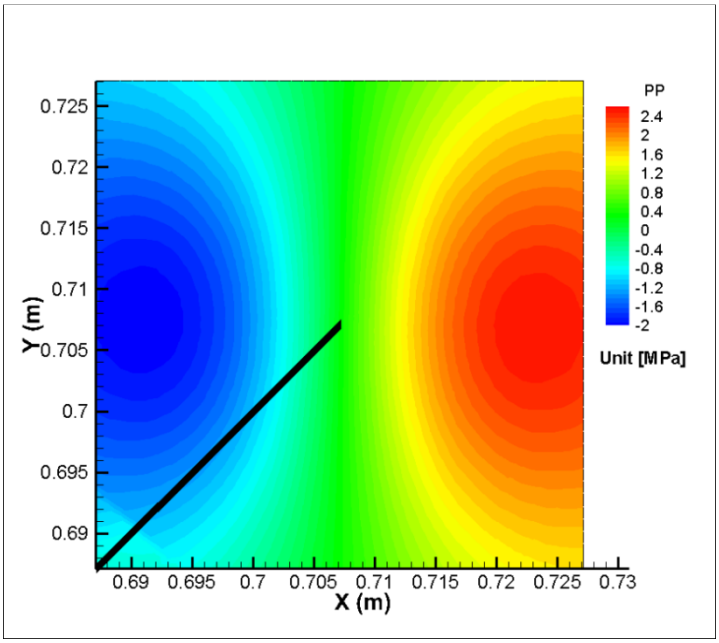

(b) Undrained- pressure

Figure 5.6 Pore pressure (MPa) at the tip of the inclined crack in (a) drained and (b) undrained conditions

5.4 Numerical examples of fracture propagation in poroelastic rock

Compared with the general elastic fracture propagation procedure which is time independent, fracture propagation under poroelastic loading can be affected by coupling of deformation and diffusion, making the process more complicated.

In this section, we consider two limiting cases of propagation to illustrate the impact of various drainage stages on the propagation pressure and path of the crack. We consider the case of very fast crack growth and that of slow crack growth. To model numerical propagation in these regimes, we use very high (6.16×10^{-2} m^2/s), and very slow (6.16×10^{-8} m^2/s) diffusivities instead of considering crack propagation velocity (v).

As mentioned in section 5.2, in the fast regime, the pore pressure diffusion effect on the crack growth is so small that the rock can be regarded as an elastic medium. But in the slow regime, the pore pressure considerably affects the fracture propagation because the crack growth occurs at very low speed. To illustrate the impact of pore pressure loading during the propagation process, we carried out a crack path comparison between Mode I and Mode I+II loading to capture the effects of pore pressure on the crack path.

Figure 5.7 illustrates the inclined pressurized crack under boundary stress and pressure loading. The crack length is 2 m, and it lies along a 45° angle from the x-axis. Initially there is zero pore pressure and only maximum and minimum in-situ stresses are acting around the crack. A total of 50 constant poroelastic elements including 1 tip element (right tip) were used to discretize the crack boundary. The material parameters used in this simulation are shown in Table 5.2.

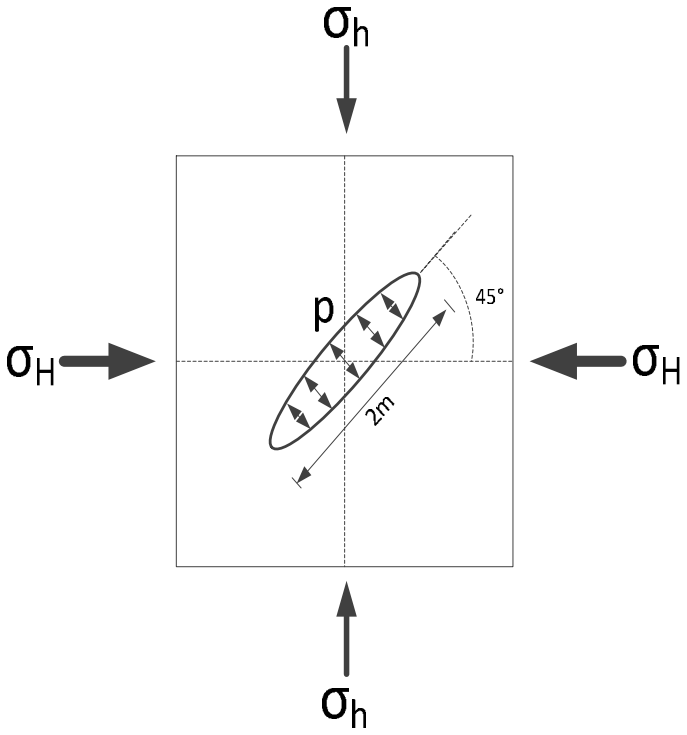

Figure 5.7 Inclined pressurized crack in an infinite poroelastic medium

Table 5.2 Poroelastic constants used in this simulation

Young's Modulus, E (GPa)	37.5
Poisson's ratio, ν	0.25
Undrained Poisson's ratio, ν_u	0.33
Solid bulk Modulus, K_s (GPa)	45
Fluid bulk Modulus, K_f (GPa)	2.5
Skempton's coefficient, B	0.85
Fluid diffusivity, c_f (m^2/s)	6.16×10^{-5}
Fluid viscosity, μ_f (Pa·s)	3.547×10^{-4}
Rock permeability, κ (m^2)	4.0×10^{-19}
Water density, ρ_w (kg/m^3)	1000
Biot's coefficient, α	0.444
Porosity, ϕ	0.01

5.4.1 Very fast crack growth regime (undrained loading)

In this case, let us consider the fracture propagation under undrained conditions (very fast crack growth). To reasonably represent undrained conditions instead of the crack propagation velocity (v), we considered very low fluid diffusivity (6.16×10^{-8} m^2/s). Figure 5.8 shows the fracture propagation paths under two different loading conditions. As shown, if the crack growth under the combined Mode I and II loading is very fast, the fracture propagates in nearly the same direction as under Mode I loading alone. This phenomenon is explained by that the fracture growth speed is so fast that the pore pressure diffusion effect is negligible consequently it does not affect the direction of crack growth.

5.4.2 Very slow crack growth regime (drained loading)

In this case, we considered fracture propagation under drained conditions (very slow crack growth). To represent drained conditions, we used very high fluid diffusivity (6.16×10^{-2} m^2/s). As shown in Figure 5.9, under very slow crack growth with both Mode I and II loading, the fracture propagates in different directions than under only Mode I loading. This is because the pore pressure diffusion under very slow crack growth not only produces a small amount of crack closing but increases shear stress around the crack tip. Consequently, the change of the principal stress direction induced by the increase of shear stress makes the crack grow in different directions.

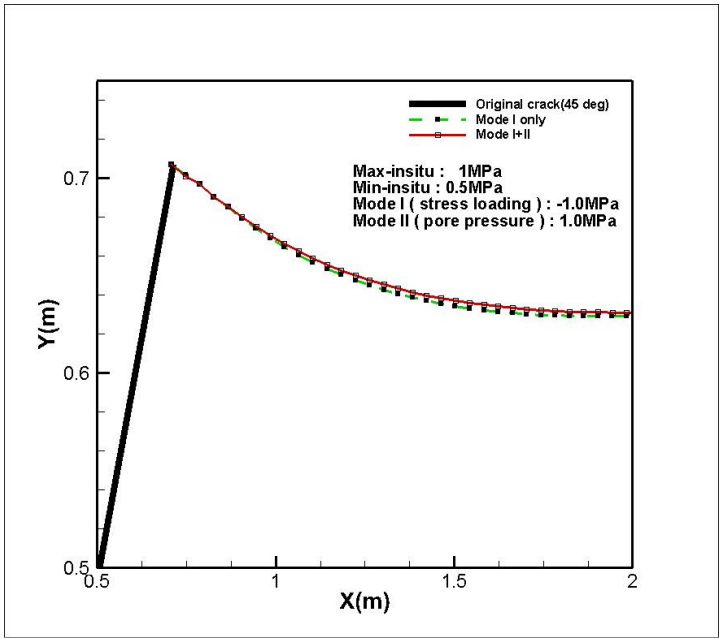

(a) Boundary loading (case 1): $\sigma_H = -1.0\,\text{MPa}$, $\sigma_h = -0.5\,\text{MPa}$, $\sigma_n = p = -1.0\,\text{MPa}$

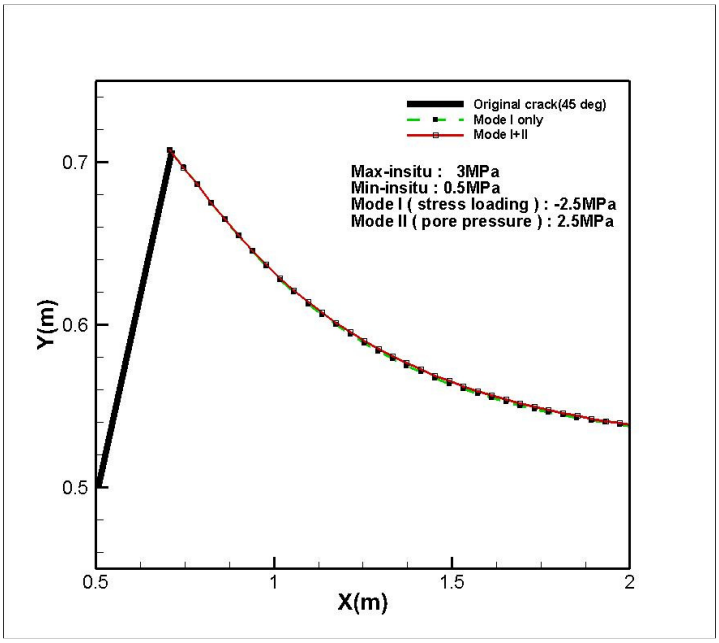

(b) Boundary loading (case 2): $\sigma_H = -3\,\text{MPa}$, $\sigma_h = -0.5\,\text{MPa}$, $\sigma_n = p = -2.5\,\text{MPa}$

Figure 5.8 Crack path comparison between Mode I and Mode I+II loading under undrained conditions with two different boundary loadings

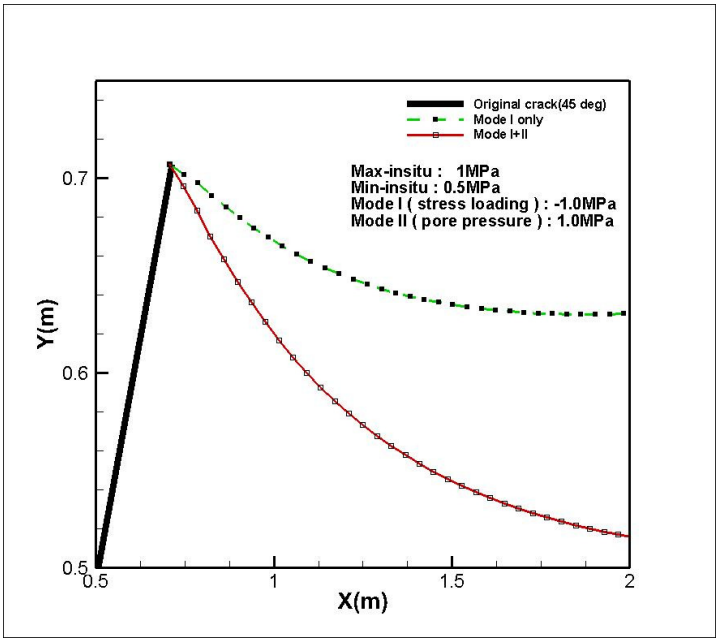

(a) Boundary loading (case 1): $\sigma_H = -1.0\,\text{MPa}$, $\sigma_h = -0.5\,\text{MPa}$, $\sigma_n = p = -1.0\,\text{MPa}$

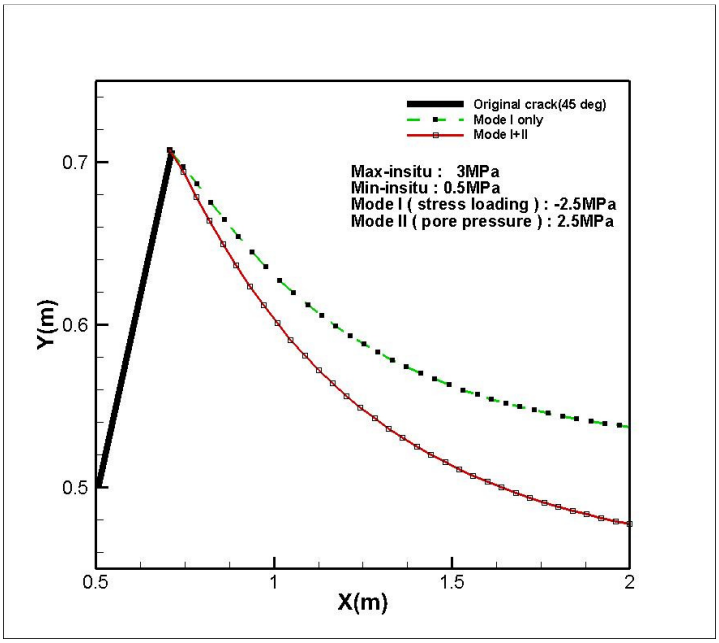

(b) Boundary loading (case 2): $\sigma_H = -3\,\text{MPa}$, $\sigma_h = -0.5\,\text{MPa}$, $\sigma_n = p = -2.5\,\text{MPa}$

Figure 5.9 Crack path comparison between Mode I and Mode I+II loading under drained conditions with two different boundary loadings

5.5 Poroelastic crack tip element implementation

Fracture propagation and its orientation in fluid-saturated media are mainly controlled by the pore pressure field. Generally for fracture problems involving a pore pressure, the influence of the pore pressure must be investigated. In particular, near the crack tip region, the stress and pore pressure fields vary with time because they are functions of the diffusivity of the medium. Therefore, investigation of those variables with diverse time and space domains is very important to anticipate the fracture propagation behavior.

Nevertheless, most numerical fracture propagation modeling in the boundary element method has ignored the pore fluid influence at the crack tip, and just considered the elastic displacement discontinuity sources.

Therefore, in this section, we develop the poroelastic crack tip element by extending the elastic displacement discontinuity crack tip element formulation (Yan 2004). Carvalho (1990) developed fully coupled displacement discontinuity methods and presented the fundamental singular solutions in a poroelastic infinite medium. To be specific, they provided the induced stress, displacement, and pore pressure attributable to the sources of constant fluid and displacement discontinuities in boundary elements. Based on these solutions, we expanded those formulations and implemented boundary integral equations for numerical applications.

A simple pressurized crack problem is our target to investigate stress and pore pressure distributions near the tip region. To examine this challenging issue, we considered three representative cases.

1. Purely elastic rock without a tip element

2. Poroelastic rock with an elastic tip element

3. Poroelastic rock with a poroelastic tip element

Also, for the poroelastic case we included two limiting behaviors (undrained and drained conditions) to capture its time-dependent poroelastic nature. The special elastic and poroelastic tip element formulations are shown in Appendices A and B, respectively. For the crack geometry, as shown in Figure 5.10, initially, the crack length was 2 m and there were zero pore pressure and in-situ stresses around the crack.

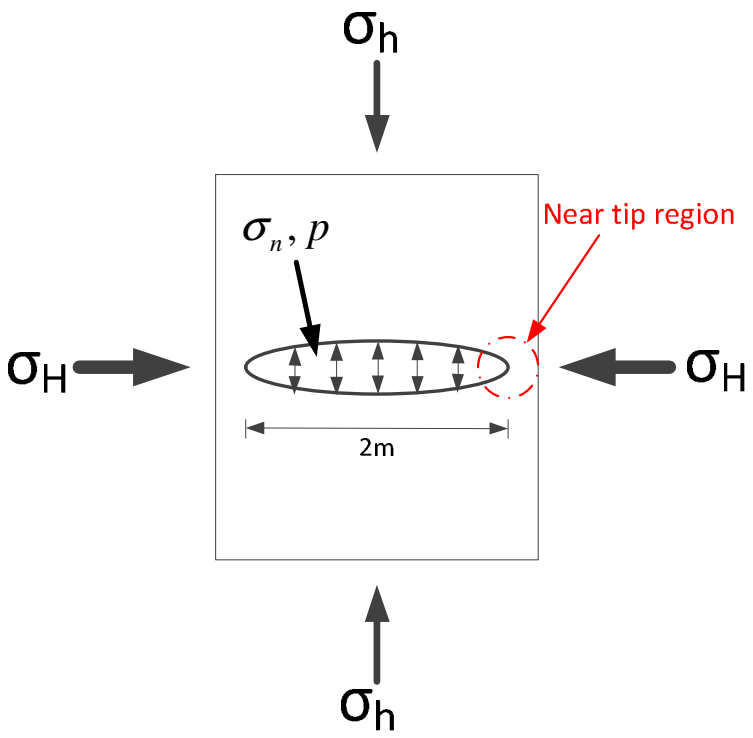

Figure 5.10 Pressurized crack geometry and crack tip region

We applied only the normal stress (1 MPa) loading across the crack surfaces uniformly. A total of 50 constant elastic or poroelastic elements including 1 crack tip (right tip) were used; the material parameters related to this simulation are shown in Table 5.2. In this case, we assumed that 10 seconds can represent undrained behavior and 10^8 seconds was chosen to represent drained behavior.

As mentioned in introduction, the general poroelastic response under drained conditions is exactly same as the elastic material because the total induced pore pressure is zero, which indicates there is no influence of the pore pressure effect around the fracture. Therefore, the stress distribution around the crack tip should be the same for all three cases. The distributions of vertical and horizontal stress near the crack tip under drained loading for the three cases are plotted in Figure 5.11 and 5.12, respectively. Note that the numerical results show a good agreement with the analytical explanation of drained behavior. Figure 5.13 shows the total induced pore pressure distribution near the crack tip under drained loading. It indicates that there is no influence of the pore fluid around the tip region because the pore fluid already has dissipated into the rock formation characterizing the drainage stage.

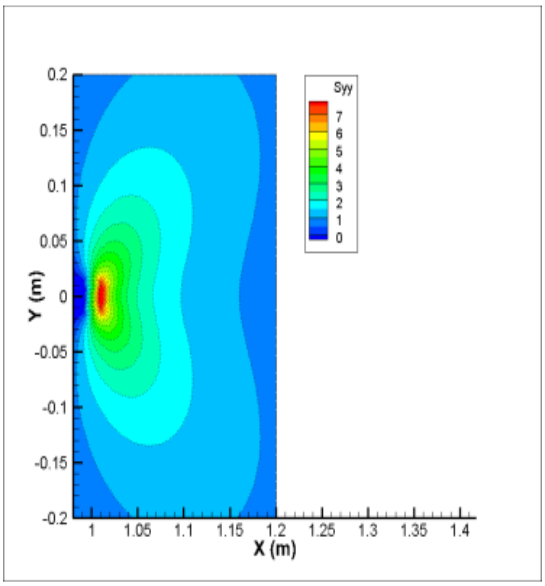

(a) Purely elastic

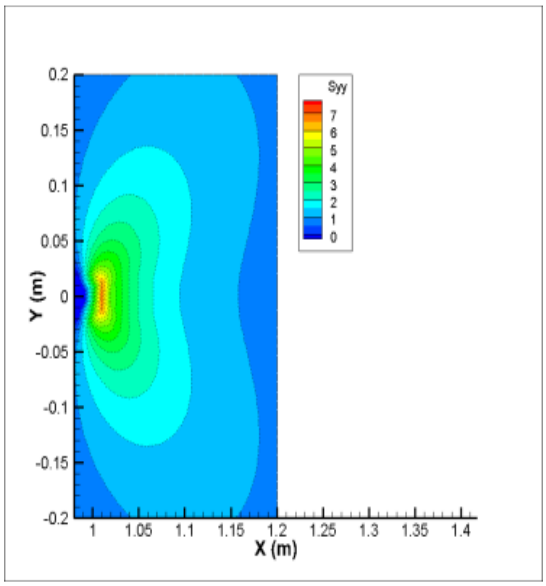

(b) elastic tip

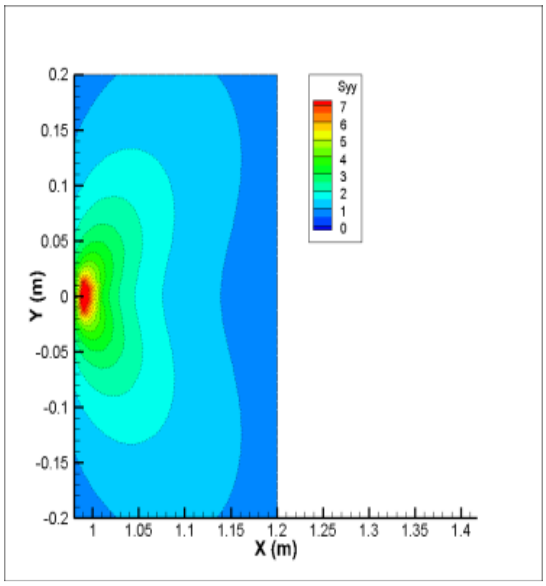

(c) poroelastic tip

Figure 5.11 Stress distribution (MPa) along the y axis around crack tip: (a) purely elastic, (b) elastic tip, and (c) poroelastic tip under drained conditions

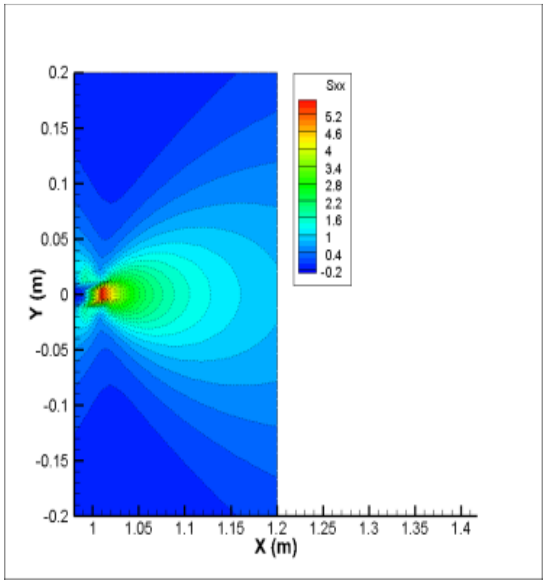

(a) Purely elastic

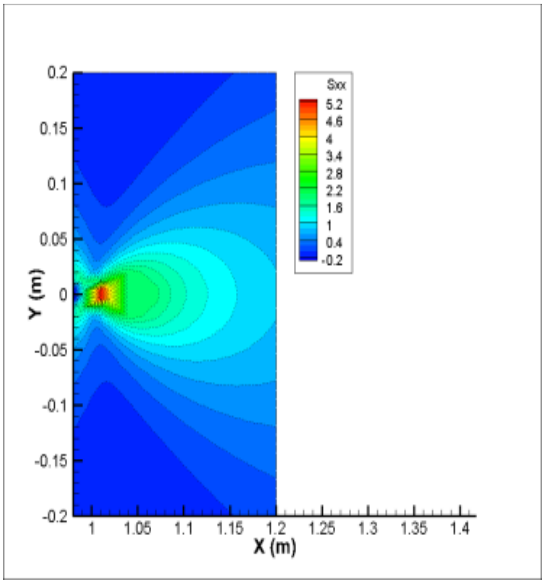

(b) elastic tip

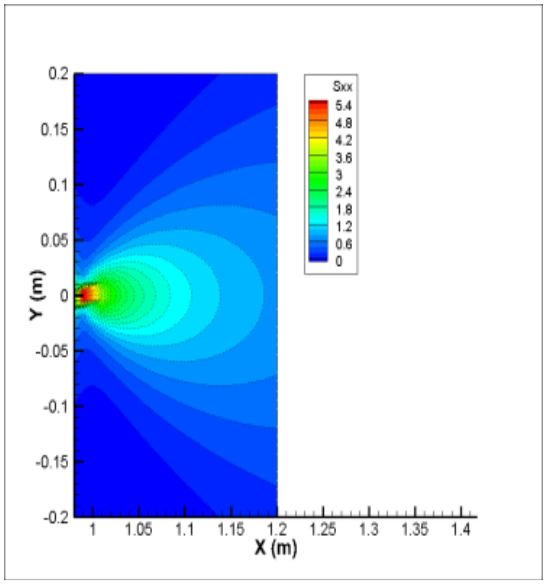

(c) poroelastic tip

Figure 5.12 Stress distribution (MPa) along the x axis around crack tip: (a) purely elastic, (b) elastic tip, and (c) poroelastic tip under drained conditions

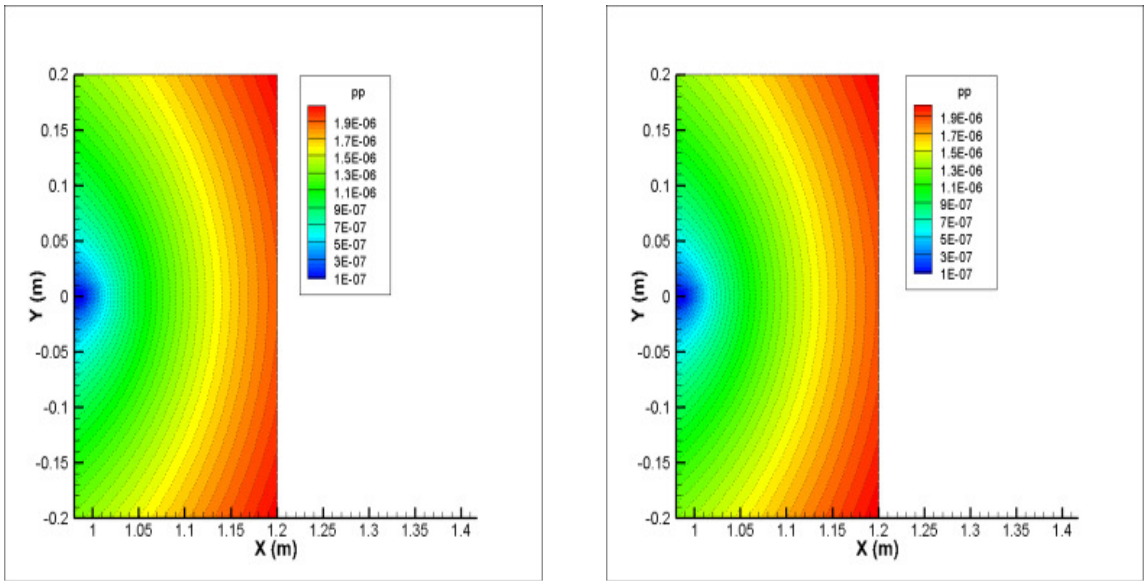

(a) elastic tip (b) poroelastic tip

Figure 5.13 Pore pressure distribution (MPa) around crack tip: (a) elastic tip (b) poroelastic tip under drained conditions

The distributions of vertical and horizontal stresses near the crack tip under undrained loading for the three cases are plotted in Figures 5.14 and 5.15.

Figure 5.16 shows the total induced pore pressure distribution near the crack tip under undrained loading. It indicates that this undrained field can induce pore pressure suction in the region of material breakdown near the crack tip, which reduces the stress field in that region.

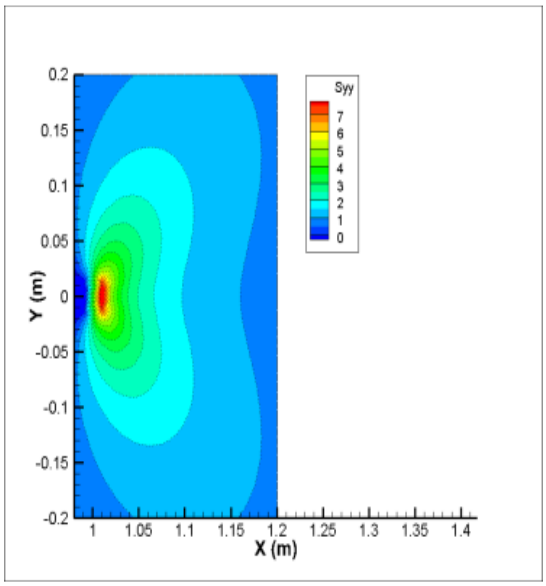

(a) Purely elastic

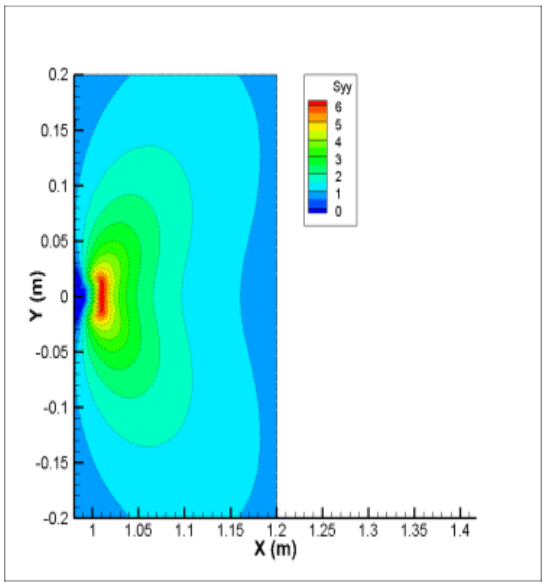

(b) elastic tip

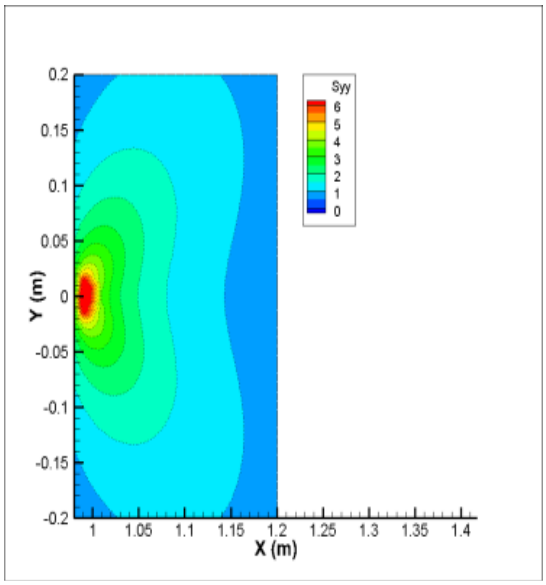

(c) poroelastic tip

Figure 5.14 Stress distribution (MPa) along the y axis around the crack tip: (a) purely elastic, (b) elastic tip, and (c) poroelastic tip under undrained conditions

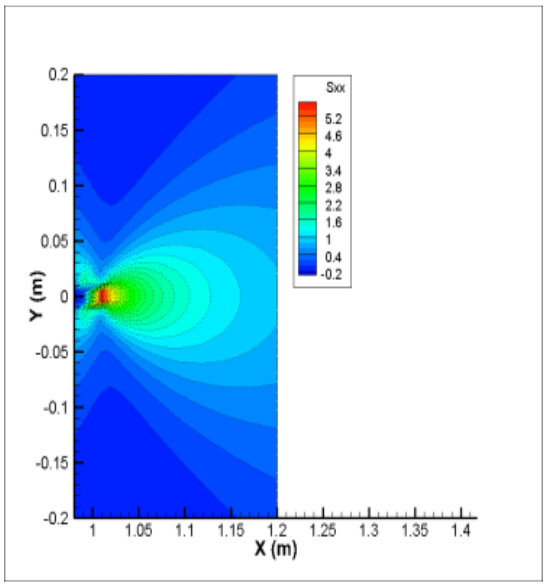

(a) Purely elastic

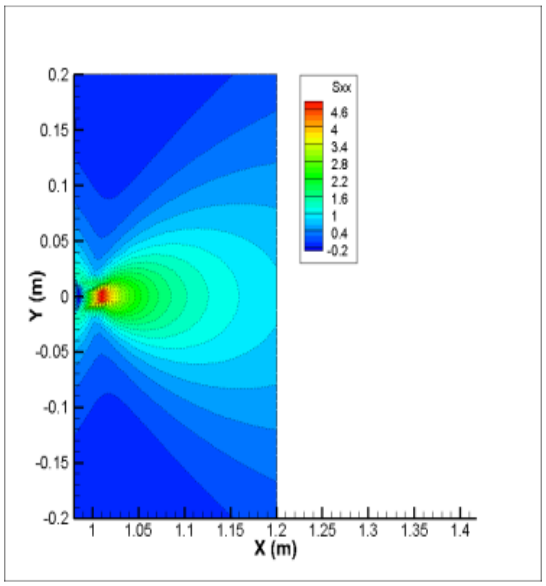

(b) elastic tip

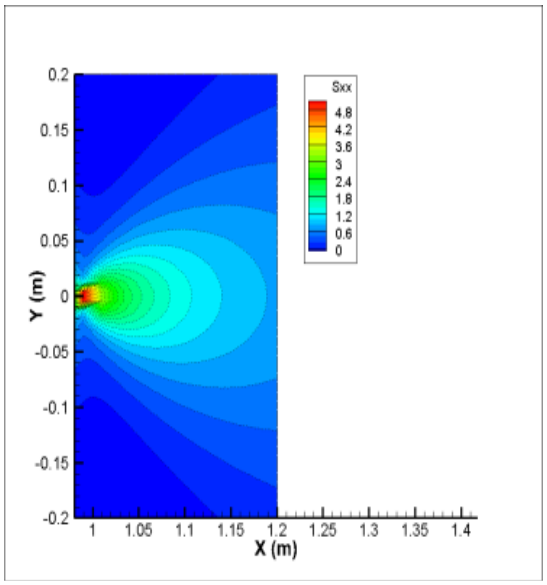

(c) poroelastic tip

Figure 5.15 Stress distribution (MPa) along the x axis around the crack tip: (a) purely elastic, (b) elastic tip, and (c) poroelastic tip under undrained conditions

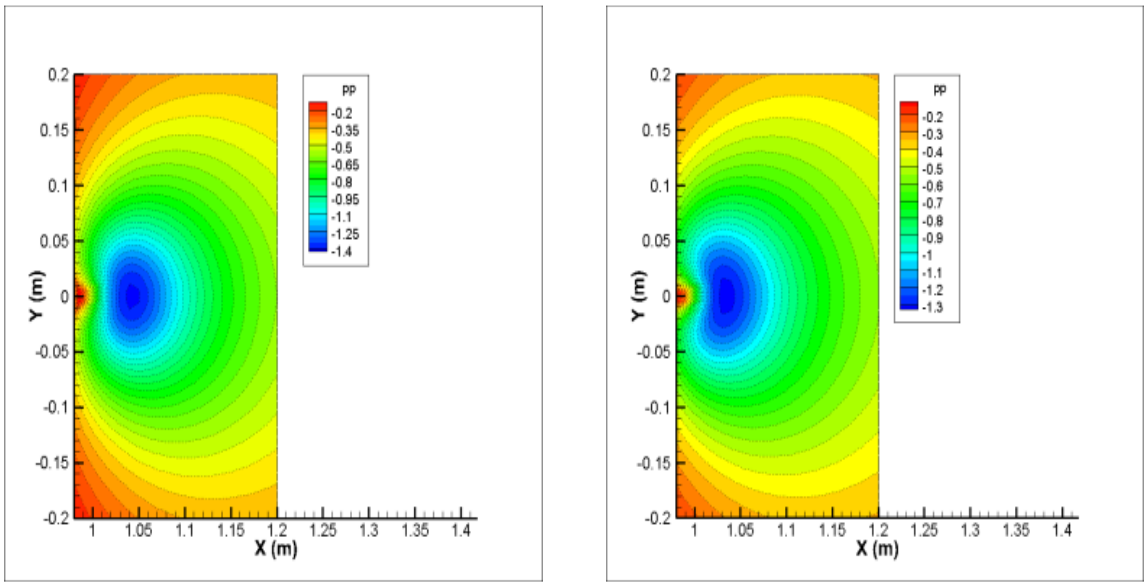

(a) elastic tip (b) poroelastic tip

Figure 5.16 Pore pressure distribution (MPa) around the crack tip: (a) elastic tip (b) poroelastic tip under undrained conditions

6. FRACTURE PROPAGATION IN THERMOELASTIC ROCK

6.1 Introduction

When the rock around a wellbore and a main fracture is cooled by injecting cold water into a hot reservoir, the rapid decrease in temperature gives rise to thermal (tensile) stress which causes cracks to initiate and influences their propagation into the rock matrix. As the rock is cooled, the in-situ stress components near the cooled zone tend to decrease and, depending on the geometry of the cooled zone, the orientations of the principal stresses can be reversed. Thermal stresses induced by cooling may exceed the in-situ stress in the reservoir, creating secondary fractures perpendicular to the main fracture (Perkins and Gonzalez 1985).

On the other hand, thermal loading not only changes the total stress but also alters the pore fluid pressure, causing additional variations in the total and effective stress states. In conventional hydraulic fracturing, this thermal coupling effect evolves because of the small thermal diffusivity of rocks; thus, thermal effects may not have a large influence on fracture propagation. However, if the injection period is long (time scale of weeks/months), the thermo-poro-mechanical coupling is not negligible (Ghassemi and Zhang 2006).

In this section, the propagation of multiple fractures by transient cooling from water injection is numerically studied. Propagation and interaction among the main and secondary fractures in both thermoelastic and poro-thermoelastic rock are considered.

6.2 Thermoelastic stresses in cooled region

If the injected fluid is at a temperature different from the formation temperature in a geothermal reservoir, a region of changed rock temperature will progress outward from the injection well (Perkins and Gonzalez 1985). The outer boundary of the region of changed temperature will be elliptical in its plane view and confocal with the two-winged vertical fractures shown in Figure 6.1.

Stresses within the region of altered temperature will be changed because of the expansion or contraction of the rock within the region of altered temperature. The interior thermoelastic stresses parallel and perpendicular to the major axes of the ellipse are given by:

$$\Delta\sigma_H = -\frac{1}{1+(b_0/a_0)} \cdot \frac{E\beta_s\Delta T}{3(1-\nu)} \quad \text{..... (6.1)}$$

$$\Delta\sigma_h = -\frac{(b_0/a_0)}{1+(b_0/a_0)} \cdot \frac{E\beta_s\Delta T}{3(1-\nu)} \quad \text{..... (6.2)}$$

where a_0 is major semi-axis of the elliptical cooled region, b_0 is minor semi-axis of the elliptical cooled region, E is Young's modulus, β_s is rock volumetric thermal expansion coefficient, ν is Poisson's ratio, ΔT is temperature difference between reservoir rock and injected water.

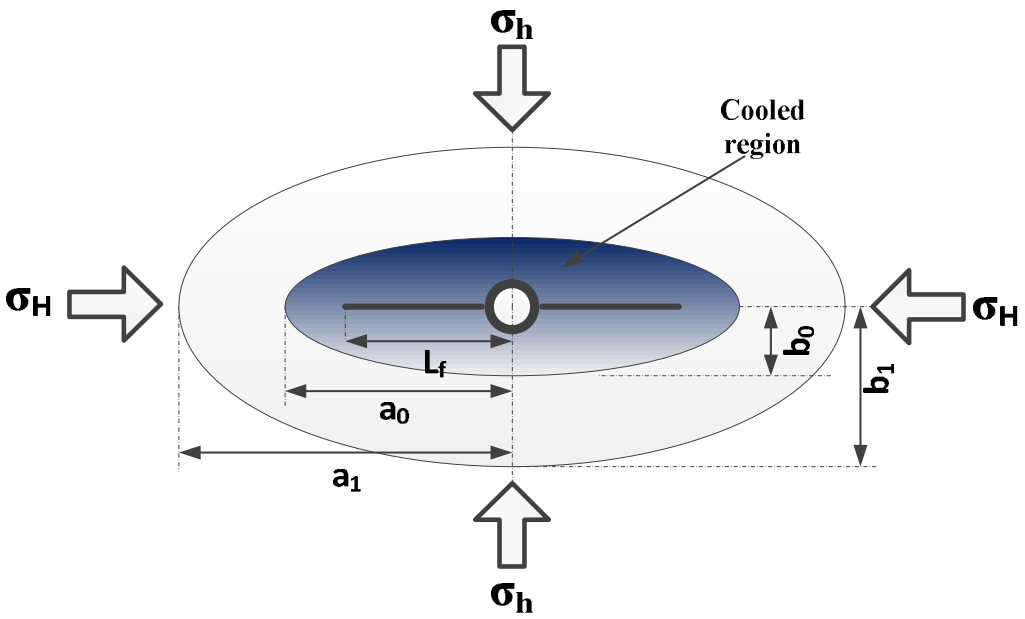

Figure 6.1 Plane view of cooled zone around a two-wing fracture and wellbore

6.3 Temperature and thermal stress calculation

The approach of transient cooling of the main and secondary fractures can be solved using the DD boundary integral equation method. It is assumed that rock has low permeability and the fluid leak off effect on thermal transport is negligible. The newly created secondary fractures have very small length compared with the main fracture and are filled with the pore fluid of same temperature as the uniformly cooled main fracture.

In the thermoelastic rock, the temperature and the corresponding stresses caused by a unit continuous point heat source are given by (Nowacki 1962).

For temperature:

$$T^{ch} = \frac{1}{4\pi\kappa^T} Ei(\xi^2) \quad \text{..... (6.3)}$$

For thermal stress:

$$\sigma_{ij}^{ch} = \frac{G\beta_s(1+\nu)}{12\pi\kappa^T(1-\nu)}\left\{\left(\delta_{ij} - \frac{2x_i x_j}{r^2}\right)\frac{1}{\xi^2}(1-e^{-\xi^2}) - \delta_{ij}Ei(\xi^2)\right\} \quad \text{..... (6.4)}$$

where, $\mathrm{Ei(x)} = \int_{-\infty}^{x} \frac{e^t}{t}dt$, $\xi^2 = \frac{r^2}{4c^T t}$, $r^2 = x^2 + y^2$, c^T is thermal diffusivity, κ^T is thermal conductivity, G is shear modulus, β_s is rock volumetric thermal expansion coefficient, ν is Poisson's ratio, $\mathrm{Ei(x)}$ is exponential integral function, and t is time. Then integrating the above point source solution over the straight line element with length 2a yields the stresses due to a constant displacement discontinuity source (Ghassemi and Zhang 2006).

For temperature:

$$T = \frac{1}{4\pi\kappa^T}\int_{-a}^{a} Ei(\xi^2)dx' \quad \text{..... (6.5)}$$

For thermal stress:

$$\sigma_{xx} = \frac{G\beta_s(1+\nu)}{12\pi\kappa^T(1-\nu)}\left\{\left[-(x-x')\frac{1-e^{-\xi^2}}{\xi^2} - (x-x')Ei(\xi^2)\right]_{-a}^{a} - 2\int_{-a}^{a} Ei(\xi^2)dx'\right\} \quad \text{..... (6.6)}$$

$$\sigma_{yy} = \frac{G\beta_s(1+\nu)}{12\pi\kappa^T(1-\nu)}\left[(x-x')\frac{1-e^{-\xi^2}}{\xi^2} + (x-x')Ei(\xi^2)\right]_{-a}^{a} \quad \text{..... (6.7)}$$

$$\sigma_{xy} = \frac{G\beta_s(1+\nu)}{12\pi\kappa^T(1-\nu)}\left[-y\frac{1-e^{-\xi^2}}{\xi^2} - yEi(\xi^2)\right]_{-a}^{a} \quad \text{..... (6.8)}$$

where, $r^2 = \left(x - x^{'}\right)^2 + y^2$ and other notations are the same as those defined previously.

6.4 Temperature and thermal stress analytical solution

Derivation of the temperature and thermal stresses can be obtained based on the analytical solution by (Carslaw and Jaeger 1959).

First the analytical solution for the temperature profile is

$$s\frac{T}{T_0} = -\frac{K_0(\xi)}{K_0(\beta)} \quad \text{..... (6.9)}$$

where T_0 is initial reservoir temperature (^{0}C), T is induced reservoir temperature (^{0}C), K_0 is the modified Bessel function of second kind of zero order, s is Laplace operator, $\xi = r\sqrt{s/c^T}$ and $\beta = a\sqrt{s/c^T}$,

where r is distance from the center of the wellbore, a is wellbore radius.

Second, the analytical solution for the stress profile is

For tangential stress:

$$s\frac{\sigma_{\theta\theta}}{T_0} = 2\eta\left[\frac{a}{r}\frac{K_1(\xi)}{\beta K_0(\beta)} - \frac{a^2}{r^2}\frac{K_1(\beta)}{\beta K_0(\beta)} + \frac{K_0(\xi)}{K_0(\beta)}\right] \quad \text{.....(6.10)}$$

For radial stress:

$$s\frac{\sigma_{rr}}{T_0} = -2\eta\left[\frac{a}{r}\frac{K_1(\xi)}{\beta K_0(\beta)} - \frac{a^2}{r^2}\frac{K_1(\beta)}{\beta K_0(\beta)}\right] \quad \text{.....(6.11)}$$

where $\eta = \alpha\frac{1-2\nu}{2(1-\nu)}$, which is poroelastic coefficient , α is Biot coefficient K_1 is the modified Bessel function of second kind of first order. Then the temperature and thermal

stress field are solved by taking the numerical inversion of the Laplace transform with the Stehfest (1970) algorithm.

Figure 6.2 shows transient temperature distribution near the wellbore region. In this case, initial reservoir temperature (T_0) is 200^0C and injection fluid temperature is 0^0C, wellbore radius is 0.1 m, and the thermal diffusivity of the rock is 5.1×10^{-6} m^2/sec. As the rock is assumed to be Westerly granite, only a conductive heat transfer mechanism dominates the temperature variation, and the rock gradually cools while the wellbore wall temperature keeps constant. For the diverse range of time domain, the numerical results agree well with the analytical solution. Figure 6.3 and 6.4 illustrate an induced thermal stress profile near the wellbore region. A significant induced radial tensile stress is observed and a highly tensile stress zone is induced around the wellbore, which is caused by the reaction to the rock shrinkage with the transient cooing. The magnitude of the induced tangential stress decreases with distance and gradually decays in the far-field region. Also, compression is induced behind the tensile zone because the rock shrinkage at the inner face of the wellbore during cooling tends to pull on the outer rock.

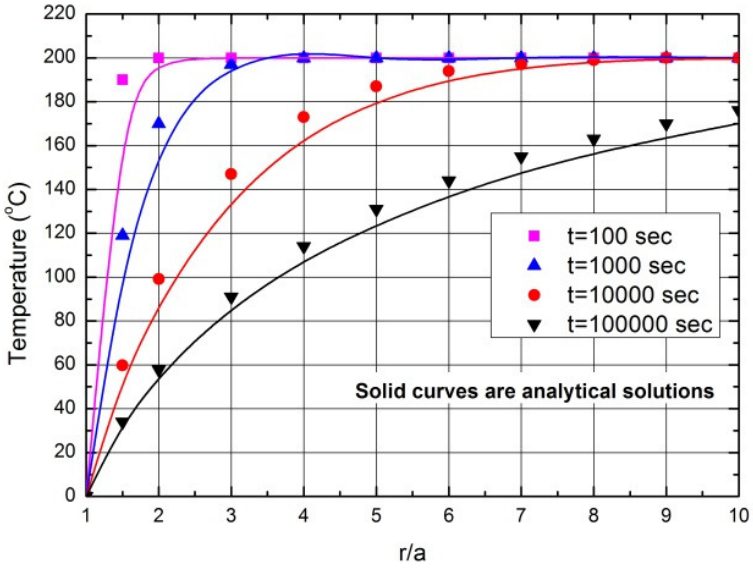

Figure 6.2 Temperature distribution around a cooled wellbore with respect to time

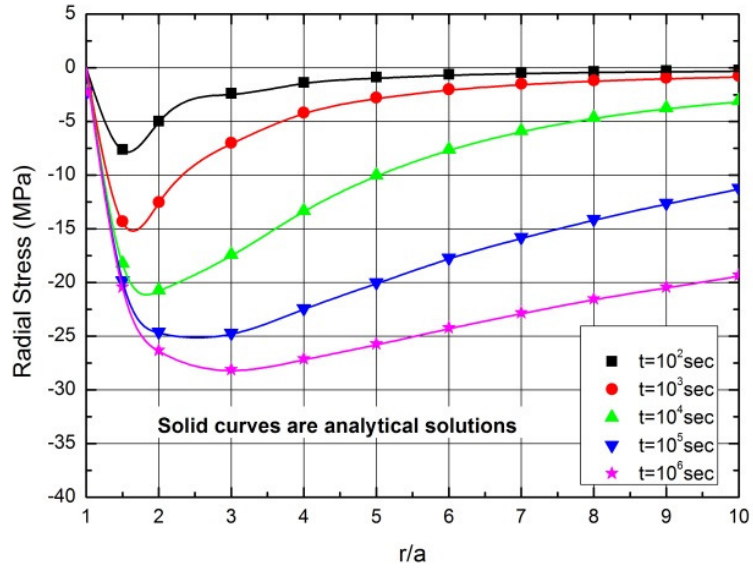

Figure 6.3 Radial stress distribution around a cooled wellbore with respect to time

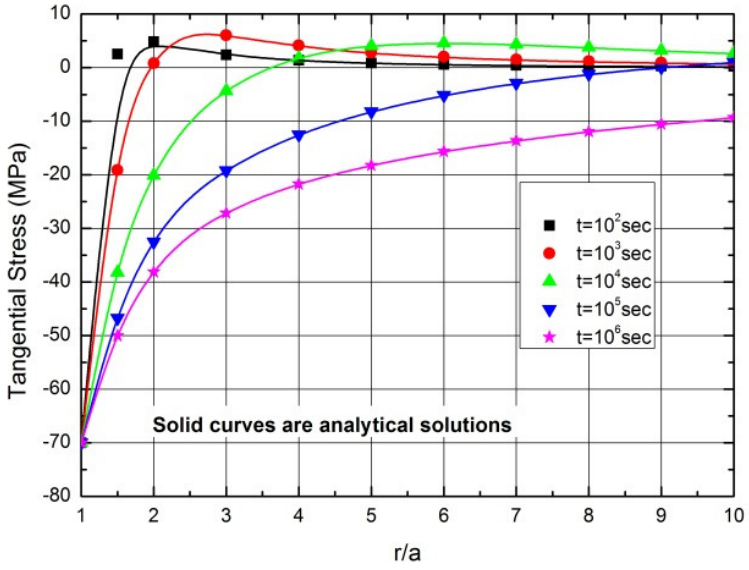

Figure 6.4 Tangential stress distribution around a cooled wellbore with respect to time

6.5 Temperature and thermal induced stress near a uniformly cooled fracture in an elastic rock

For water flooding, stimulation of shale gas reservoirs and geothermal stimulation, the temperature of the injected fluids is generally lower than the initial in-situ reservoir temperature. We considered one example of transient uniform cooling around a single main fracture in an elastic rock. Understanding temperature and the induced thermal stress field that results from the cooling helps to calculate the fracture geometry, injection rate, and pressure conditions. For this simulation, we assumed that the initial fracture length was 50 m, the initial reservoir rock temperature (T_0) was

200°C, and injection water temperature (T_w) was 20°C (Figure 6.5). Other material constants for Westerly Granite rock are presented in Table 6.1 (McTigue 1986).

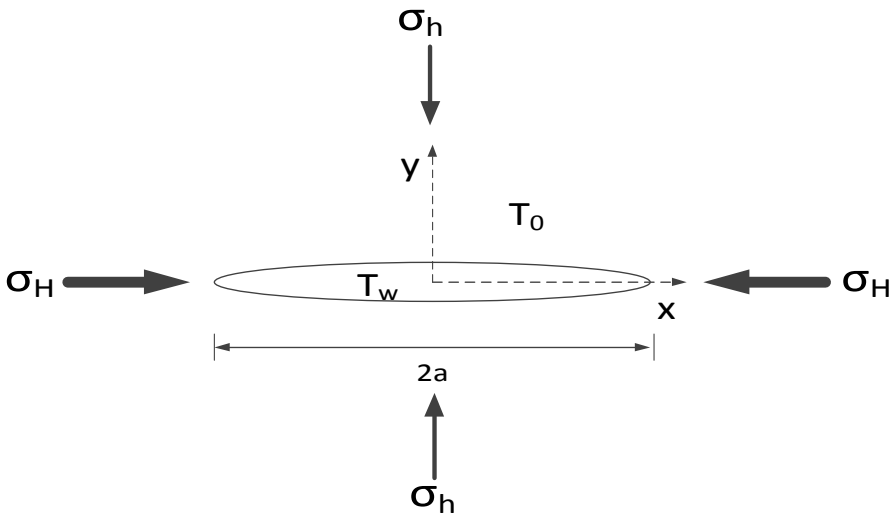

Figure 6.5 Horizontal thermal crack in an infinite thermoelastic medium

Table 6.1 The material properties of Westerly granite

Initial reservoir rock temperature, T_0 (°C)	200
Injection water temperature, T_w (°C)	20
Young's Modulus, E (GPa)	37.5
Poisson's ratio, ν	0.25
Maximum in-situ stress, σ_H (MPa)	-40
Minimum in-situ stress, σ_h (MPa)	-10
Rock thermal expansion coefficient, β_s [m/(m·°C)]	24×10^{-6}
Rock thermal conductivity, κ^T [W/(m·K)]	10.7
Rock thermal diffusivity, c^T (m^2/s)	5.1×10^{-6}
Rock density, ρ_r (kg/m^3)	2650
Water density, ρ_w (kg/m^3)	1000
Rock heat capacity, c_r (J/kg·K)	790
Water heat capacity, c_w (J/kg·K)	4200

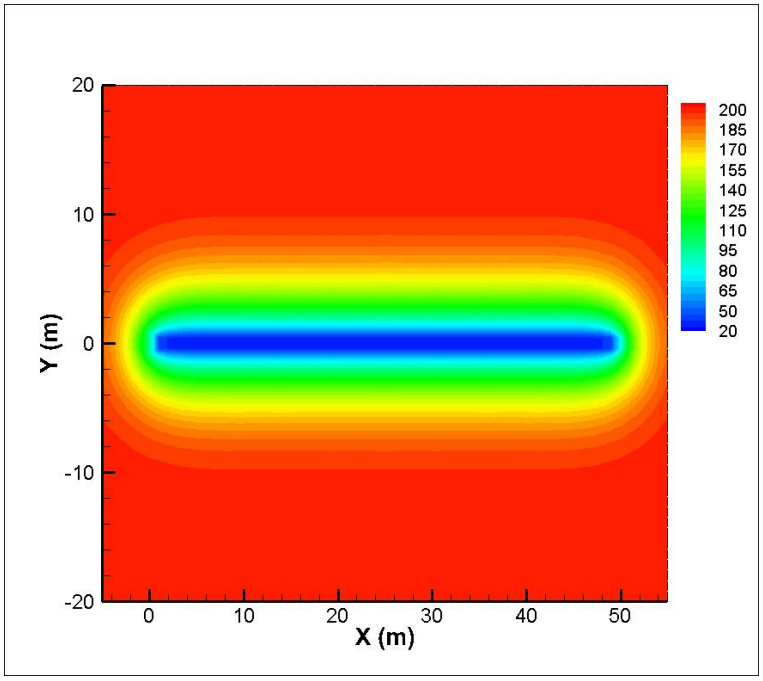

Figure 6.6 The temperature field in the rock matrix at 1 month by uniformly transient cooing around the fracture

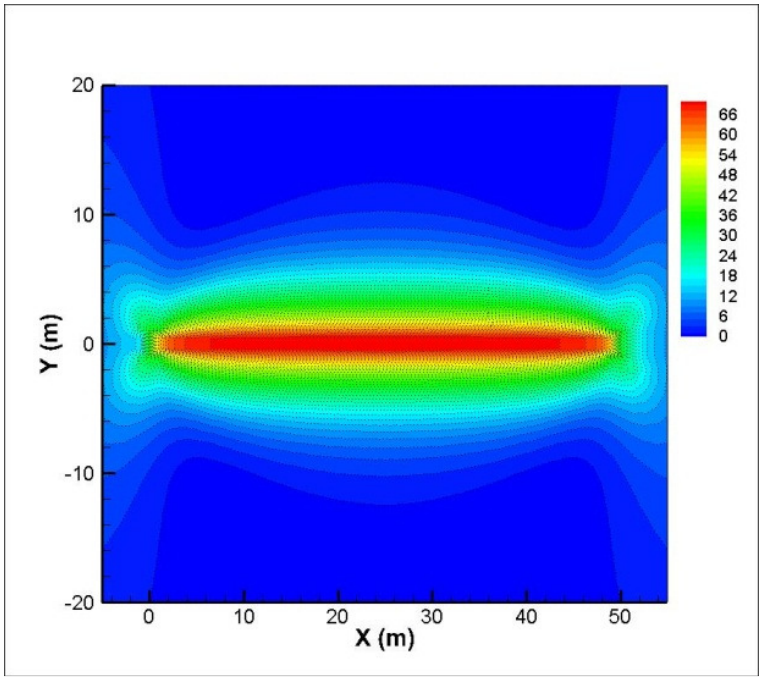

Figure 6.7 The induced tangential thermal stress field (MPa) in the rock matrix at 1 month by uniformly transient cooing around the fracture

Figure 6.6 shows the temperature field in the rock matrix at 1 month of transient cooling. As expected, the elliptical shape of the cooled zone is uniformly induced near the fracture. Along the crack surface, it remains at the injection temperature (T_w) resulting from the constant water injection.

Figure 6.7 illustrates the tangential thermal stress distribution induced by the transient cooling of the surface (Y=0m) at 1 month. As shown in the figure, the maximum tangential thermoelastic stress is around 65 MPa at the surface of cooling, which creates a zone of high tensile stress around the fracture. Usually, the tensile strength of the granite rock is from 7 to 25 MPa (Hopkins 1986), and if we apply the stress superposition principles (the highly induced tensile stresses + initial in-situ stress + low tensile strength of the rocks), we can expect that thermal fracturing will occur as long as the sum of the total stresses (in-situ plus thermal induced stress) exceeds the tensile strength of the rock.

Figure 6.8 shows the thermally induced tangential (σ_{xx}) and normal (σ_{yy}) stress distribution corresponding to three different cooling times around the main fracture. In this figure, x-axis (Y) is defined as the vertical distance from the main fracture surface. First, for the tangential stress (σ_{xx}), a largely induced tensile stress component has formed very close to the fracture surface at early time (10^6 sec). However, with increasing cooling time, it tends to move into the deeper region of the reservoir rock as expected. Second, the normal stress (σ_{yy}), is relatively uniform along the vertical direction; its magnitude is initially small and then increases slowly up to 60 MPa at 10^{10}

seconds. With this, we can say that the thermoelastic stress reduction parallel to the fracture ($\Delta\sigma_H$) exceeds the thermoelastic stress reduction perpendicular to the fracture ($\Delta\sigma_h$) in the cooled region. As a consequence, this phenomenon results in reducing the difference between total stresses (in-situ plus thermal induced stress) with the cooled areas that are parallel and perpendicular to the main fracture (Figure 6.9). Subsequently, secondary fractures can form perpendicular to the main fracture.

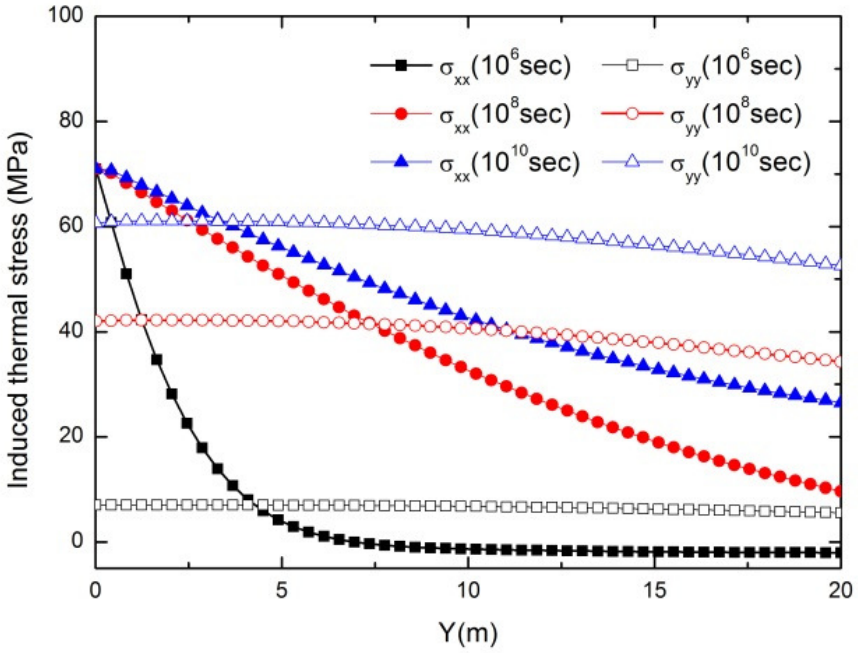

Figure 6.8 The thermally induced tangential stress (σ_{xx}) and normal stress (σ_{yy}) corresponding to three different cooling times around the main fracture

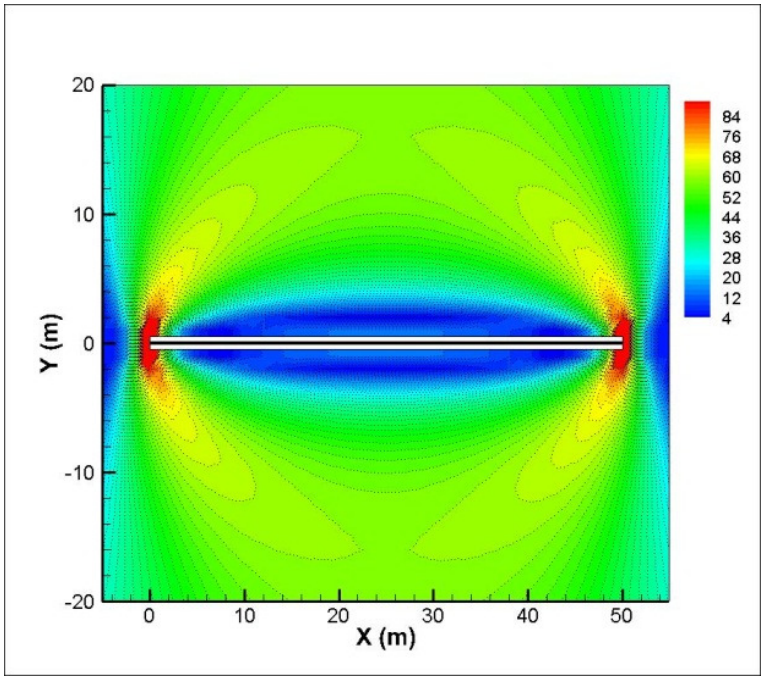

Figure 6.9 The total (in-situ + induced) principal stress difference in the rock matrix at 1 month by transient cooling around the fracture

6.6 Thermal fracturing

6.6.1 Single main thermal fracture propagation in an elastic rock

The previous section illustrated the possibility of thermal fracture propagation caused by thermal stresses in an unconventional reservoir induced by uniform cooling. In this section, we simulate the propagation of a single fracture to find the impact of cooling on fracture orientation and its length. Here we consider two situations; one is that only the initial crack is uniformly cooled while the other is that the newly created fractures are also cooled to the temperature of the initial fracture.

For the simulation, the initial length of the fracture is 2 m and it is oriented along a 45° angle with regard to the x-axis. The maximum and minimum in-situ stresses are 20 MPa and 10 MPa, and the internal fluid pressure is 10.5 MPa. Initial rock reservoir temperature is 200°C and injection water temperature is 20°C. Figure 6.10 compares the thermal fracture orientation and length of uncooled and cooled cases. The result indicates that the cooling of both initial and newly created fractures can boost their penetration length. To be specific, at 8×10^{7}seconds, the cooling both initial and extended fracture propagates approximately 28% more than the uncooled ones. However, the orientation of those thermal fractures is mostly identical paths. These results tell us that the impact of cooling enhances deeper penetration of thermal fractures but it may not be involved in changes in orientation of those fractures.

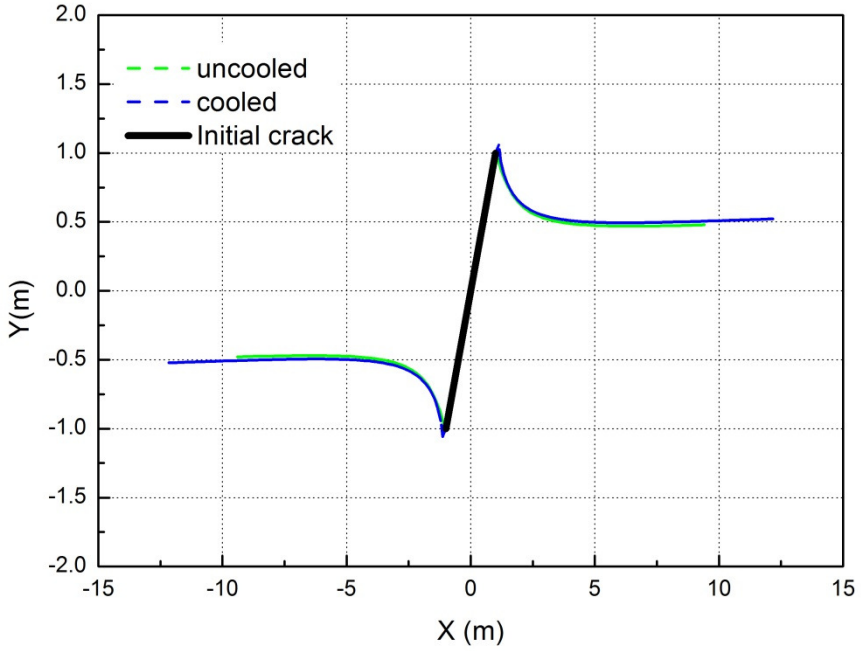

Figure 6.10 The propagation orientation and path of the main thermal fracture corresponding to uncooled and cooled cracks

6.6.2 Multiple main and secondary thermal fracture propagation in an elastic rock

We have shown that a single main thermal fracture can be propagated deeply into the geothermal reservoir under certain conditions. For the multiple fracture propagation, the fracture propagation path is significantly influenced by the mechanical interaction between neighboring cracks altering the stress state around the fracture through the fracture growth behavior (Nemat-Nasser et al. 1978; Tarasovs and Ghassemi 2010). The mechanical interaction indicates that at early time, the secondary fractures may be spaced closely and of very short penetration. However, with the elapse of time, some will grow deeper penetration, and others will stop.

We considered propagation of multiple main and secondary thermal fractures under transient cooling in a reservoir.

Figure 6.11 shows the formation of expected secondary fractures around the main fracture. Initially these cracks are located at random locations, but keeping the nature of geometry such as crack spacing, d, as a constant value (Tarasovs and Ghassemi 2010). For the numerical approach, once thermal induced stress are computed at the collocation points using Eq. 6.6 through 6.8, then these are applied as surface tractions on the fracture surface to simulate crack propagation in the thermal field using the stress superposition principle (in-situ + induced thermal stress). For closed cracks, the penalty method is used to maintain appropriate contact with crack surfaces without penetration.

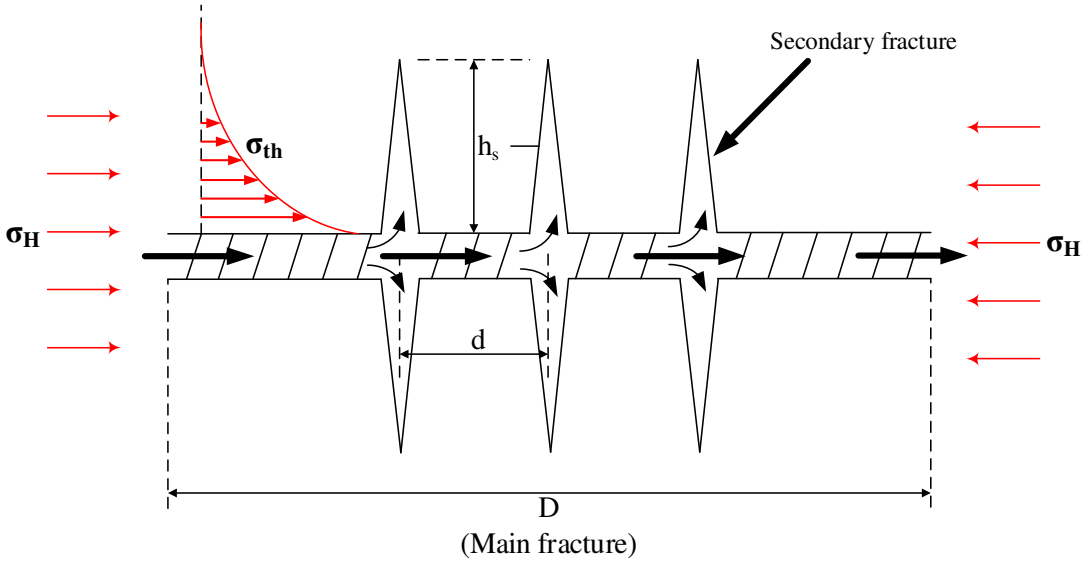

Figure 6.11 Secondary thermal cracks geometry perpendicular to the main fracture

Here the length of the main fracture (D) is 50 m, and it was subdivided into 50 segments. For the secondary fracture, the initial length (h_s) is 5 m with 10 segments, and average crack spacing (d) is 10 m. The maximum and minimum in-situ stresses are 20 MPa and 10 MPa, and the internal fluid pressure is 20.5 MPa which is slightly higher than the maximum in-situ stress. Other material constants are same as the same as the one presented in Table 6.1.

Figure 6.12 shows the secondary fracture growth path at the time of 2 years, in which the temperature difference (ΔT) between the fracture surface and the initial reservoir rock is 180°C. The location of the main fracture in this figure is along the x-axis from 0 to 50 m. The fractures at the end of the array propagate faster than the middle one because they are only opposed by another fracture on one side, which causes them to have less mechanical interaction among the three fractures. Also, this mechanical interaction among those fractures induces the outward crack extension (except for the middle one) since the interacting forces repel each other.

Figure 6.13 depicts the same simulation results except that the temperature difference between the fracture surface and the initial reservoir rock is 120°C. As shown and compared with Figure 6.12, the faster cooling rate produces longer crack extension of the secondary thermal fractures. This implies that the faster cooling induces a higher tensile stress zone around the fracture, which tends to produce larger driving forces to make them penetrate deeper into the geothermal reservoir.

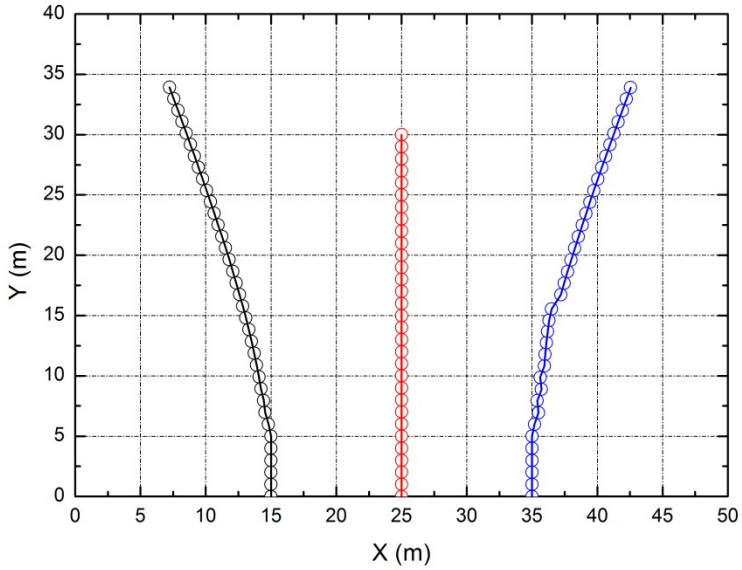

Figure 6.12 The propagation of three secondary fractures with spacing 10 m, in which the temperature difference (ΔT) between the fracture surface and the initial reservoir rock is 180°C after 2 years

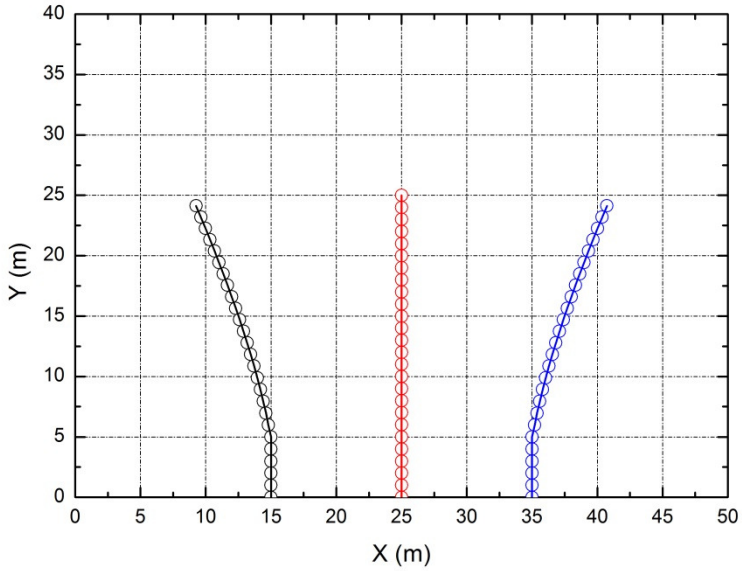

Figure 6.13 The propagation of three secondary fractures with spacing 10 m, in which the temperature difference (ΔT) between the fracture surface and the initial reservoir rock is 120°C after 2 years

6.6.3 Poro-thermally induced fracture propagation

The examples shown in section 6.6.2 involved only thermoelastic rock, neglecting the pore pressure effect. However, most rocks do have a pore fluid such as oil or water. This pore fluid pressure can influence the fracture propagation behavior of the porous rock.

In this section, the influence of the pore pressure on the fracture propagation and interaction between fractures in poro-thermoelastic rock is considered. Let us consider an example of one main and three secondary fractures induced by transient cooling in the poro-thermoelastic rock in which all the main and secondary fractures are cooled. In this case, both the initial fracture formation and the boundary conditions were exactly the same as the example in section 6.6.2. To investigate the influence of pore pressure on fracture propagation direction, three different initial pore pressures (P_0) were considered. They are 0MPa, 5MPa, 10MPa, respectively. The injection water temperature (T_w) is 20°C and the initial reservoir rock temperature (T_0) is 200°C. Other material constants are the same as in Table 6.1.

Figure 6.14 shows the secondary fracture growth path at the time of 2 years, in which three different initial pore pressures exist. In the absence of the initial pore pressure (0 MPa), a roughly deviating path of tensile fracture propagation is observed, which is mostly identical to the thermoelastic propagation result (see Figure 6.12). However, when an initial pore pressure exists (5 and 10 MPa), numerical simulation

results indicate that the fracture is more rapidly deviated. This is because of the distribution of the total induced pore pressure field.

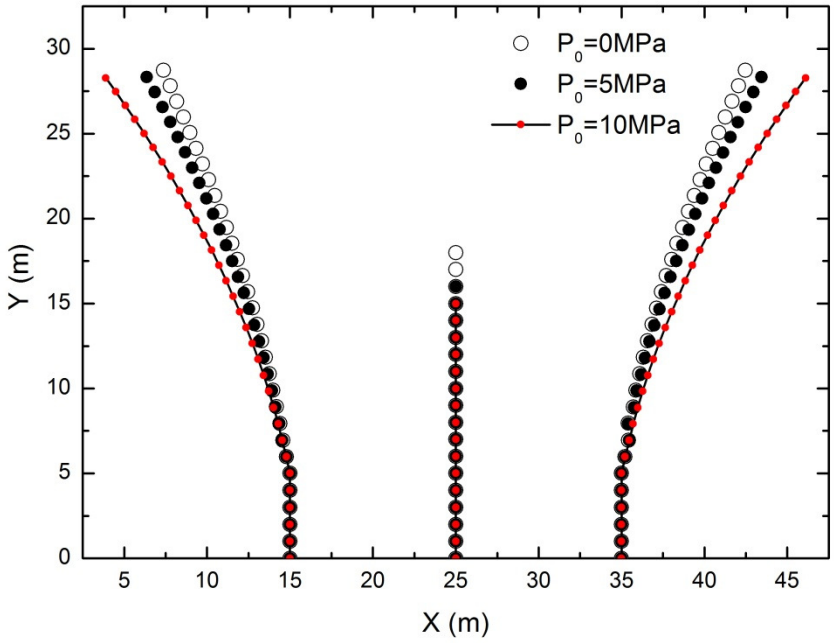

Figure 6.14 The initial pore pressure influence on the propagation of three secondary fractures with spacing 10 m, in which the temperature difference (ΔT) is 180°C after 2 years

Figures 6.15 and 6.16 illustrate the total induced pore pressure distribution at the time of 2 years when the initial pore pressure is 0 and 10 MPa respectively. As seen, the higher total induced pore pressure makes the crack more deviated. Therefore, the orientation of multiple fractures in poro-thermo-elastic rock is influenced not only by the magnitude of the total induced pore pressure, but also their mechanical interactions (outward crack growth) during the propagation.

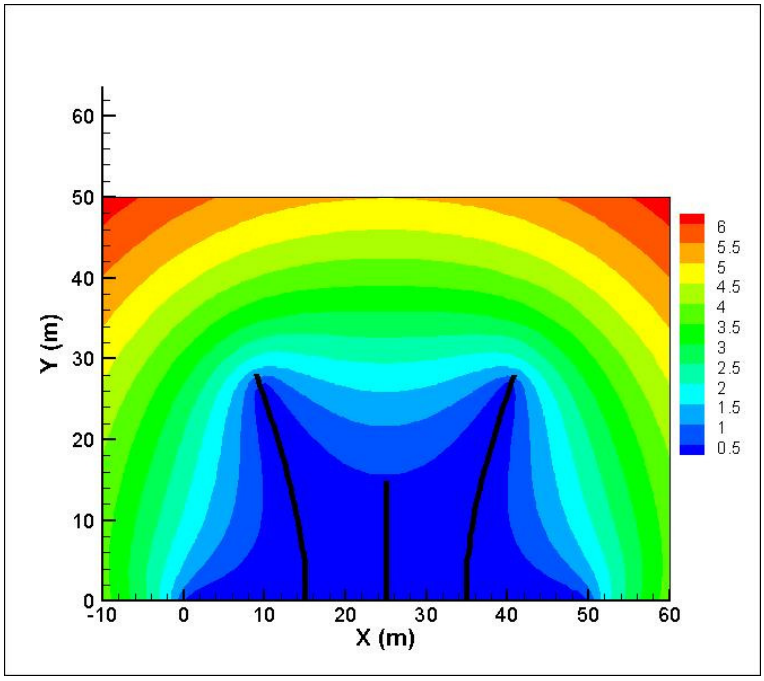

Figure 6.15 Total induced pore pressure field (MPa) after 2 years when the initial pore pressure (P_0) is 10MPa

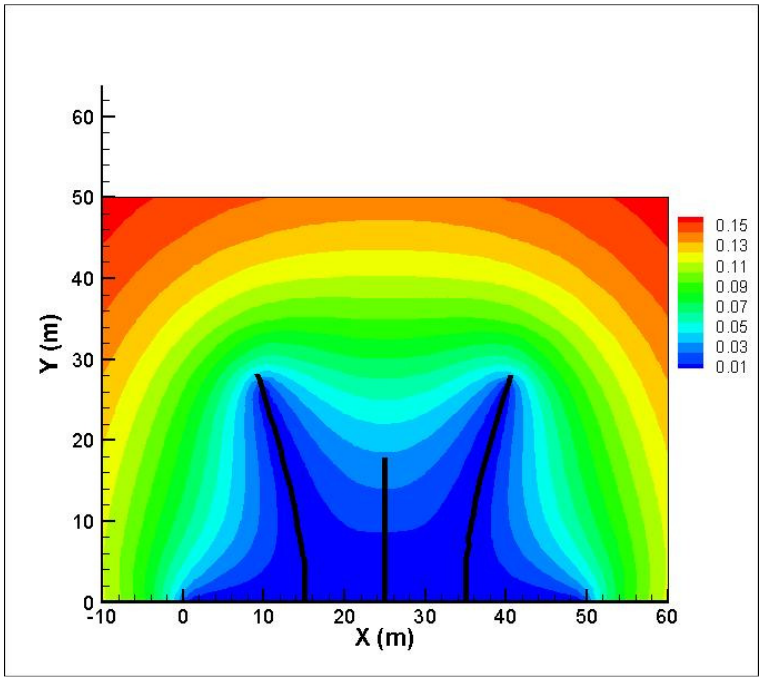

Figure 6.16 Total induced pore pressure field (MPa) after 2 years when the initial pore pressure (P_0) is 0 MPa

7. ROCK MECHANICS APPLICATIONS

7.1 Thermo-hydraulically induced fracture growth in the Haynesville shale formation

Natural gas production in shale gas reservoirs has proven to be the hottest trends in North America's onshore oil and gas industry, and many shale plays are being successfully developed throughout the United States (Britt and Schoeffler 2009). Technological advances in horizontal drilling and hydraulic fracturing stimulation have made shale oil and gas production economically conspicuous (Guo et al. 2012). The Haynesville shale play is one of the most active formations in the United States. The petrophysical evaluations have been recently provided for a comprehensive description of this formation (Mullen et al. 2007; Parker et al. 2009; Rickman et al. 2008), which is critical for the design of stimulation treatments in unconventional reservoirs.

In spite of this abundant information about the shale play, realistic hydraulic fracturing results in shale have yet to be found. Therefore, in this work, we simulated thermo-hydraulically induced fracture propagation in the Haynesville shale formation with realistic reservoir conditions based on the petrophysical evaluations and compared this with the results in the Westerly granite rock formation to observe the differences between the two cases.

Figure 7.1 illustrates one injection well and two wing fractures in the Haynesville formation. It assumes that the wellbore radius is 0.1 m and the initial length of the two fractures is 1 m, respectively. The material parameters for shale are used from the dataset in Tao and Ghassemi (2010) and shown in Table 7.1. As shown in Table 7.2, for

the initial reservoir condition, the initial reservoir temperature is 165.5°C and the injecting fluid temperature is 30.5°C. The initial pore pressure is 12 MPa and the injecting fluid pressure is 28.5 MPa. The maximum in-situ stress assumes 18 MPa and the minimum in-situ stress is 17 MPa. The material parameters for Westerly granite rock used the dataset from McTigue (1986) are shown in Table 7.3.

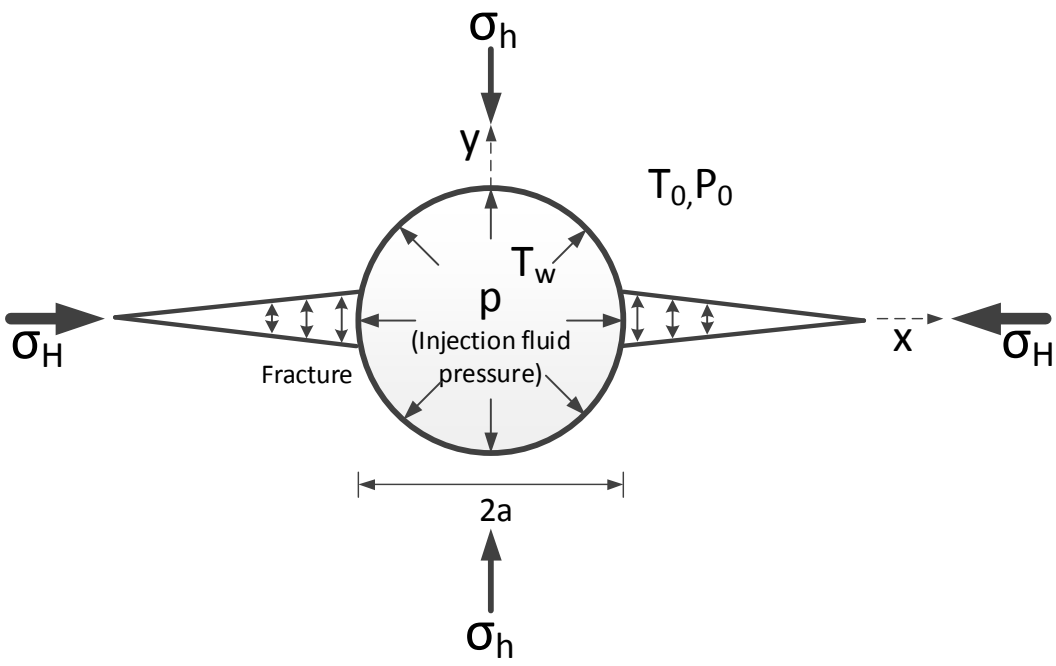

Figure 7.1 An injection well and two wing fractures in the Haynesville shale formation

Table 7.1 The poro-thermoelastic parameters of Haynesville shale formation

Parameter	value
Young's Modulus, E (GPa)	13.8
Poisson's ratio, ν	0.22
Undrained Poisson's ratio, ν_u	0.46
Solid bulk Modulus, K_s (GPa)	241.6
Fluid bulk Modulus, K_f (GPa)	2.5
Skempton's coefficient, B	0.915
Fluid diffusivity, c_f (m^2/s)	4.5×10^{-6}
Fluid viscosity, μ_f (Pa·s)	3.0×10^{-4}
Rock thermal expansion coefficient, β_s [m/(m·°C)]	1.8×10^{-5}
Rock thermal conductivity, κ^T [W/(m·K))	3.2
Rock thermal diffusivity, c^T (m^2/s)	1.6×10^{-6}
Rock heat capacity, c_r (J/kg·K)	770
Water heat capacity, c_w (J/kg·K)	4200
Rock permeability, κ (m^2)	1.0×10^{-19}
Rock density, ρ_r (kg/m^3)	2600
Water density, ρ_w (kg/m^3)	1000
Biot's coefficient, α	0.966
Porosity, ϕ	0.10

Table 7.2 List of parameters for the initial reservoir condition in Haynesville shale formation

Parameter	value
Maximum in-situ stress, σ_H (MPa)	-18
Minimum in-situ stress, σ_h (MPa)	-17
Initial pore pressure, P_0 (MPa)	12
Injecting fluid pressure, p (MPa)	28.5
Formation temperature, T_0 (°C)	165.5
Injecting fluid temperature, T_w (°C)	30.5

Table 7.3 The poro-thermoelastic parameters of Westerly granite rock

Parameter	value
Young's Modulus, E (GPa)	37.5
Poisson's ratio, ν	0.25
Undrained Poisson's ratio, ν_u	0.33
Solid bulk Modulus, K_s (GPa)	45
Fluid bulk Modulus, K_f (GPa)	2.5
Skempton's coefficient, B	0.85
Fluid diffusivity, c_f (m^2/s)	6.16×10^{-5}
Fluid viscosity, μ_f (Pa·s)	3.547×10^{-4}
Rock thermal expansion coefficient, β_s [m/(m·°C)]	2.4×10^{-5}
Rock thermal conductivity, κ^T [W/(m·K)]	10.7
Rock thermal diffusivity, c^T (m^2/s)	5.1×10^{-6}
Rock heat capacity, c_r (J/kg·K)	790
Water heat capacity, c_w (J/kg·K)	4200
Rock permeability, κ (m^2)	4.0×10^{-19}
Rock density, ρ_r (kg/m^3)	2650
Water density, ρ_w (kg/m^3)	1000
Biot's coefficient, α	0.444
Porosity, ϕ	0.01

Figure 7.2 and 7.3 show total induced pore pressure variations as a function of time in Haynesville shale and Westerly granite rock. In shale, the fracture continuously grows until 30 days and more; but in granite rock, the fracture stops growing at 20 days. This is because the stress intensity factor at the tip in shale is higher than it is in granite so that the thermo-hydraulically induced fracture can grow farther into the formation under the same amount of the injecting pressure. Also, we can consider the magnitude of fracture toughness (K_{Ic}) of both rocks. It is material properties obtained from the

experimental work. In this case, in shale, K_{Ic} is 1.65MPa√m (Abbas et al. 2013), but in granite it is 1.9MPa√m (McKinney et al. 2008). So in the granite, we have to use more injecting pressure than in shale for the crack to extend enough to raise the productivity of the reservoir.

Figures 7.4 and 7.5 show vertical stress (σ_{yy}) variations as a function of time in the Haynesville shale and Westerly granite rock. The numerical results indicate that the vertical stress contour has the same configuration in both cases, which means the stress is not dependent on material properties, but on the magnitude of fluid pressure once the fracture starts to propagate.

The examples of secondary thermo-hydraulic multiple fracture propagation in Haynesville shale and Westerly granite rock are plotted in Figure 7.6 and 7.7. The results show that the secondary fractures in Haynesville can also extend to farther distances than in granite under the same reservoir conditions. This indicates that the multiple fracture growth behavior in shale and granite is entirely consistent with the previous examples.

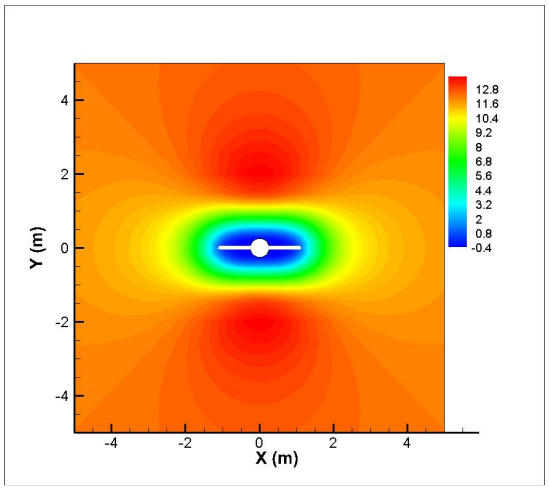

(a) 1 day

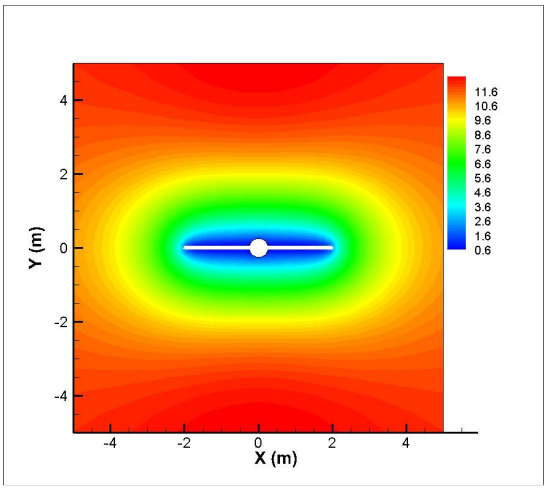

(b) 10 days

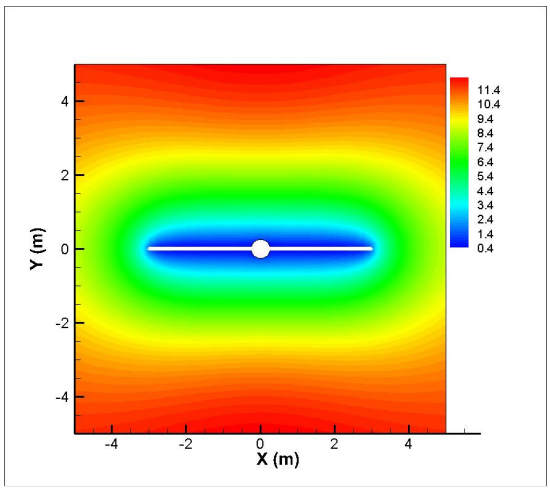

(c) 20 days

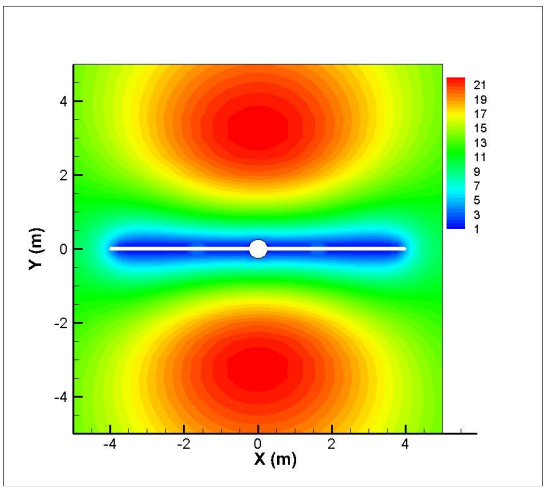

(d) 30 days

Figure 7.2 Pore pressure variations (MPa) as a function of time (a) 1 day (b) 10 days (c) 20 days and (d) 30 days in Haynesville shale formation

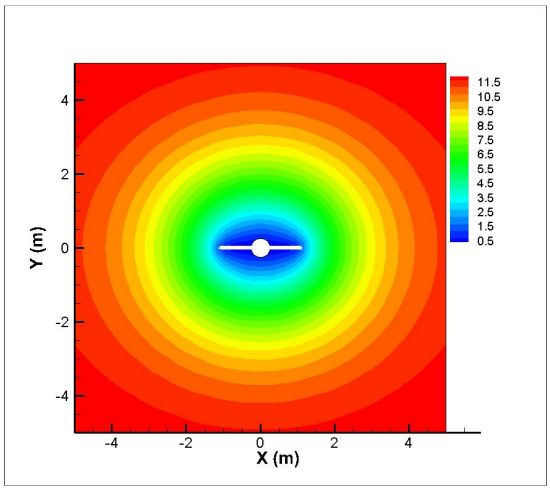

(a) 1 day

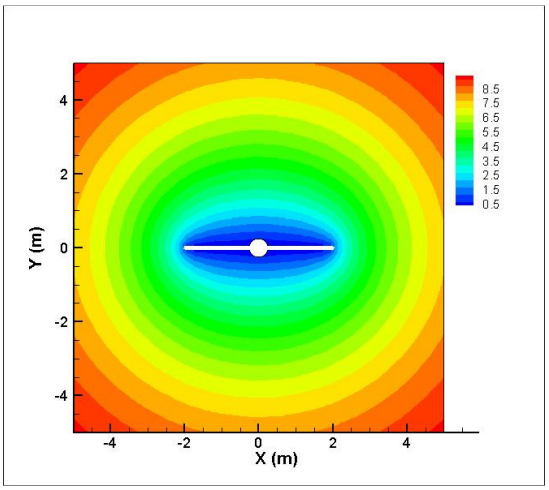

(b) 10 days

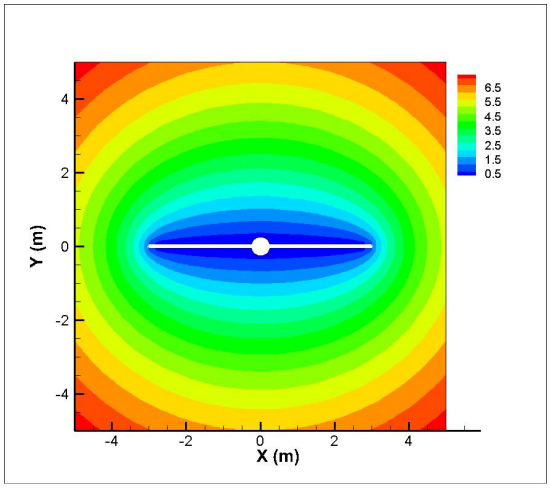

(c) 20 days

Figure 7.3 Pore pressure variations (MPa) as a function of time (a) 1 day (b) 10 days and (c) 20 days in Westerly granite rock formation

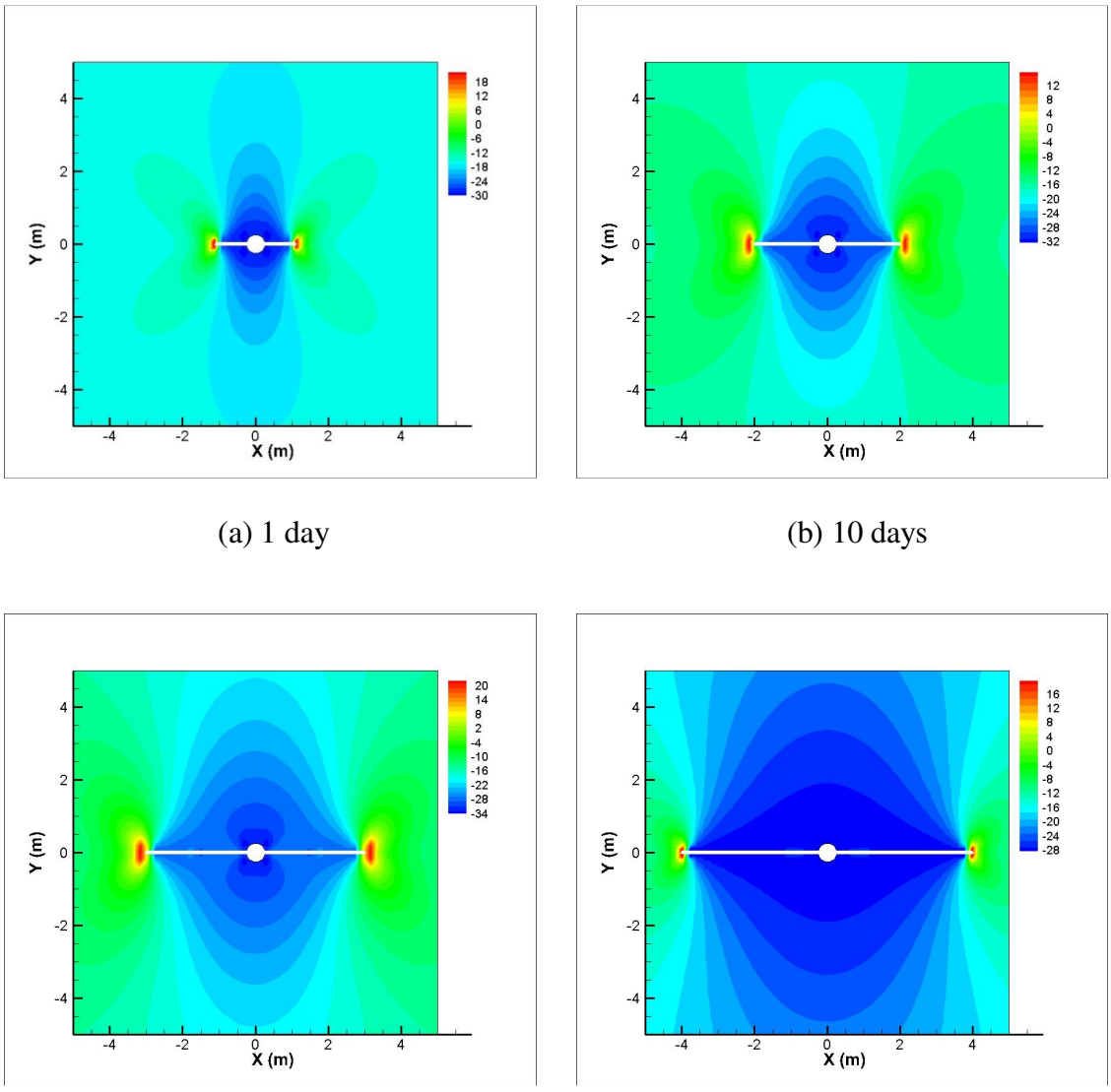

(a) 1 day

(b) 10 days

(c) 20 days

(d) 30 days

Figure 7.4 Vertical stress (σ_{yy}) variations (MPa) as a function of time (a) 1 day (b) 10 days (c) 20 days and (d) 30 days in Haynesville shale formation

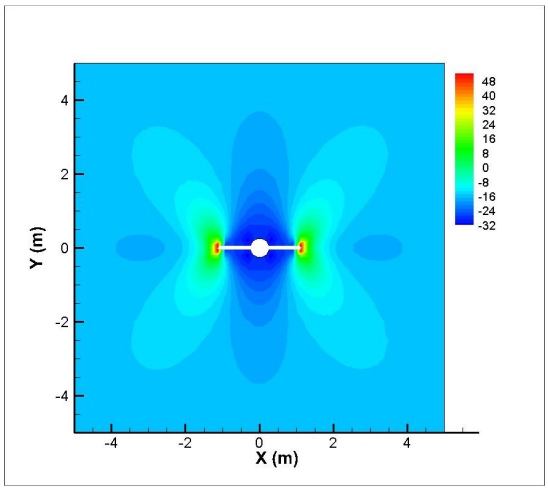

(a) 1 day

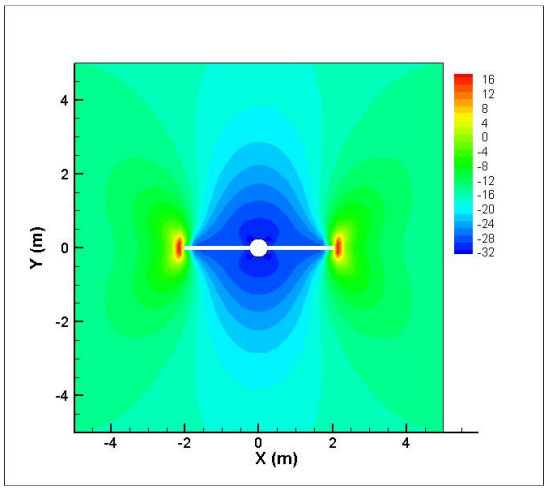

(b) 10 days

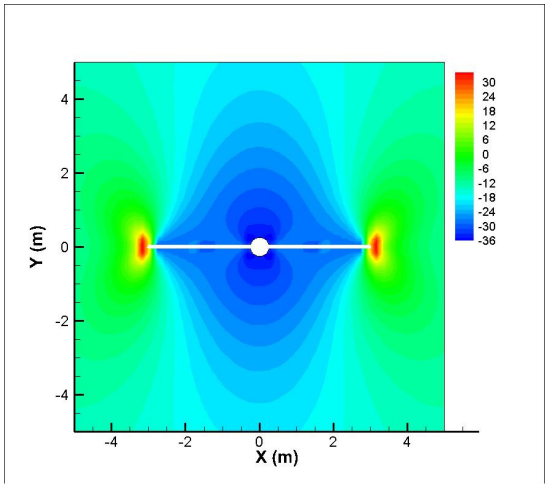

(c) 20 days

Figure 7.5 Vertical stress (σ_{yy}) variations (MPa) as a function of time (a) 1 day (b) 10 days and (c) 20 days in Westerly granite rock formation

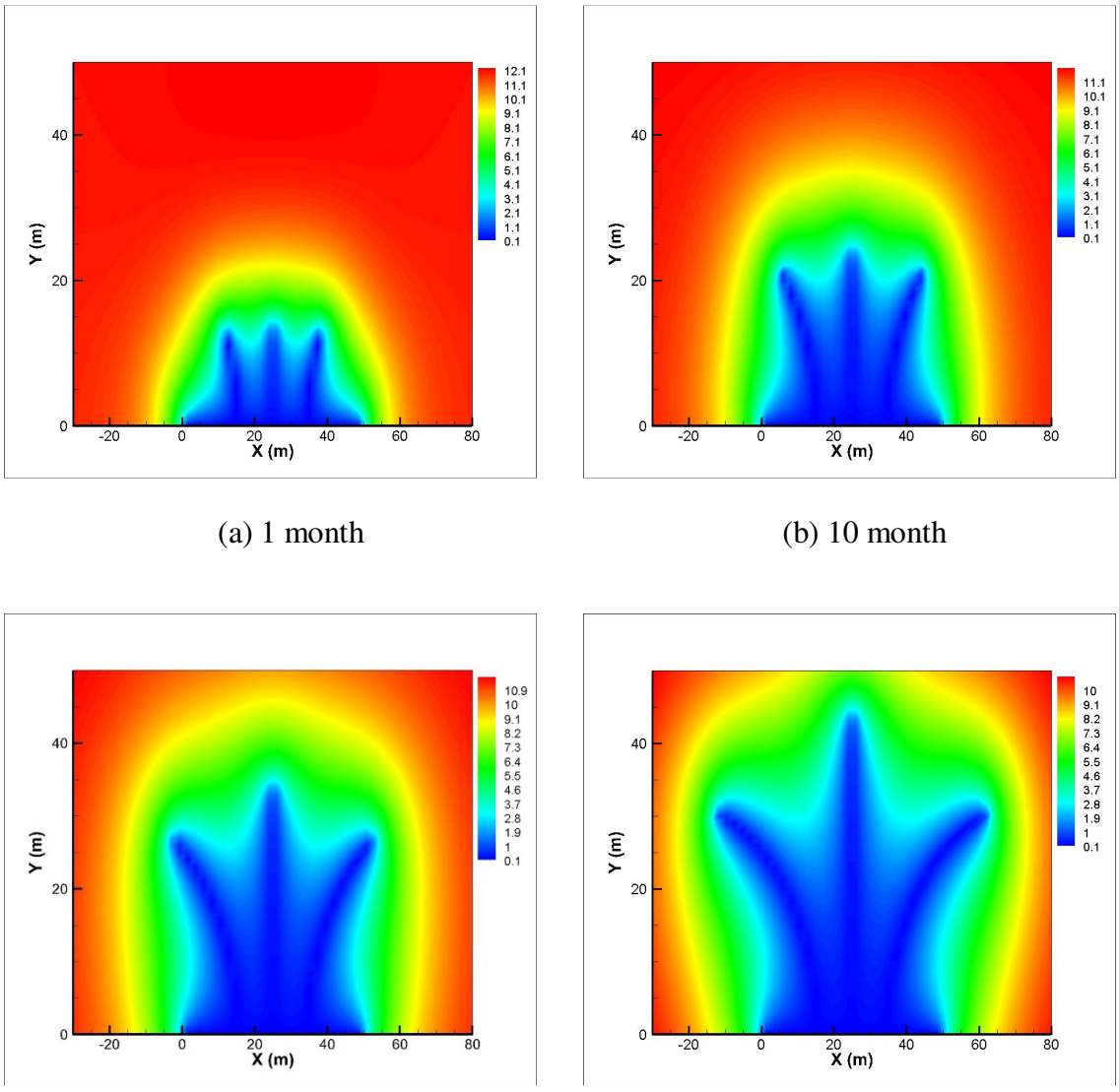

(a) 1 month

(b) 10 month

(c) 20 month

(d) 30 month

Figure 7.6 Pore pressure distribution (MPa) during the secondary thermo-hydraulic induced multiple fracture propagation in Haynesville shale formation

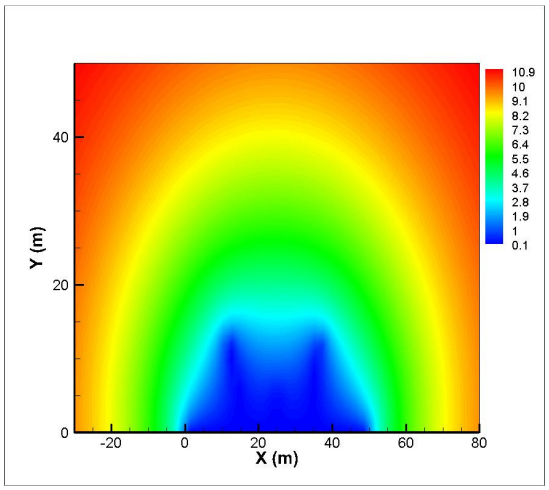

(a) 1 month

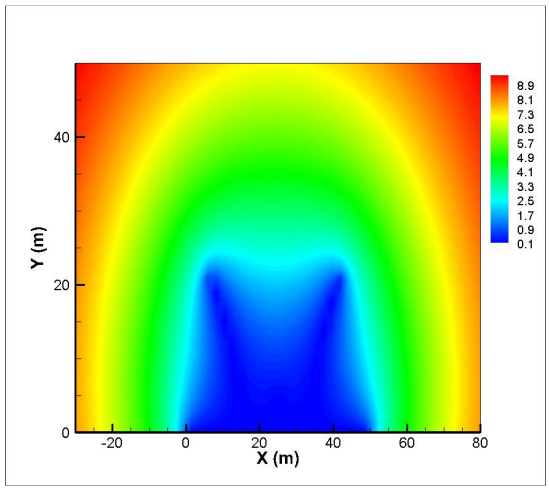

(b) 10 month

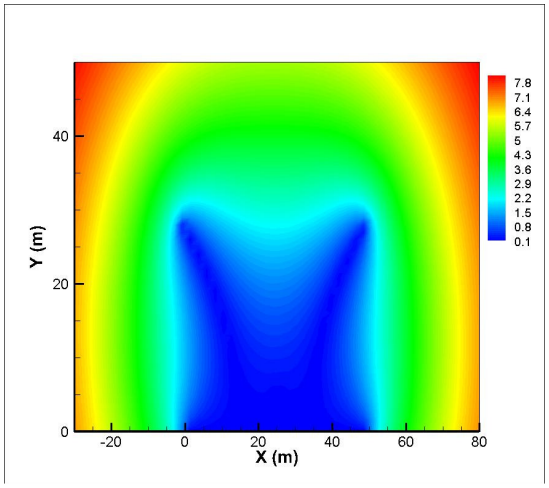

(c) 20 month

Figure 7.7 Pore pressure distribution (MPa) during the secondary thermo-hydraulic induced multiple fracture propagation in Westerly granite rock formation

8. CONCLUSIONS AND RECOMMENDATIONS

This work developed a numerical fracture propagation model in response to fully coupled thermo-poroelastic effect using the boundary element method. This model is based on the linear coupled theory of poroelasticity and thermoelasticity. The displacement discontinuity method and the fictitious stress method were used to solve single/multiple fractures as well as borehole problems. The influence of pore pressure and temperature variations on the fracture propagation length and orientation as well as stress and pore pressure distribution near hydraulically/thermally induced fractures was investigated in isotropic and homogeneous rock formations with a plane strain assumption.

First of all, we showed the general poroelastic and thermo-poroelastic response of a stationary crack in rock to demonstrate their effects on total stress and pore pressure variations near the crack region. We also analyzed the impact of the pore fluid diffusion on the transient crack aperture and evaluated the evolution of the stress intensity factor between two limiting poroelastic behaviors (drained and undrained conditions). In addition, we also examined the influence of heat diffusion on the stress and pore pressure variations near the single crack.

Second, the linear elastic fracture mechanics (LEFM) theory was introduced to study the general nature of the stress intensity at the crack tip under mixed-mode conditions. The stress intensity factor was evaluated at the crack tip in terms of the displacement discontinuities formulation. Numerical examples of pressurized crack

propagation in elastic rock were studied. The results show that if a higher fluid pressure is injecting into the crack under biaxial in-situ stresses, it makes the crack less oriented to the maximum in-situ stress direction. Also the pressurized crack propagates with rapid reorientation under larger in-situ stress anisotropy.

Third, in poroelastic fracture propagation analysis, we reviewed an analytical approach to observe insight into the nature of the pore pressure field in the vicinity of hydraulic fractures. Then fracture tip stress analysis was examined to consider the stress and pore pressure distribution around the crack tip between drained and undrained conditions. we also simulated poroelastic fracture propagation examples to investigate the influence of pore pressure on the crack extension path. Results indicate that in very fast crack growth regimes, the effect of pore fluid diffusion on the crack growth path is negligible because of the high crack propagation velocity. However, in very slow regimes, the pore fluid diffusion effect is significant in that it changes the local stress state around the crack tip, which makes the crack grow to different orientation.

Fourth, we studied thermal fracture propagation induced by temperature differences between reservoir rock and wellbores/fractures. The thermal stress and temperature variations during cooling were analytically derived, and numerical examples were verified with an analytical solution. The example of a uniformly cooled crack was simulated to capture the thermally induced stresses and temperature variations as a function of time. Results demonstrate that thermoelastic stress along the tangential direction creates a zone of high tensile stress around the fracture, and thermal fracturing can occur as long as the sum of the total stresses exceeds the tensile strength of the rock.

In addition, we simulated the propagation of a single fracture to find the impact of cooling on fracture orientation and its length. Results show that cooling enhances deeper penetration of thermal fractures but it may not be involved in the orientation change of those fractures. We also considered propagation of multiple main and secondary thermal fractures. The numerical results imply that faster cooling induces zones of higher tensile stress which tend to produce larger driving forces to make the secondary fractures penetrate deeper into the reservoir. Then we repeated this example considering the initial pore pressure to capture the influence of pore pressure on the fracture propagation and interaction between fractures. Results show that the fracture is more rapidly deviated when the initial pore pressure is higher because of the total induced pore pressure around the fractures.

Last, we simulated thermo-hydraulic induced fracture propagation in the Haynesville shale and compared it with the results in Westerly granite rock to observe the distinct aspects of the shale fracturing under thermo-poroelastic effect. Results show that the thermo-hydraulically induced fracture grows farther in the Haynesville shale formation because the stress intensity factor at the tip in shale is higher than it is in granite under the same amount of injecting pressure.

For the recommendations, in this dissertation, we only considered single-phase flow models with isotropic and homogeneous rock properties. Therefore, the following studies are recommended for future work. Rock anisotropy and inhomogeneity would be better for the practical behavior of fracture propagation in rock. Also multi-phase flow

with a coupled geomechanical reservoir simulator would be more realistic for real-scale reservoir characterization and stimulation.

REFERENCES

Abbas, S., Lecampion, B., and Prioul, R. 2013. Competition between Transverse and Axial Hydraulic Fractures in Horizontal Wells. Paper presented at the 2013 SPE Hydraulic Fracturing Technology Conference, The Woodlands, TX, USA. SPE-163848-MS.

Aliabadi, M.H. and Rooke, D.P. 1991. *Numerical Fracture Mechanics*. Solid Mechanics and Its Applications. Southampton, UK: Computational Mechanics Publications

Anderson, T.L. 2005. *Fracture Mechanics: Fundamentals and Applications*. Boca Raton, FL: Taylor & Francis.

Atkinson, B.K. 1987. *Fracture Mechanics of Rock*. Academic Press Geology Series. London: Academic Press.

Atkinson, C. and Craster, R.V. 1991. Plane-Strain Fracture in Poroelastic Media. *Proceedings of the Royal Society of London Series a-Mathematical Physical and Engineering Sciences* **434** (1892): 605-633.

Banerjee, P.K. and Butterfield, R. 1981. *Boundary Element Methods in Engineering Science*. London: McGraw-Hill Book Co. (UK).

Biot, M.A. 1941. General Theory of Three-Dimensional Consolidation. *Journal of Applied Physics* **12** (2): 155-164.

Biot, M.A. 1955. Theory of Elasticity and Consolidation for a Porous Anisotropic Solid. *Journal of Applied Physics* **26** (2): 182-185.

Biot, M.A. 1956a. Theory of Propagation of Elastic Waves in a Fluid-Saturated Porous Solid .1. Low-Frequency Range. *Journal of the Acoustical Society of America* **28** (2): 168-178.

Biot, M.A. 1956b. Theory of Propagation of Elastic Waves in a Fluid-Saturated Porous Solid .2. Higher Frequency Range. *Journal of the Acoustical Society of America* **28** (2): 179-191.

Bobet, A. 2000. The Initiation of Secondary Cracks in Compression. *Engineering Fracture Mechanics* **66** (2): 187-219.

Bobet, A. 2001. Numerical Simulation of Initiation of Tensile and Shear Cracks. *Rock Mechanics in the National Interest, Vols 1 and 2*: 731-738.

Bobet, A. and Mutlu, O. 2005. Stress and Displacement Discontinuity Element Method for Undrained Analysis. *Engineering Fracture Mechanics* **72** (9): 1411-1437.

Boone, T.J. and Ingraffea, A.R. 1990. A Numerical Procedure for Simulation of Hydraulically-Driven Fracture Propagation in Poroelastic Media. *International Journal for Numerical and Analytical Methods in Geomechanics* **14** (1): 27-47.

Boone, T.J., Ingraffea, A.R., and Roegiers, J.C. 1991. Simulation of Hydraulic Fracture Propagation in Poroelastic Rock with Application to Stress Measurement Techniques. *International Journal of Rock Mechanics and Mining Sciences & Geomechanics Abstracts* **28** (1): 1-14.

Brebbia, C.A. and Dominquez, J. 1992. *Boundary Elements : An Introductory Course*. Southampton, UK: Computational Mechanics Publications

Britt, L.K. and Schoeffler, J. 2009. The Geomechanics of a Shale Play: What Makes a Shale Prospective! Paper presented at the SPE Eastern Regional Meeting, Charleston, WV. SPE-125525-MS.

Carslaw, H.S. and Jaeger, J.C. 1959. *Conduction of Heat in Solids*. Oxford,: Clarendon Press.

Carvalho, J.L. 1990. Poroelastic Effects and Influence of Material Interfaces on Hydraulic Fracturing. PhD dissertation, University of Toronto,Toronto,Ontario,Canada

Crouch, S.L. 1976. Solution of Plane Elasticity Problems by Displacement Discontinuity Method .1. Infinite Body Solution. *International Journal for Numerical Methods in Engineering* **10** (2): 301-343.

Crouch, S.L. and Starfield, A.M. 1983. *Boundary Element Methods in Solid Mechanics: With Applications in Rock Mechanics and Geological Engineering*. London: Allen & Unwin.

Detournay, E. and Cheng, A.H.-D. 1993. Fundamentals of Poroelasticity. In *Comprehensive Rock Engineering: Principles, Practice and Projects, Vol. II, Analysis and Design Method*:113–171: Oxford, UK: Pergamon Press.

Detournay, E. and Cheng, A.H.D. 1988. Poroelastic Response of a Borehole in a Non-Hydrostatic Stress Field. *International Journal of Rock Mechanics and Mining Sciences & Geomechanics Abstracts* **25** (3): 171-182.

Detournay, E. and Cheng, A.H.D. 1991. Plane-Strain Analysis of a Stationary Hydraulic Fracture in a Poroelastic Medium. *International Journal of Solids and Structures* **27** (13): 1645-1662.

Detournay, E., Cheng, A.H.D., Roegiers, J.C. et al. 1989. Poroelasticity Considerations in in Situ Stress Determination by Hydraulic Fracturing. *International Journal of Rock Mechanics and Mining Sciences & Geomechanics Abstracts* **26** (6): 507-513.

Dong, C.Y. and de Pater, C.J. 2001. Numerical Implementation of Displacement Discontinuity Method and Its Application in Hydraulic Fracturing. *Computer Methods in Applied Mechanics and Engineering* **191** (8-10): 745-760.

Erdogan, F. and Sih, G.C. 1963. On the Crack Extension in Plates under Plane Loading and Transverse Shear. *Journal of Basic Engineering* **85**: 519-525.

Finnie, I., Cooper, G.A., and Berlie, J. 1979. Fracture Propagation in Rock by Transient Cooling. *International Journal of Rock Mechanics and Mining Sciences* **16** (1): 11-21.

Geertsma, J. 1966. Problems of Rock Mechanics in Petroleum Production Engineering. LNEC (National Laboratory for Civil Engineering) ISRM-1CONGRESS-1966-099. Rijswijk, The Netherlands

Ghassemi, A., Cheng, A.H.D., Diek, A. et al. 2001. A Complete Plane Strain Fictitious Stress Boundary Element Method for Poroelastic Media. *Engineering Analysis with Boundary Elements* **25** (1): 41-48.

Ghassemi, A., Nygren, A., and Cheng, A. 2008. Effects of Heat Extraction on Fracture Aperture: A Poro-Thermoelastic Analysis. *Geothermics* **37** (5): 525-539.

Ghassemi, A., Tarasovs, S., and Cheng, A.H.D. 2007. A 3-D Study of the Effects of Thermomechanical Loads on Fracture Slip in Enhanced Geothermal Reservoirs. *International Journal of Rock Mechanics and Mining Sciences* **44** (8): 1132-1148.

Ghassemi, A. and Zhang, Q. 2004. A Transient Fictitious Stress Boundary Element Method for Porothermoelastic Media. *Engineering Analysis with Boundary Elements* **28** (11): 1363-1373.

Ghassemi, A. and Zhang, Q. 2006. Porothermoelastic Analysis of the Response of a Stationary Crack Using the Displacement Discontinuity Method. *Journal of Engineering Mechanics-Asce* **132** (1): 26-33.

Ghassemi, A. and Zhou, X. 2011. A Three-Dimensional Thermo-Poroelastic Model for Fracture Response to Injection/Extraction in Enhanced Geothermal Systems. *Geothermics* **40** (1): 39-49.

Guéguen, Y. and Boutéca, M. 2004. *Mechanics of Fluid Saturated Rocks*. International Geophysics Series. Amsterdam: Elsevier Academic Press.

Guo, Q., Ji, L., Rajabov, V. et al. 2012. Marcellus and Haynesville Drilling Data: Analysis and Lessons Learned. Paper presented at the SPE Asia Pacific Oil and Gas Conference and Exhibition, Perth, Australia. SPE-158894-MS.

Hopkins, T.W. 1986. Microfracturing in Westerly Granite Experimentally Extended Wet and Dry at Temperatures to 800°C and Pressures to 200 Mpa. MS thesis, Texas A&M University,College Station,Texas.

Huang, N.C. and Russell, S.G. 1985. Hydraulic Fracturing of a Saturated Porous Medium-I: General Theory. *Theoretical and Applied Fracture Mechanics* **4** (3): 201-213.

Irwin, G.R. 1957. Analysis of Stresses and Strains near the End of a Crack Traversing a Plate. *Journal of Applied Mechanics* **24**: 361-364.

Jaeger, J.C., Cook, N.G.W., and Zimmerman, R.W. 2007. *Fundamentals of Rock Mechanics*. Malden, MA: Blackwell Pub.

John, R., Hartman, G.A., and Gallagher, J.P. 1992. Crack-Growth Induced by Thermal-Mechanical Loading. *Experimental Mechanics* **32** (2): 102-108.

McKinney, K.R., Wu, C.C., and Rice, R.W. 2008. Toughness, Crack Propagation, and Size Effect on Strength of Westerly Granite. In *Proceedings of the 9th Annual Conference on Composites and Advanced Ceramic Materials: Ceramic Engineering and Science Proceedings*: John Wiley & Sons, Inc.

McTigue, D.F. 1986. Thermoelastic Response of Fluid-Saturated Porous Rock. *Journal of Geophysical Research-Solid Earth and Planets* **91** (B9): 9533-9542.

Mullen, M.J., Roundtree, R., and Turk, G.A. 2007. A Composite Determination of Mechanical Rock Properties for Stimulation Design (What to Do When You Don'T Have a Sonic Log). Paper presented at the Rocky Mountain Oil & Gas Technology Symposium, Denver, Colorado, U.S.A. SPE-108139-MS.

Nemat-Nasser, S., Keer, L.M., and Parihar, K.S. 1978. Unstable Growth of Thermally Induced Interacting Cracks in Brittle Solids. *International Journal of Solids and Structures* **14** (6): 409-430.

Norris, A. 1992. On the Correspondence between Poroelasticity and Thermoelasticity. *Journal of Applied Physics* **71** (3): 1138-1141.

Nowacki, W. 1962. *Thermoelasticity*. International Series of Monographs on Aeronautics and Astronautics Division 1: Solid and Structural Mechanics,. Reading, Mass.,: Addison-Wesley Pub. Co.

Nuismer, R.J. 1975. Energy-Release Rate Criterion for Mixed Mode Fracture. *International Journal of Fracture* **11** (2): 245-250.

Palciauskas, V.V. and Domenico, P.A. 1982. Characterization of Drained and Undrained Response of Thermally Loaded Repository Rocks. *Water Resources Research* **18** (2): 281-290.

Parker, M.A., Buller, D., Petre, J.E. et al. 2009. Haynesville Shale-Petrophysical Evaluation. Paper presented at the SPE Rocky Mountain Petroleum Technology Conference, Denver, Colorado. SPE-122937-MS.

Perkins, T.K. and Gonzalez, J.A. 1985. The Effect of Thermoelastic Stresses on Injection Well Fracturing. *Society of Petroleum Engineers Journal* **25** (1): 78-88.

Rice, J.R. and Cleary, M.P. 1976. Some Basic Stress Diffusion Solutions for Fluid-Saturated Elastic Porous-Media with Compressible Constituents. *Reviews of Geophysics* **14** (2): 227-241.

Rickman, R., Mullen, M.J., Petre, J.E. et al. 2008. A Practical Use of Shale Petrophysics for Stimulation Design Optimization: All Shale Plays Are Not Clones of the Barnett Shale. Paper presented at the SPE Annual Technical Conference and Exhibition, Denver, Colorado, USA. SPE-115258-MS.

Ruina, A. 1978. Influence of Coupled Deformation-Diffusion Effects on the Retardation of Hydraulic Fracture. Permission to Distribute - American Rock Mechanics Association ARMA-78-0334.

Selvadurai, A.P.S. and Mahyari, A.T. 1998. Computational Modelling of Steady Crack Extension in Poroelastic Media. *International Journal of Solids and Structures* **35** (34–35): 4869-4885.

Shou, K.J. and Crouch, S.L. 1995. A Higher-Order Displacement Discontinuity Method for Analysis of Crack Problems. *International Journal of Rock Mechanics and Mining Sciences & Geomechanics Abstracts* **32** (1): 49-55.

Sih, G.C. 1962. On the Singular Character of Thermal Stresses near a Crack Tip. *Journal of Applied Mechanics* **29** (3): 587-589.

Sneddon, I.N. 1946. The Distribution of Stress in the Neighbourhood of a Crack in an Elastic Solid. *Proceedings of the Royal Society of London Series a-Mathematical and Physical Sciences* **187** (1009): 229-260.

Stehfest, H. 1970. Numerical Inversion of Laplace Transforms. *Communications of the Acm* **13** (1): 47-49.

Stephens, G. and Voight, B. 1982. Hydraulic Fracturing Theory for Conditions of Thermal-Stress. *International Journal of Rock Mechanics and Mining Sciences* **19** (6): 279-284.

Stone, T.J. and Babuska, I. 1998. A Numerical Method with a Posteriori Error Estimation for Determining the Path Taken by a Propagating Crack. *Computer Methods in Applied Mechanics and Engineering* **160** (3-4): 245-271.

Tao, Q. 2010. Numerical Modeling of Fracture Permeability Change in Naturally Fractured Reservoirs Using a Fully Coupled Displacement Discontinuity Method. PhD dissertation, Texas A&M University,College Station,Texas.

Tao, Q. and Ghassemi, A. 2007. Porothermoelastic Analysis of Wellbore Failure and Determination of in Situ Stress and Rock Strength. *Rock Mechanics: Meeting Society's Challenges and Demands, Vols 1 and 2*: 1657-1664.

Tao, Q.F. and Ghassemi, A. 2010. Poro-Thermoelastic Borehole Stress Analysis for Determination of the in Situ Stress and Rock Strength. *Geothermics* **39** (3): 250-259.

Tao, Q.F., Ghassemi, A., and Ehlig-Economides, C.A. 2011. A Fully Coupled Method to Model Fracture Permeability Change in Naturally Fractured Reservoirs. *International Journal of Rock Mechanics and Mining Sciences* **48** (2): 259-268.

Tarasovs, S. and Ghassemi, A. 2010. A Study of Propagation of Cooled Cracks in a Geothermal Reservoir. In *Geothermal Resources Council*, 34:463-466. Sacramento, California ,USA.

Wang, H. 2000. *Theory of Linear Poroelasticity with Applications to Geomechanics and Hydrogeology*. Princeton Series in Geophysics. Princeton, N.J.: Princeton University Press.

Wang, J.L., Papamichos, E., and Dusseault, M.B. 1996. Thermal Stresses and Borehole Stability. *Rock Mechanics Tools and Techniques, Vols 1 and 2*: 1121-1126.

Yan, X.Q. 2004. A Special Crack Tip Displacement Discontinuity Element. *Mechanics Research Communications* **31** (6): 651-659.

Zhang, Q. 2004. A Boundary Element Method for Thermo-Poroelasticity with Applications in Rock Mechanics. MS thesis, University of North Dakota, Grand Forks, North Dakota.

Zhou, X.X. and Ghassemi, A. 2011. Three-Dimensional Poroelastic Analysis of a Pressurized Natural Fracture. *International Journal of Rock Mechanics and Mining Sciences* **48** (4): 527-534.

Zimmerman, R.W. 2000. Coupling in Poroelasticity and Thermoelasticity. *International Journal of Rock Mechanics and Mining Sciences* **37** (1-2): 79-87.

APPENDIX A

THE ELASTIC CRACK TIP DISPLACEMENT DISCONTINUITY ELEMENT FORMULATION

The arbitrary shape of differential displacement discontinuity element is depicted in Figure A.1. The total length of the element is $2a$ and the differential element has normal and shear differential displacement discontinuities, $D_x(\xi)$ and $D_y(\xi)$, respectively.

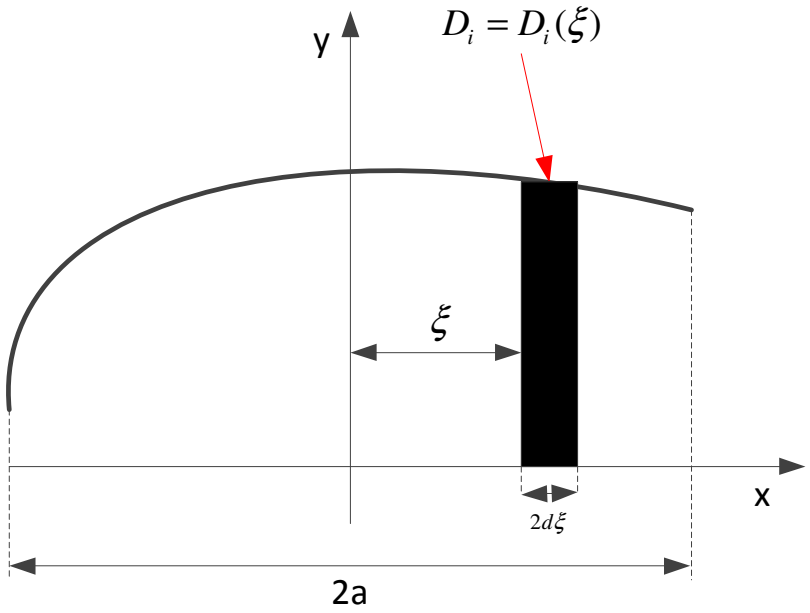

Figure A.1 The arbitrary shape of differential displacement discontinuity element

From the differential point of view, we can obtain a differential element formulation by modifying the shape function of the constant displacement discontinuity formulation (Crouch 1976; Yan 2004).

For the displacements:

$$du_x = D_x(\xi)\left[2(1-\nu)V_3(x,y,\xi) - yV_5(x,y,\xi)\right] + D_y(\xi)\left[-(1-2\nu)V_2(x,y,\xi) - yV_4(x,y,\xi)\right]$$
$$du_y = D_x(\xi)\left[(1-2\nu)V_2(x,y,\xi) - yV_4(x,y,\xi)\right] + D_y(\xi)\left[2(1-\nu)V_3(x,y,\xi) - yV_5(x,y,\xi)\right] \quad \text{..... (A.1)}$$

For the stresses:

$$\begin{aligned} d\sigma_{xx} &= 2GD_x(\xi)\left[2V_4(x,y,\xi) + yV_6(x,y,\xi)\right] + \\ &\quad 2GD_y(\xi)\left[-V_5(x,y,\xi) + yV_7(x,y,\xi)\right] \\ d\sigma_{yy} &= 2GD_x(\xi)\left[-yV_6(x,y,\xi)\right] + 2GD_y(\xi)\left[-V_5(x,y,\xi) - yV_7(x,y,\xi)\right] \\ d\sigma_{xy} &= 2GD_x(\xi)\left[-V_5(x,y,\xi) + yV_7(x,y,\xi)\right] + 2GD_y(\xi)\left[-yV_6(x,y,\xi)\right] \end{aligned} \quad \text{..... (A.2)}$$

where functions $V_i(x,y,\xi)$ in these equations are given by

$$V_2(x,y,\xi) = -\frac{1}{4\pi(1-\nu)}\frac{x-\xi}{(x-\xi)^2+y^2}$$
$$V_3(x,y,\xi) = -\frac{1}{4\pi(1-\nu)}\frac{y}{(x-\xi)^2+y^2}$$
$$V_4(x,y,\xi) = \frac{2y}{4\pi(1-\nu)}\frac{x-\xi}{\left\{(x-\xi)^2+y^2\right\}^2}$$
$$V_5(x,y,\xi) = \frac{1}{4\pi(1-\nu)}\frac{(x-\xi)^2-y^2}{\left\{(x-\xi)^2+y^2\right\}^2}$$
$$V_6(x,y,\xi) = \frac{2}{4\pi(1-\nu)}\left\{\frac{(x-\xi)^3}{\left\{(x-\xi)^2+y^2\right\}^3} - \frac{3(x-\xi)y^2}{\left\{(x-\xi)^2+y^2\right\}^3}\right\}$$
$$V_7(x,y,\xi) = \frac{2y}{4\pi(1-\nu)}\left\{\frac{3(x-\xi)^2}{\left\{(x-\xi)^2+y^2\right\}^3} - \frac{y^2}{\left\{(x-\xi)^2+y^2\right\}^3}\right\} \quad \text{..... (A.3)}$$

Then integrating the above differential formulation over the element with length $2a$ yields

$$U_{ij}(x,y)=\int_{-a}^{a} D_j(\xi)V_i(x,y,\xi)d\xi \quad (i=2,3,...,7;\ j=1,2) \qquad \text{(A.4)}$$

Then the displacements and stresses at any random point in the body can be formulated as

$$\begin{aligned} u_x &= \left[2(1-\nu)U_{3x}(x,y)-yU_{5x}(x,y)\right]+\left[-(1-2\nu)U_{2y}(x,y)-yU_{4y}(x,y)\right] \\ u_y &= \left[(1-2\nu)U_{2x}(x,y)-yU_{4x}(x,y)\right]+\left[2(1-\nu)U_{3y}(x,y)-yU_{5y}(x,y)\right] \end{aligned} \qquad \text{(A.5)}$$

$$\begin{aligned} \sigma_{xx} &= 2G\left[2U_{4x}(x,y)+yU_{6x}(x,y)\right]+2G\left[-U_{5y}(x,y)+yU_{7y}(x,y)\right] \\ \sigma_{yy} &= 2G\left[-yU_{6x}(x,y)\right]+2G\left[-U_{5y}(x,y)-yU_{7y}(x,y)\right] \\ \sigma_{xy} &= 2G\left[-U_{5x}(x,y)+yU_{7x}(x,y)\right]+2G\left[-yU_{6y}(x,y)\right] \end{aligned} \qquad \text{(A.6)}$$

These formulae are the fundamental ones required to set up the crack tip element implementation.

The special crack tip displacement discontinuity element at the left tip of the crack is depicted in Figure A.2. The displacement discontinuity functions at the left tip are expressed in terms of constant displacement discontinuity (H_i) (Yan 2004):

$$\begin{aligned} D_x &= H_s\left(\frac{a+\xi}{a}\right)^{0.5} \\ D_y &= H_n\left(\frac{a+\xi}{a}\right)^{0.5} \end{aligned} \qquad \text{(A.7)}$$

where H_s and H_n are the tangential and normal displacement discontinuities at the center of the special crack tip element, respectively.

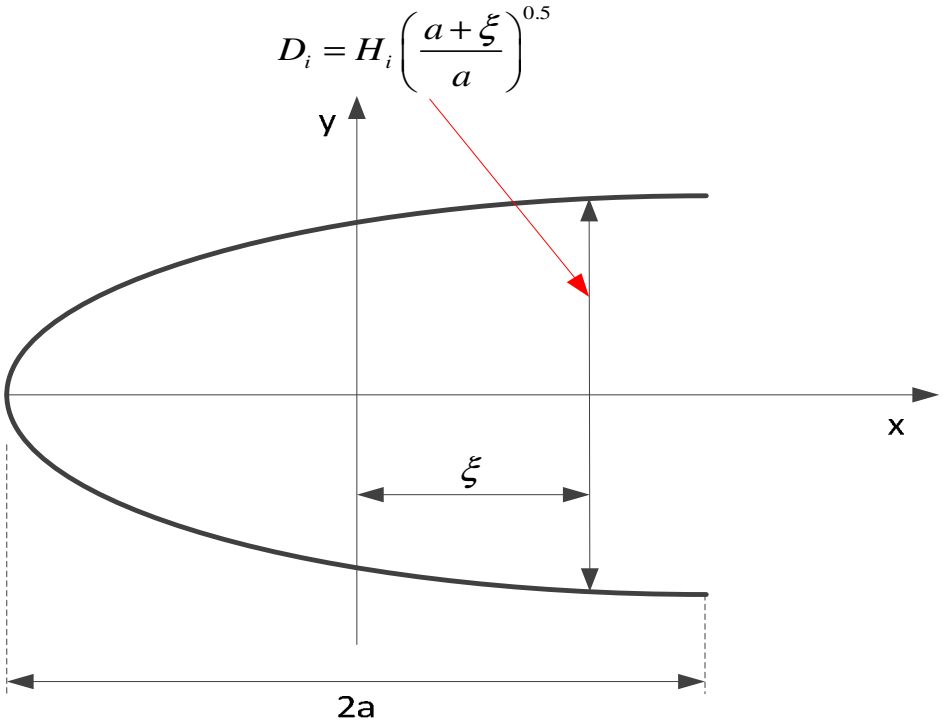

Figure A.2 The special elastic DD element shape at the left crack tip (Yan 2004)

Substituting Eq. A.7 into A.4, the formulation is

$$U_{ij}(x,y) = H_j \int_{-a}^{a} \left(\frac{a+\xi}{a} \right)^{0.5} V_i(x,y,\xi) d\xi = H_j B_i(x,y) \quad (i = 2,3,...,7;\ j = 1,2) \quad \text{..... (A.8)}$$

where functions $V_i(x,y,\xi)$ in these equations are given by

$$B_i(x,y) = \int_{-a}^{a} \left(\frac{a+\xi}{a} \right)^{0.5} V_i(x,y,\xi) d\xi \quad (i = 2,3,...,7) \quad \text{..... (A.9)}$$

Substituting Eq. A.8 into A.5 and A.6, the formulation is

$$\begin{aligned} u_x &= H_s \left[2(1-\nu) B_3(x,y) - y B_5(x,y) \right] + H_n \left[-(1-2\nu) B_2(x,y) - y B_4(x,y) \right] \\ u_y &= H_s \left[(1-2\nu) B_2(x,y) - y B_4(x,y) \right] + H_n \left[2(1-\nu) B_3(x,y) - y B_5(x,y) \right] \end{aligned} \quad \text{.....(A.10)}$$

$$\sigma_{xx} = 2GH_s\left[2B_4(x,y) + yB_6(x,y)\right] + 2GH_n\left[-B_5(x,y) + yB_7(x,y)\right]$$
$$\sigma_{yy} = 2GH_s\left[-yB_6(x,y)\right] + 2GH_n\left[-B_5(x,y) - yB_7(x,y)\right] \quad \text{.....(A.11)}$$
$$\sigma_{xy} = 2GH_s\left[-B_5(x,y) + yB_7(x,y)\right] + 2GH_n\left[-yB_6(x,y)\right]$$

The shape function of B_i $(i = 2,3,...,7)$ can be calculated as followings (Yan 2004).

(1) For an arbitrary point in the domain $P(x,y)(y \neq 0)$

$B_i(x,y)$ functions are solved by Gauss numerical integration.

$$\xi = at \quad \text{.....(A.12)}$$

Then,

$$B_i(x,y) = \int_{-a}^{a}\left(\frac{a+\xi}{a}\right)^{1/2} V_i(x,y,\xi)d\xi = a\int_{-1}^{1} V_i(x,y,at)(1+t)^{1/2}dt \quad (i = 2,3,...,7) \quad \text{.....(A.13)}$$

Therefore, $B_i(x,y)$ can be given as

$$B_i(x,y) = a\sum_j V_i(x,y,a\zeta_j)(1+\zeta_j)^{1/2} w_j \quad (i = 2,3,...,7) \quad \text{.....(A.14)}$$

where ζ_j and w_j are the Gaussian point coordinates and corresponding weight factors, respectively.

(2) For an arbitrary point in the domain $P(x,y)(y = 0)$

$B_i(x,y)$ functions are solved analytically.

For $x > -a$,

$$B_2(x,0) = -\frac{1}{4\pi(1-\nu)}\left\{-2\sqrt{2} + \sqrt{\frac{x+a}{a}}\ln\left|\frac{\sqrt{x+a}+\sqrt{2a}}{\sqrt{x+a}-\sqrt{2a}}\right|\right\}$$

$$B_4(x,0) = 0$$

$$B_5(x,0) = \frac{1}{4\pi(1-\nu)}\left\{\frac{\sqrt{2}}{x-a} - \frac{1}{2\sqrt{a(x+a)}}\ln\left|\frac{\sqrt{x+a}+\sqrt{2a}}{\sqrt{x+a}-\sqrt{2a}}\right|\right\} \quad \text{.....(A.15)}$$

$$B_6(x,0) = \frac{1}{4\pi(1-\nu)}\left\{\frac{\sqrt{2}}{(x-a)^2} - \frac{\sqrt{2}}{2(x^2-a^2)} - \frac{1}{4\sqrt{a}(x+a)^{1.5}}\ln\left|\frac{\sqrt{x+a}+\sqrt{2a}}{\sqrt{x+a}-\sqrt{2a}}\right|\right\}$$

$$B_7(x,0) = 0$$

For $x < -a$, define $r = |x| - a$

$$B_2(x,0) = -\frac{1}{4\pi(1-\nu)}\left\{-2\sqrt{2} + 2\sqrt{\frac{r}{a}}\arctan\sqrt{\frac{2a}{r}}\right\}$$

$$B_4(x,0) = 0$$

$$B_5(x,0) = \frac{1}{4\pi(1-\nu)}\left\{-\frac{\sqrt{2}}{r+2a} + \frac{1}{\sqrt{ar}}\arctan\sqrt{\frac{2a}{r}}\right\} \quad \text{.....(A.16)}$$

$$B_6(x,0) = \frac{1}{4\pi(1-\nu)}\left\{\frac{\sqrt{2}}{(r+2a)^2} - \frac{\sqrt{2}}{2r(r+2a)} - \frac{1}{2\sqrt{a}r^{1.5}}\arctan\sqrt{\frac{2a}{r}}\right\}$$

$$B_7(x,0) = 0$$

(3) For an arbitrary point in the domain $P(x,y)(y=0)$, the

$B_3(x,0)$ function is solved analytically.

$$B_3(x,0) = \begin{cases} 0 & |x| > a \\ \dfrac{1}{4(1-\nu)}, & y = 0_+, |x| < a \\ -\dfrac{1}{4(1-\nu)}, & y = 0_-, |x| < a \end{cases} \quad \text{.....(A.17)}$$

(4) For a point in the domain $P(0,0)$

$$B_2(0,0) = -\frac{1}{4\pi(1-\nu)}\left\{-2\sqrt{2} + \ln\left|\frac{1+\sqrt{2}}{1-\sqrt{2}}\right|\right\}$$

$$B_3(0,0) = \begin{cases} \dfrac{1}{4(1-\nu)}, & y = 0_+ \\ -\dfrac{1}{4(1-\nu)}, & y = 0_- \end{cases}$$

$$B_4(0,0) = 0 \qquad \text{.....(A.18)}$$

$$B_5(0,0) = \frac{1}{4\pi(1-\nu)}\left\{-\sqrt{2} - \frac{1}{2}\ln\left|\frac{1+\sqrt{2}}{1-\sqrt{2}}\right|\right\} \Big/ a$$

$$B_6(0,0) = \frac{1}{4\pi(1-\nu)}\left\{-\frac{3\sqrt{2}}{2} - \frac{1}{4}\ln\left|\frac{1+\sqrt{2}}{1-\sqrt{2}}\right|\right\} \Big/ a^2$$

$$B_7(0,0) = 0$$

APPENDIX B

THE POROELASTIC CRACK TIP DISPLACEMENT DISCONTINUITY ELEMENT FORMULATION

The fundamental solution for induced stresses in poroelastic media with constant displacement discontinuities on the fracture segments can be written as (Carvalho 1990):

$$
\begin{aligned}
\left(\sigma_{ijkn}\right) = \frac{G}{2\pi(1-\nu)}\frac{1}{r^2}\Bigg\{ & \left(\delta_{in}\delta_{jk}+\delta_{ik}\delta_{jn}\right)\left[1+\frac{\nu_u-\nu}{1-\nu_u}\left[1+2e^{-\zeta^2}\frac{3}{\zeta^2}\left(1-e^{-\zeta^2}\right)\right]\right] \\
& -\delta_{ij}\delta_{kn}\left[1+\frac{\nu_u-\nu}{1-\nu_u}\left[1+8e^{-\zeta^2}-\frac{9}{\zeta^2}\left(1-e^{-\zeta^2}\right)+4\zeta^2e^{-\zeta^2}\right]\right] \\
& +\frac{2}{r^2}\left(\delta_{ij}x_kx_n+\delta_{kn}x_ix_j\right)\left[1+\frac{\nu_u-\nu}{1-\nu_u}\left[1+5e^{-\zeta^2}+2\zeta^2e^{-\zeta^2}-\frac{6}{\zeta^2}\left(1-e^{-\zeta^2}\right)\right]\right] \quad \text{..... (B.1)} \\
& -\frac{8x_ix_jx_kx_n}{r^4}\left[1+\frac{\nu_u-\nu}{1-\nu_u}\left[1+2e^{-\zeta^2}-\frac{3}{\zeta^2}\left(1-e^{-\zeta^2}\right)+\frac{\zeta^2}{2}e^{-\zeta^2}\right]\right]\Bigg\}
\end{aligned}
$$

where $r^2 = x^2 + y^2$, and $\zeta^2 = \dfrac{r^2}{4c_f t}$.

This equation basically contains both elastic and poroelastic parts. The basic concept is simple. The elastic part has already been developed in Appendix A. So what we need to do is just adding poroelastic part into the elastic one.

From the differential point of view, we can obtain a differential poroelastic element formulation by modifying Eq. A.2 in Appendix A.

$$
\begin{aligned}
d\sigma_{xx}^{\text{poro}} &= D_x(\xi)\left\{\left[4GV_4(x,y,\xi)+2GyV_6(x,y,\xi)\right]+d\sigma_{xx}^{ds}\right\}+ \\
&\quad D_y(\xi)\left\{\left[-2GV_5(x,y,\xi)+2GyV_7(x,y,\xi)\right]+d\sigma_{xx}^{dn}\right\} \\
d\sigma_{yy}^{\text{poro}} &= D_x(\xi)\left[-2GyV_6(x,y,\xi)+d\sigma_{yy}^{ds}\right]+ \\
&\quad D_y(\xi)\left[-2GV_5(x,y,\xi)-2GyV_7(x,y,\xi)+d\sigma_{yy}^{dn}\right] \\
d\sigma_{xy}^{\text{poro}} &= D_x(\xi)\left[-2GV_5(x,y,\xi)+2GyV_7(x,y,\xi)+d\sigma_{xy}^{ds}\right]+ \\
&\quad D_y(\xi)\left[-2GyV_6(x,y,\xi)+d\sigma_{xy}^{dn}\right]
\end{aligned}
\qquad \text{..... (B.2)}
$$

where the poroelastic stress components in these equations are given by

For stress ($d\sigma_{xx}$) due to continuous shear displacement discontinuity source:

$$
\begin{aligned}
d\sigma_{xx}^{ds} &= \frac{G}{2\pi(1-\nu)}\left(\frac{\nu_u-\nu}{1-\nu_u}\right)\frac{1}{(x-\xi)^2+y^2}\times \\
&\left(\left(-\frac{12(x-\xi)y}{(x-\xi)^2+y^2}+\frac{24(x-\xi)^3y}{\left\{(x-\xi)^2+y^2\right\}^2}\right)\frac{1-e^{-\zeta^2}}{\zeta^2}+2\left(\frac{5(x-\xi)y}{(x-\xi)^2+y^2}-\frac{8(x-\xi)^3y}{\left\{(x-\xi)^2+y^2\right\}^2}\right)e^{-\zeta^2}+\right. \\
&\left.4\left(\frac{(x-\xi)y}{(x-\xi)^2+y^2}-\frac{(x-\xi)^3y}{\left\{(x-\xi)^2+y^2\right\}^2}\right)\zeta^2e^{-\zeta^2}\right)
\end{aligned}
$$

.....(B.3)

For stress ($d\sigma_{xx}$) due to continuous normal displacement discontinuity source:

$$
\begin{aligned}
d\sigma_{xx}^{dn} &= \frac{G}{2\pi(1-\nu)}\left(\frac{\nu_u-\nu}{1-\nu_u}\right)\frac{1}{(x-\xi)^2+y^2}\times \\
&\left(\left(-3+\frac{24(x-\xi)^2y^2}{\left\{(x-\xi)^2+y^2\right\}^2}\right)\frac{1-e^{-\zeta^2}}{\zeta^2}+2\left(1-\frac{8(x-\xi)^2y^2}{\left\{(x-\xi)^2+y^2\right\}^2}\right)e^{-\zeta^2}-\frac{4(x-\xi)^2y^2}{\left\{(x-\xi)^2+y^2\right\}^2}\zeta^2e^{-\zeta^2}\right)
\end{aligned}
$$

.....(B.4)

For stress ($d\sigma_{yy}$) due to continuous shear displacement discontinuity source:

$$d\sigma_{yy}^{ds} = \frac{G}{2\pi(1-\nu)}\left(\frac{\nu_u-\nu}{1-\nu_u}\right)\frac{1}{(x-\xi)^2+y^2}\times$$
$$\left(\left(-\frac{12(x-\xi)y}{(x-\xi)^2+y^2}+\frac{24(x-\xi)y^3}{\left\{(x-\xi)^2+y^2\right\}^2}\right)\frac{1-e^{-\zeta^2}}{\zeta^2}+2\left(\frac{5(x-\xi)y}{(x-\xi)^2+y^2}-\frac{8(x-\xi)y^3}{\left\{(x-\xi)^2+y^2\right\}^2}\right)e^{-\zeta^2}+\right.$$
$$\left.4\left(\frac{(x-\xi)y}{(x-\xi)^2+y^2}-\frac{(x-\xi)y^3}{\left\{(x-\xi)^2+y^2\right\}^2}\right)\zeta^2 e^{-\zeta^2}\right)$$

.....(B.5)

For stress ($d\sigma_{yy}$) due to continuous normal displacement discontinuity source:

$$d\sigma_{yy}^{dn} = \frac{G}{2\pi(1-\nu)}\left(\frac{\nu_u-\nu}{1-\nu_u}\right)\frac{1}{(x-\xi)^2+y^2}\times$$
$$\left(\left(\frac{24y^2}{(x-\xi)^2+y^2}-3-\frac{24y^4}{\left\{(x-\xi)^2+y^2\right\}^2}\right)\frac{1-e^{-\zeta^2}}{\zeta^2}+2\left(2-\frac{10y^2}{(x-\xi)^2+y^2}+\frac{8y^4}{\left\{(x-\xi)^2+y^2\right\}^2}\right)e^{-\zeta^2}+\right.$$
$$\left.4\left(1-\frac{2y^2}{(x-\xi)^2+y^2}+\frac{y^4}{\left\{(x-\xi)^2+y^2\right\}^2}\right)\zeta^2 e^{-\zeta^2}\right)$$

.....(B.6)

For stress ($d\sigma_{xy}$) due to continuous shear displacement discontinuity source:

$$d\sigma_{xy}^{ds} = \frac{G}{2\pi(1-\nu)}\left(\frac{\nu_u-\nu}{1-\nu_u}\right)\frac{1}{(x-\xi)^2+y^2}\times$$
$$\left(\left(-3+\frac{24(x-\xi)^2y^2}{\left\{(x-\xi)^2+y^2\right\}^2}\right)\frac{1-e^{-\zeta^2}}{\zeta^2}+2\left(1-\frac{8(x-\xi)^2y^2}{\left\{(x-\xi)^2+y^2\right\}^2}\right)e^{-\zeta^2}-\frac{4(x-\xi)^2y^2}{\left\{(x-\xi)^2+y^2\right\}^2}\zeta^2e^{-\zeta^2}\right)$$

.....(B.7)

For stress ($d\sigma_{xy}$) due to continuous normal displacement discontinuity source:

$$d\sigma_{xy}^{dn} = \frac{G}{2\pi(1-\nu)}\left(\frac{\nu_u-\nu}{1-\nu_u}\right)\frac{1}{(x-\xi)^2+y^2}\times$$
$$\left(\left(-\frac{12(x-\xi)y}{(x-\xi)^2+y^2}+\frac{24(x-\xi)y^3}{\left\{(x-\xi)^2+y^2\right\}^2}\right)\frac{1-e^{-\zeta^2}}{\zeta^2}+2\left(\frac{5(x-\xi)y}{(x-\xi)^2+y^2}-\frac{8(x-\xi)y^3}{\left\{(x-\xi)^2+y^2\right\}^2}\right)e^{-\zeta^2}+\right.$$
$$\left.4\left(\frac{(x-\xi)y}{(x-\xi)^2+y^2}-\frac{(x-\xi)y^3}{\left\{(x-\xi)^2+y^2\right\}^2}\right)\zeta^2e^{-\zeta^2}\right)$$

.....(B.8)

where $\zeta^2=\dfrac{(x-\xi)^2+y^2}{4c_ft}$, c_f is fluid diffusivity, and t is time.

The shape function of $B_i(x,y)^{\text{poro}}$ can be calculated as followings

(1) For an arbitrary point in the domain $P(x,y)(y\neq 0)$

$B_i(x,y)^{\text{poro}}$ functions are solved by Gauss numerical integration.

$$\xi = at \quad \text{..... (B.9)}$$

Then,

$$B_{ij}(x,y)^{\text{poro}} = \int_{-a}^{a} \left(\frac{a+\xi}{a} \right)^{1/2} \sigma_{ij}(x,y,\xi)^{\text{poro}} d\xi \quad (i,j=1,2)$$
$$= a\int_{-1}^{1} \sigma_{ij}(x,y,at)^{\text{poro}} (1+t)^{1/2} dt \quad (i,j=1,2) \quad \text{.....(B.10)}$$

Therefore, $B_i(x,y)^{\text{poro}}$ can be given as

$$B_i(x,y) = a\sum_j \sigma_{ij}(x,y,a\zeta_j)^{\text{poro}} (1+\zeta_j)^{1/2} w_j \quad \text{.....(B.11)}$$

where ζ_j and w_j are the Gaussian point coordinates and corresponding weight factors, respectively.

(2) For an arbitrary point in the domain $P(x,y)(y=0)$

$B_i(x,y)^{\text{poro}}$ functions are solved by Gauss numerical integration.

But $\sigma_{ij}(x,y,\xi)^{\text{poro}}$ functions are taken by limitation $y \to 0$ before taking Gauss numerical integration.

$$\lim_{y\to 0} \sigma_i(x,y) \quad \text{.....(B.12)}$$

(3) For an arbitrary point in the domain $P(x,y)(y=0)$,

$B_i(x,y)^{\text{poro}}$ functions are solved by Gauss numerical integration.

But $\sigma_{ij}(x,y,\xi)^{\text{poro}}$ functions are taken by limitation $x, y \to 0$ before taking Gauss numerical integration.

$$\lim_{x,y\to 0} \sigma_i(x,y) \quad \text{.....(B.13)}$$

APPENDIX C

TIME-MARCHING SCHEME USED FOR THERMO-POROELASTIC FUNDAMENTAL SOLUTION FOR A NON-STATIONARY CRACK (PROPAGATION)

The time-marching scheme for crack propagation is more complicated than that for the stationary crack problem because we have to not only keep track of the variations of temperature and pore pressure changing in time but also take into account the updated new elements as the crack propagates.

In this section, we first present basic steps for crack growth simulation within the scope of linear elastic fracture mechanics in detail. Then we describe how to keep track of the variations of stresses, temperature, and pore pressure in time during multi-stage fracture propagation.

The numerical analysis of crack propagation is generally based upon incremental extensions of the crack. In this work, we assumed the crack extension path is determined by the stress intensity factor, which must be calculated in each time step, and the maximum number of crack growth iterations in one time step is 3.

Crack propagation simulation involves for which the following procedures must be performed step by step:

1. Thermo-poroelastic boundary element analysis

2. Computation of stress intensity factors at the crack tip

3. Determination of crack growth direction (θ_c)

4. Determination of crack growth extension (Δa)

5. Determination of new crack tip coordinate, and updating boundary condition

6. Back to step 1

The first and second steps have already been discussed in detail in previous sections. The third step is based on the maximum principal stress criterion using Eq. C.1 described in section 4.5.

$$\theta_c = 2\arctan\frac{1}{4}\left(\frac{K_{\mathrm{I}}}{K_{\mathrm{II}}} - \mathrm{sgn}(K_{\mathrm{II}})\sqrt{\left(\frac{K_{\mathrm{I}}}{K_{\mathrm{II}}}\right)^2 + 8}\right) \quad \text{(C.1)}$$

For the fourth step, we assume the increment (Δa) of new crack do not change with time, keeping constant size as a size of the previous crack segments. The position of the corresponding point l' in the new crack tip can be obtained from the position of point l in the previous tip as (Figure C.1):

$$\mathbf{r}^{l'} = \mathbf{r}^{l} + \Delta a\left[\cos(\theta_c), \sin(\theta_c)\right] \quad \text{(C.2)}$$

where $\mathbf{r}^{l'}$ and $\mathbf{r}^{l}$ are the position vectors of point l' and l respectively.

Once the new crack front position is determined, new elements are added, connecting the new crack front to the previous element as long as crack extension criterion is met.

After that, the boundary conditions of this model need to be updated in order that new boundary conditions are applied at the crack faces.

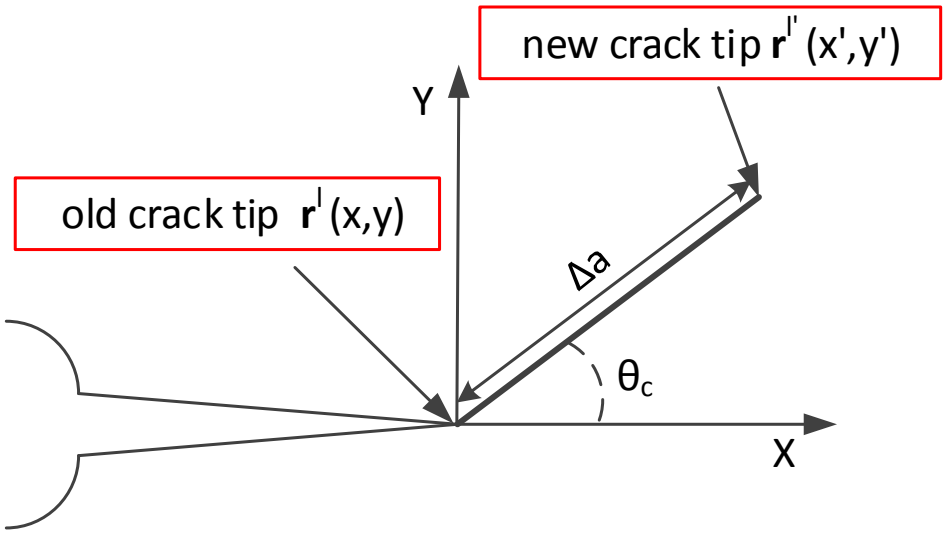

Figure C.1 Discrete representation of extended crack segments

Figure C.2 shows a connected set of straight-line segments. As mentioned, in this case, the maximum number of crack growth iterations in one time step is 3.

The normal and shear displacement discontinuities, fluid flux, and heat flux on the N number of fracture segments are known at time t_n, and we assume the crack can start to propagate from one end of those segments at t_{n+1}. In this case, the solution

matrix before the fracture propagation at t_n is shown in Eq. C.3. (Temperature and heat flux can be calculated independently) As shown, the solution matrix consists of a system of 3 N linear equations.

$$\begin{pmatrix} {}^{11}A & {}^{11}B & {}^{11}C & \cdots & {}^{1N}A & {}^{1N}B & {}^{1N}C \\ {}^{11}E & {}^{11}F & {}^{11}G & \cdots & {}^{1N}E & {}^{1N}F & {}^{1N}G \\ {}^{11}K & {}^{11}L & {}^{11}M & \cdots & {}^{1N}K & {}^{1N}L & {}^{1N}M \\ \vdots & \vdots & \vdots & \cdots & \vdots & \vdots & \vdots \\ {}^{N1}A & {}^{N1}B & {}^{N1}C & \cdots & {}^{NN}A & {}^{NN}B & {}^{NN}C \\ {}^{N1}E & {}^{N1}F & {}^{N1}G & \cdots & {}^{NN}E & {}^{NN}F & {}^{NN}G \\ {}^{N1}K & {}^{N1}L & {}^{N1}M & \cdots & {}^{NN}K & {}^{NN}L & {}^{NN}M \end{pmatrix} \begin{pmatrix} {}^{1}\Delta D_n \\ {}^{1}\Delta D_s \\ {}^{1}\Delta q_f \\ \vdots \\ {}^{N}\Delta D_n \\ {}^{N}\Delta D_s \\ {}^{N}\Delta q_f \end{pmatrix} = \begin{pmatrix} {}^{1}\sigma_n \\ {}^{1}\sigma_s \\ {}^{1}p \\ \vdots \\ {}^{N}\sigma_n \\ {}^{N}\sigma_s \\ {}^{N}p \end{pmatrix} \quad \text{..... (C.3)}$$

However, once the crack starts to propagate, the influences of the singular sources on the newly updated element (shown in Figure C.2) should be taken into consideration in the system to calculate its influence coefficients to other elements as well as the induced stresses and the pore pressure near the element as the new boundary conditions.

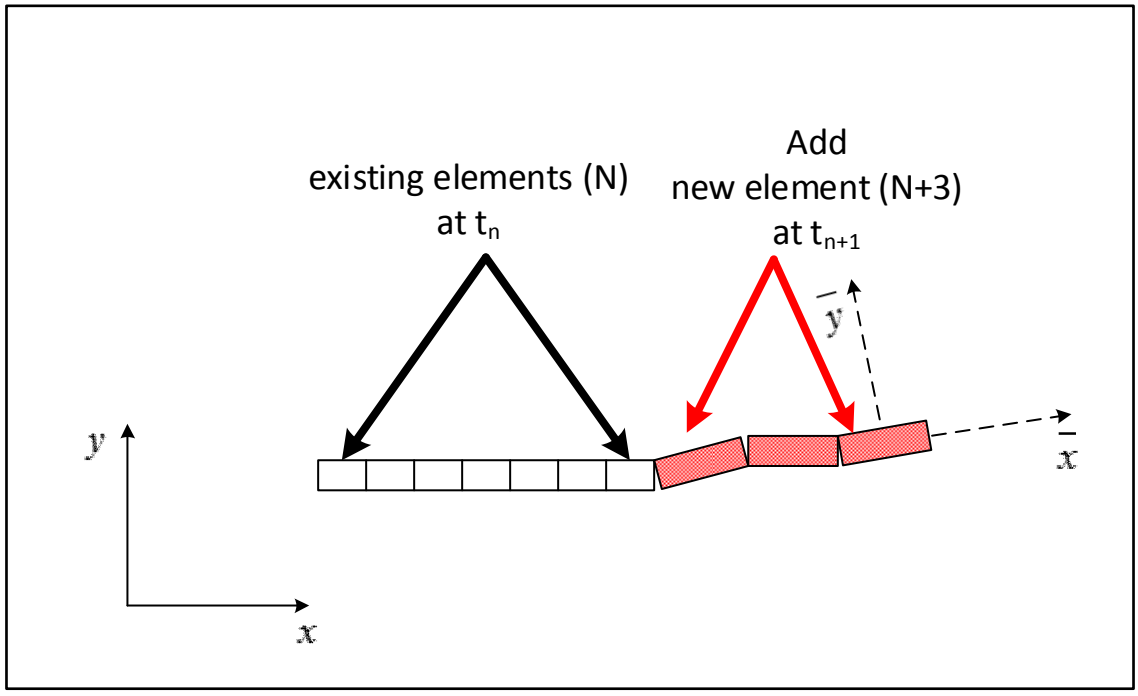

Figure C.2 A schematic illustration of an evolution of a crack geometry

Therefore, the newly updated solution matrix for the crack propagation at time t_{n+1} is shown in Eq. C.4.

$$
\begin{pmatrix}
{}^{11}A & {}^{11}B & {}^{11}C & \cdots & {}^{1N}A & {}^{1N}B & {}^{1N}C & {}^{1(N+3)}A & {}^{1(N+3)}B & {}^{1(N+3)}C \\
{}^{11}E & {}^{11}F & {}^{11}G & \cdots & {}^{1N}E & {}^{1N}F & {}^{1N}G & {}^{1(N+3)}E & {}^{1(N+3)}F & {}^{1(N+3)}G \\
{}^{11}K & {}^{11}L & {}^{11}M & \cdots & {}^{1N}K & {}^{1N}L & {}^{1N}M & {}^{1(N+3)}K & {}^{1(N+3)}L & {}^{1(N+3)}M \\
\vdots & \vdots & \vdots & \cdots & \vdots & \vdots & \vdots & \vdots & \vdots & \vdots \\
{}^{N1}A & {}^{N1}B & {}^{N1}C & \cdots & {}^{NN}A & {}^{NN}B & {}^{NN}C & {}^{N(N+3)}A & {}^{N(N+3)}B & {}^{N(N+3)}C \\
{}^{N1}E & {}^{N1}F & {}^{N1}G & \cdots & {}^{NN}E & {}^{NN}F & {}^{NN}G & {}^{N(N+3)}E & {}^{N(N+3)}F & {}^{N(N+3)}G \\
{}^{N1}K & {}^{N1}L & {}^{N1}M & \cdots & {}^{NN}K & {}^{NN}L & {}^{NN}M & {}^{N(N+3)}K & {}^{N(N+3)}L & {}^{N(N+3)}M \\
{}^{(N+1)1}A & {}^{(N+1)1}B & {}^{(N+3)1}C & \cdots & {}^{(N+3)N}A & {}^{(N+3)N}B & {}^{(N+3)N}C & {}^{(N+3)(N+3)}A & {}^{(N+3)(N+3)}B & {}^{(N+3)(N+3)}C \\
{}^{(N+1)1}E & {}^{(N+1)1}F & {}^{(N+3)1}G & \cdots & {}^{(N+3)N}E & {}^{(N+3)N}F & {}^{(N+3)N}G & {}^{(N+3)(N+3)}E & {}^{(N+3)(N+3)}F & {}^{(N+3)(N+3)}G \\
{}^{(N+1)1}K & {}^{(N+1)1}L & {}^{(N+3)1}M & \cdots & {}^{(N+3)N}K & {}^{(N+3)N}L & {}^{(N+3)N}M & {}^{(N+3)(N+3)}K & {}^{(N+3)(N+3)}L & {}^{(N+3)(N+3)}M
\end{pmatrix}
\begin{pmatrix}
{}^{1}\Delta D_n \\ {}^{1}\Delta D_s \\ {}^{1}\Delta q_f \\ \vdots \\ {}^{N}\Delta D_n \\ {}^{N}\Delta D_s \\ {}^{N}\Delta q_f \\ {}^{N+3}\Delta D_n \\ {}^{N+3}\Delta D_s \\ {}^{N+3}\Delta q_f
\end{pmatrix}
=
\begin{pmatrix}
{}^{1}\sigma_n + ({}^{1}\Delta\sigma_n)_{\text{porothermo}} \\
{}^{1}\sigma_s + ({}^{1}\Delta\sigma_s)_{\text{porothermo}} \\
{}^{1}p + ({}^{1}\Delta p)_{\text{porothermo}} \\
\vdots \\
{}^{N}\sigma_n + ({}^{N}\Delta\sigma_n)_{\text{porothermo}} \\
{}^{N}\sigma_s + ({}^{N}\Delta\sigma_s)_{\text{porothermo}} \\
{}^{N}p + ({}^{N}\Delta p)_{\text{porothermo}} \\
{}^{N+3}\sigma_n + ({}^{N+3}\Delta\sigma_n)_{\text{porothermo}} \\
{}^{N+3}\sigma_s + ({}^{N+3}\Delta\sigma_s)_{\text{porothermo}} \\
{}^{N+3}p + ({}^{N+3}\Delta p)_{\text{porothermo}}
\end{pmatrix}
\quad \text{..... (C.4)}
$$

Then for the newly updated boundary conditions, we do not consider subtracting all previous influences from known boundary conditions at the previous time step because the boundary conditions should be kept during the fracture propagation. Thus only thermally or poro-thermally induced stresses are applied as surface tractions on the fracture surface to simulate crack propagation using the stress superposition principle.

For example, for the normal stress,

$$
\sum_{j=1}^{N} {}^{ij}A(t-\tau_\xi)\Delta\, {}^{j\xi}D_n + \sum_{j=1}^{N} {}^{ij}B(t-\tau_\xi)\Delta\, {}^{j\xi}D_s + \sum_{j=1}^{N} {}^{ij}C(t-\tau_\xi)\Delta\, {}^{j\xi}q_f + \sum_{j=1}^{N} {}^{ij}T(t-\tau_\xi)\Delta\, {}^{j\xi}h_f = \quad \text{..... (C.5)}
$$
$$
{}^{i}\sigma_n(\xi) + ({}^{i}\Delta\sigma_n)_{\text{porothermo}}
$$

For the shear stress,

$$\sum_{j=1}^{N} \overset{ij}{E}(t-\tau_{\xi})\Delta \overset{j\xi}{D}_n + \sum_{j=1}^{N} \overset{ij}{F}(t-\tau_{\xi})\Delta \overset{j\xi}{D}_s + \sum_{j=1}^{N} \overset{ij}{G}(t-\tau_{\xi})\Delta \overset{j\xi}{q}_f + \sum_{j=1}^{N} \overset{ij}{T}(t-\tau_{\xi})\Delta \overset{j\xi}{h}_f = \overset{i}{\sigma}_s(\xi) + (\Delta \overset{i}{\sigma}_s)_{\text{porothermo}} \quad \text{..... (C.6)}$$

For the pore pressure,

$$\sum_{j=1}^{N} \overset{ij}{K}(t-\tau_{\xi})\Delta \overset{j\xi}{D}_n + \sum_{j=1}^{N} \overset{ij}{L}(t-\tau_{\xi})\Delta \overset{j\xi}{D}_s + \sum_{j=1}^{N} \overset{ij}{M}(t-\tau_{\xi})\Delta \overset{j\xi}{q}_f + \sum_{j=1}^{N} \overset{ij}{T}(t-\tau_{\xi})\Delta \overset{j\xi}{h}_f = \overset{i}{p}(\xi) + (\Delta \overset{i}{p})_{\text{porothermo}} \quad \text{..... (C.7)}$$

Then the increment of normal displacement discontinuity ($\Delta \overset{j\xi}{D}_n$), shear displacement discontinuity ($\Delta \overset{j\xi}{D}_s$), fluid flux ($\Delta \overset{j\xi}{q}_f$) and heat flux ($\Delta \overset{j\xi}{h}_f$) at time t can be determined from the previous sets of the algebraic equations shown in Eq. C.5 to C.7.

Once we solve this linear algebraic equation, $\Delta \overset{j\xi}{D}_n$, $\Delta \overset{j\xi}{D}_s$, $\Delta \overset{j\xi}{q}_f$, and $\Delta \overset{j\xi}{h}_f$ should be changed to full loads to escape the influences from the previous time step.

$$\overset{j}{D}_n = \sum_{h=0}^{\xi} \Delta \overset{jh}{D}_n \; ; \; \overset{j}{D}_s = \sum_{h=0}^{\xi} \Delta \overset{jh}{D}_s \; ; \; \overset{j}{q}_f = \sum_{h=0}^{\xi} \Delta \overset{jh}{q}_f \; ; \; \overset{j}{h}_f = \sum_{h=0}^{\xi} \Delta \overset{jh}{h}_f \quad \text{..... (C.8)}$$

As a consequence, the total induced stress, pore pressure, and temperature on the i element at time t can be obtained in terms of the full loads.

$$
\begin{aligned}
\overset{i}{\sigma}_n(t) &= \sum_{j=1}^{N} \overset{ij}{A}(t-\tau_0)\overset{j}{D}_n + \sum_{j=1}^{N} \overset{ij}{B}(t-\tau_0)\overset{j}{D}_s + \sum_{j=1}^{N} \overset{ij}{C}(t-\tau_0)\overset{j}{q}_f + \sum_{j=1}^{N} \overset{ij}{T}(t-\tau_0)\overset{j}{h}_f \\
\overset{i}{\sigma}_s(t) &= \sum_{j=1}^{N} \overset{ij}{E}(t-\tau_0)\overset{j}{D}_n + \sum_{j=1}^{N} \overset{ij}{F}(t-\tau_0)\overset{j}{D}_s + \sum_{j=1}^{N} \overset{ij}{G}(t-\tau_0)\overset{j}{q}_f + \sum_{j=1}^{N} \overset{ij}{T}(t-\tau_0)\overset{j}{h}_f \\
\overset{i}{p}(t) &= \sum_{j=1}^{N} \overset{ij}{K}(t-\tau_0)\overset{j}{D}_n + \sum_{j=1}^{N} \overset{ij}{L}(t-\tau_0)\overset{j}{D}_s + \sum_{j=1}^{N} \overset{ij}{M}(t-\tau_0)\overset{j}{q}_f + \sum_{j=1}^{N} \overset{ij}{T}(t-\tau_0)\overset{j}{h}_f \\
\overset{i}{T}(t) &= \sum_{j=1}^{N} \overset{ij}{T}(t-\tau_0)\overset{j}{h}_f
\end{aligned}
\qquad \text{..... (C.9)}
$$

APPENDIX D

FLOW CHART FOR THE FRACTURE PROPAGATION ITERATIONS